UNIVERSITY OF CALGARY

Physical Modeling and Analysis of Seismic Data from a Simulated Fractured Medium

by

Faranak Mahmoudian

A THESIS

SUBMITTED TO THE FACULTY OF GRADUATE STUDIES

IN PARTIAL FULFILLMENT OF THE REQUIREMENTS FOR THE

DEGREE OF DOCTOR OF PHILOSOPHY

DEPARTMENT OF GEOSCIENCE

CALGARY, ALBERTA

June, 2013

UNIVERSITY OF CALGARY

FACULTY OF GRADUATE STUDIES

The undersigned certify that they have read, and recommend to the Faculty of Graduate Studies for acceptance, a thesis entitled "Physical Modeling and Analysis of Seismic Data from a Simulated Fractured Medium" submitted by Faranak Mahmoudian in partial fulfillment of the requirements for the degree of Doctor of Philosophy.

Supervisor, Dr. Gary F. Margrave
Department of Geoscience

Dr. Kristopher A. Innanen
Department of Geoscience

Dr. Donald C. Lawton
Department of Geoscience

Dr. David Wesley Hobill
Department of Physics and Astronomy

External Examiner, Dr. Douglas R. Schmitt,
University of Alberta, Department of Physics

Date

Abstract

This thesis studies the physical seismic modeling of a simulated fractured medium to examine variations of seismic reflection amplitudes with source-receiver offset and azimuth (AVAZ). The intent is to extract information about the fracture orientation and magnitude of the anisotropy of a naturally fractured medium. The simulated fractured medium is constructed from phenolic LE-grade material which exhibits orthorhombic symmetry. For initial characterization of the phenolic model, its elastic stiffness coefficients were determined from group velocities. The group velocities along various directions were obtained from three-component physical model transmission data. The phenolic model approximates a weakly anisotropic layer with horizontal transverse isotropy (HTI).

Three-dimensional (3D) physical model reflection data were acquired over a model consisting of the simulated fractured layer sandwiched between two isotropic plexiglas layers submerged in water. Interference between primary and ghost events was avoided with a careful 3D seismic survey design. After deterministic amplitude corrections, including a correction for the directivity effect of the physical model transducers, reflection amplitudes agreed with the amplitudes predicted by the Zoeppritz equations, confirming the suitability of the 3D physical model data for a quantitative amplitude analysis.

Linear AVAZ inversions for the fracture orientation and HTI anisotropic parameters (including shear-wave splitting parameter) were performed on P-wave reflection amplitudes from the top of the simulated fractured medium. Sensitivity analysis of the inversions results, including variations of the background velocity model and maximum incident angle used, confirms the accuracy of the amplitude analysis. The results reveal that the amplitude analysis of the P-wave data alone allows for extraction the information about the shear-wave anisotropy confined in the P-wave multi-offset and multi-azimuth amplitude data, without any S-measurements.

Acknowledgements

First of all I would like to express my gratitude to my supervisor Dr. **Gary Margrave** for his supervision, leadership, advice, and guidance in all aspects of this research. Above all, and the most appreciated, he provided me unyielding encouragement and support in various ways. I am indebted to him more than he knows. I gratefully acknowledge the CREWES Project sponsors for providing the financial means to complete this thesis.

I feel privileged to have learned a great deal from Dr. **Pat F. Daley** about seismic ray theory and anisotropy, and am very much grateful to him for his patient instruction. I'd like to acknowledge Dr. **Joe Wong** for his wonderful work in acquiring the physical seismic model data, his advise and many discussions, and his incredible patience with me in collecting more than 700 physical model seismic gathers for this dissertation. I'd like to acknowledge Mr. **David C. Henley** for many geophysical discussions and applying his amazing radial trace filtering in PROMAX to several seismic gathers used in this thesis, I will follow your discipline in adding walking to my weekly routine once I've defended, Dave! Mr. Eric Gallant constructed the phenolic layer used in this research, I am much indebted to his art in gluing the solid layers used in chapters 3 and 4, since I previously spent almost two years analyzing reflection amplitudes of a non-welded contact interface in growing despair.

Dr. **Don Lawton** helped me to a fast start with anisotropic measurements and related concepts, and also provided me with his course notes and support during the semester when I taught an undergraduate course that was suggested to me without any advance notice. I took a wonderful course in seismic inversion with Dr. **Kris Innanen**, linking scattering theory and seismic migration with inversion techniques, which opened a new venue for me to explore in the future. Dr. **Rob Ferguson** helped me with the (τ, p) transform code in Matlab. I had several extremely useful discussions with Dr. **Jon**

Downton which I could not utilize in this thesis due to time constraints. Mr. **Kevin Hall** and Ms. **Laura Baird** were great assistants throughout the course of this research. Dr. **Mostafa Naghizadeh** set me up with Latex which eased the writing task for many reports and this thesis, and guided me on several occasions. Dr. **Rolf Maier** edited this thesis for English along with me during late nights working on this thesis. Dr. **Michael Lamoureux** picked a geophysical mistake in my work which was not seen by any of the geophysicists around me. I had countless geophysical discussions with my friend **Mahdi Al-Mutlagh**, and had his constant support and help. My fellow graduate students in CREWES have been a constant source of help, ideas, good conversation, in particular Roohollah Askari, David Cho, Nasser Yousefzadeh, Raul Cova, Virginia Vera, Diane Lespinasse, Peter Gagliardi, Jean Cui, Heather Lloyd, Patricia Gavotti. I acknowledge them all with extreme gratitude.

Last but not least, I thank my husband, **Vafa Adib**, for his unending patience, encouragement, love, support, and faith in my abilities, our two beautiful children **Romina** and **Ryan** who have never known any lifestyle but the student-family lifestyle, my mother **Zari**, and my two sisters **Fariba** and **Fereshteh**, and my parents in law **Jaleh** and **Razi** for their prayers and support.

Dedication

To all of my teachers, especially my parents, and Gary,

and to my husband Vafa, and our two beautiful children Romina, and Ryan.

Table of Contents

List of Tables

List of Figures and Illustrations

List of Symbols, Abbreviations

α	P-wave vertical velocity
β	S-wave vertical velocity (fast S-velocity)
Δ	difference
ϵ, δ, γ	Thomsen's anisotropic parameters
$\epsilon^V, \delta^V, \gamma$	Rüger's anisotropic parameters for HTI media
θ	incident angle with respect to the vertical direction
φ	source-receiver azimuth
ρ	bulk density
A_{ij}	density-normalized stiffness coefficients
C_{ij}	stiffness coefficients
E_{ij}	(linearized) anellipsoidal deviation terms
I	identity matrix
P-wave	compressional wave
S-wave	shear wave
p	horizontal slowness
q	vertical slowness
qP	quasi compressional wave
qS_V	quasi shear-wave (polarized in plane of propagation)
qS_H	quasi shear-wave mode (polarized orthogonal to propagation plane)
t	two-way-travel time
V_{rms}	root-mean-square velocity

3C	three-component
3D	three-dimension
AGC	Automatical Gain Control
AVO	Amplitude Variation with Offset
AVAZ	Amplitude Variation with Angle and aZimuth
CMP	Common Mid-Point
HTI	Horizontal Transverse Isotropy
NMO	Normal-Move-Out
PP	reflected P wave from an incident P wave
PS	converted S wave from an incident P wave
VTI	Vertical Transverse Isotropy
VVAZ	Velocity Variations with aZimuth
(τ, p)	intercept time, horizontal component of the slowness vector

Chapter 1

Introduction

Naturally fractured reservoirs hold large hydrocarbon resources and represent attractive economic targets in exploration ventures. Many of the reservoirs, such as carbonates, tight clastics, and basement reservoirs are often fractured. Fractures play important roles in hydrocarbon production. They can provide pore space in reservoir rocks to hold oil and gas in place, and also increase the permeability of the reservoir rocks so oil and gas flows easily to well bores (Zheng, 2006). They can also have a negative impact on hydrocarbon production. Cemented or mineralized fractures may act as barriers to fluid flow. Consequently, the distribution and orientation of fractures are important for geophysicists, geologists, and reservoir engineers when evaluating a reservoir.

In exploring, developing, or evaluating a fractured formation, the zones of highest fracture intensity must be found and drilled (Nelson, 1985). For optimal oil recovery, the production wells should be drilled perpendicular or at some angle to the fracture orientation, as wells parallel to fracture orientation could possibly miss fractures. Therefore, the knowledge of fracture orientation and intensity helps in locating optimal drilling locations and predicting the production rates of new wells.

Characterization of natural fractures relies on direct and indirect sources of information. Fractures can be measured directly by logs (such as Formation Micro Imager (FMI) logs), or by checking core samples, which only provides information around the well bores. Three-dimensional (3D) three-component (3C) seismic can provide indirect overall information on fracture intensity and orientation. When seismic waves travel through, or are reflected from the boundaries of fractured layers, the fractures will leave footprints in the seismic data. Generally speaking, the fractured medium will affect the amplitudes and traveltimes of both P- and S-waves. This provides an opportunity to extract the fracture information from seismic waves by measuring the amplitude and/or velocity anisotropy.

Seismic modeling is one of the methods for studying the effects of fractures on seismic data, including phenomenons such as shear-wave splitting, or velocity and amplitude anisotropy. It is extremely useful in bridging the gap between theory and the complexities observed in seismic field data. In particular, physical modeling can provide invaluable insights in studying fractured reservoirs, a premise on which this thesis is build. More specifically, the effects of a simulated fractured medium on reflection amplitudes, recorded on physical model data, are examined here by means of a quantitative amplitude analysis.

1.1 Fractures: Geological overview

A natural fracture is defined as a macroscopic, plane discontinuity that results from stresses that exceed the rupture strength of the rock (Stearns, 1994). Virtually all reservoirs contain at least some natural fractures (Aguilera, 2003). From a geologic point of view the fractures can be classified as tectonic (fold and fault related), regional and contractional, and surface related (Aguilera, 2003). Depending on the origin, fractures display different patterns (Nelson, 1985). Fold and fault related fractures have an X-pattern (Figures 1.1a-b), regional and contractional fractures have orthogonal patterns (Figure 1.2), and surface-related fractures due to dry-out have polygonal patterns. Vertical fractures are among the most common fractures observed in naturally fractured reservoirs (Nelson, 1985). The thesis deals only with the modeling of vertical fractures.

Fracture orientation, or strike, is the direction of the fracture face. For the fold and fault related fractures, the average direction of the X-pattern is taken as the fracture orientation. In geological field observations of the regularity of the fractures that appear

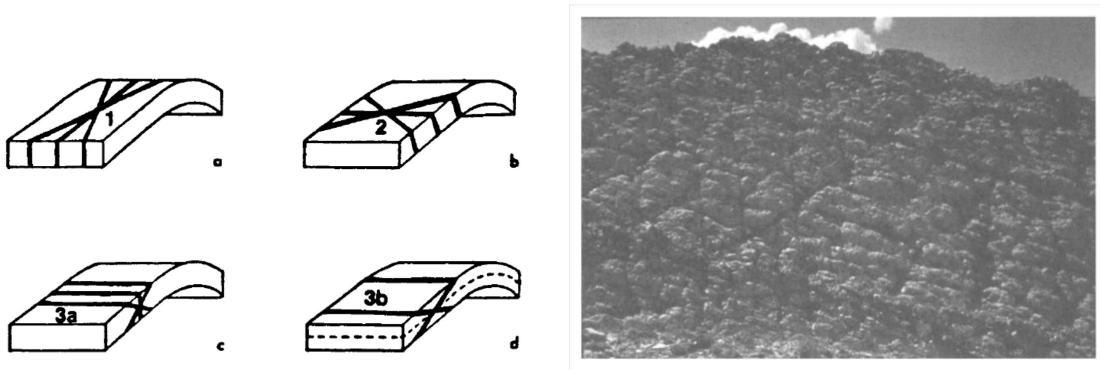

(a) (b)

Figure 1.1: (a) A generalization of dominant fold-related fracture sets (Nelson, 1985). (b) Tectonic fold-related fractures expressed on the bedding surface of Black Canyon anticline in the Rocky Mountains Foreland near Rawlins, Wyoming. The field of view is about 20ft (Nelson, 1985).

Figure 1.2: Orthogonal regional fractures in Devonian Antrim shale, Michigan Basin (Nelson, 1985).

in fold and fault related outcrops, it might appear that fracture orientation is random. However, measurement confirms a dominant fracture orientation related to the each stress regime in the field (Parsons, 1996; Nelson, 1985).

Together with fracture orientation, fracture intensity, or density, is the other important quantitative fracture system parameter which describes fracture porosity and permeability in a reservoir. Fracture density, the term used here in an attempt to qualify the abundance of fractures in a reservoir, is considered to be an effective influence of fracture width and fracture spacing on permeability. Fracture intensity is defined as

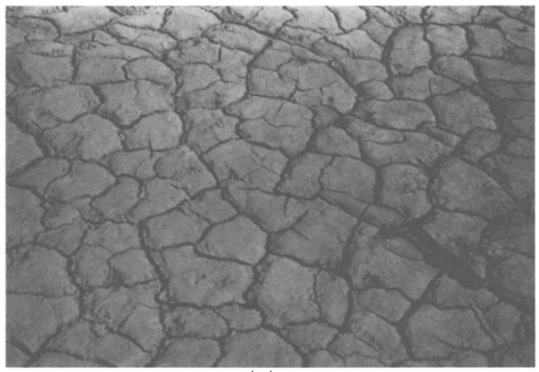

(a)

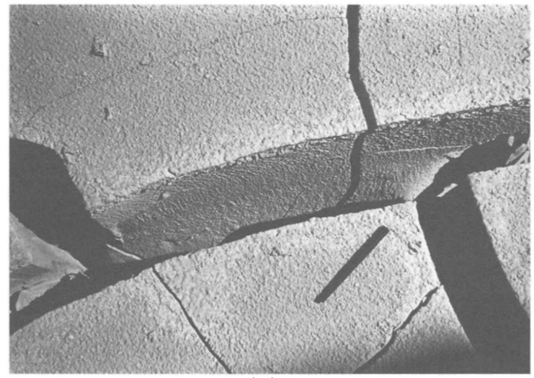

(b)

Figure 1.3: Surface-related fractures. (b) A zoomed portion of small part of photo in (a) (Nelson, 1985).

the product of fracture spacing and fracture width (Nelson, 2001). In the small scale of fractures, the values of fracture width range from 0.01mm up to 0.5mm (Nelson, 1985). Fracture spacing is defined as the average distance between regularly spaced fractures measured perpendicular to a parallel set of fractures of a given orientation (Nelson, 1985).

1.2 Fractures: Geophysical point of view

Fractures can be expected of all length scales, which is consistent with observation (Lynn, 2004a,b; Schijns et al., 2012). At the upper end of the scale, faults are visible in seismic images. Moving down the scale, fractures lie well beneath the limit of seismic resolution. They nonetheless can be observed through induced seismic anisotropy. The dominant orientation of fracture networks result in the fractured medium displaying azimuthal anisotropy in seismic wave propagation. Seismic waves travel faster in the direction of the fracture orientation (Bale, 2006). S-waves polarized parallel to the fracture orientation propagate faster than S-waves polarized orthogonal to it, a phenomenon known as shear-wave splitting or S-wave birefringence which historically has been a diagnostic informative and easily observable evidence of fractures (Crampin, 1981). Also, P-wave NMO velocity appears to be faster in the direction of the vertical fractures, known as velocity variation with angle and azimuth (VVAZ) Tsvankin (2001). Also, there are differences in the seismic amplitude response parallel and perpendicular to fractures, known as amplitude variation with angle and azimuth (AVAZ) Zheng (2006). AVAZ is useful for determining dominant fracture orientation, fracture intensity, and sometimes the types of fluid in fractures.

Horizontal transverse isotropy (HTI) is a first-order approximate symmetry model to describe vertical fractures embedded in an otherwise isotropic rock matrix (Bale, 2006; Rüger, 2001). In an HTI model, the fracture plane is considered to be isotropic, and the direction normal to it is referred to as the symmetry axis (Figure 1.4). A more realistic anisotropic model to represent the long-wavelength behavior of vertical fractures, however, is orthorhombic symmetry (Schoenberg and Helbig, 1997). A combination of a vertical transverse isotropy (VTI) background medium with a system of aligned vertical fractures can be considered as a simple orthorhombic model. A medium with orthorhombic symmetry is an anisotropic medium with three distinct and mutually orthogonal planes of symmetry. Transverse isotropy, TI, particularly with vertical symmetry axis (VTI) and HTI, is a degenerate case of orthorhombic symmetry.

1.3 Physical modeling

Numerical seismic modeling plays an important role in improving our understanding of seismic wave propagation, and in the verification of processing algorithms. Seismic modeling, the process through which a subsurface geologic model is transformed into a seismic record, has been extensively done using numerical methods. The mathematical formulation (acoustic or elastic) of wave propagation, and complexities in the computa-

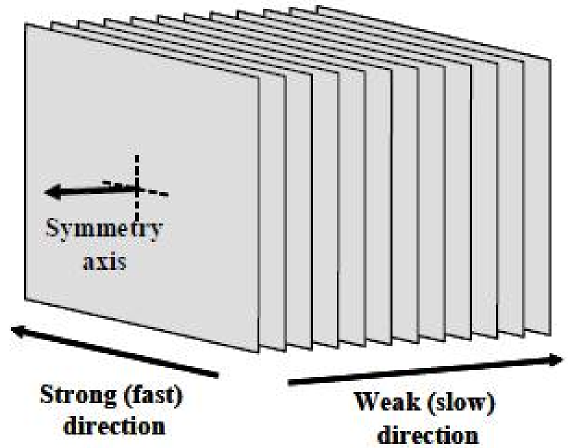

Figure 1.4: Schematic depiction of an HTI medium (Bale, 2006). The vertical planes representing the fracture planes are the isotropy planes of the HTI model. The direction normal to the isotropy plane is the axis of symmetry.

tional processes when modeling complex geological features, make numerical modeling challenging.

In physical seismic modeling, an alternative to numerical modeling, the seismic data are acquired over small, laboratory sized geological models. Physical modeling has been used to evaluate the accuracy of mathematical models of wave propagation, to test seismic data processing algorithms, and to provide insights into the interpretation of 3C seismic data acquired over complex media (Ebrom and McDonald, 1994). Physical model data have been used for many years to simulate exploration targets, of which a fractured medium is an example. Traveltime and qualitative amplitude analysis of physical model data acquired over simulated fractured media have been employed by many researchers (Cheadle et al., 1991; Brown et al., 1991; Tadepalli, 1995; Sayers and Ebrom, 1997; Grechka et al., 1999; Mah and Schmitt, 2001a; Theophanis and Zhu, 2003; Wang and Li, 2003; Wang et al., 2007; Zheng and Wang, 2005; Chang and Gardner, 1997; Chen and Hilterman, 2007; Enkanem et al., 2009; Ortiz-Osornio and Schmitt, 2010). Physical modeling has gained interest in the study of anisotropic media as the waves propagate in the same way that they propagate in real earth anisotropic media. The challenges associated with numerical modeling methods, including employing approximate mathematical formulations (e.g., acoustic or elastic) and assumptions, or purely computational difficulties like grid dispersion, are not present in physical modeling.

1.3.1 The physical modeling system

The University of Calgary physical modeling system has a scale of (1 : 10000) for length and time (Figure 1.5). This means that, for example, 1mm in the physical model represents 10m and a frequency of 500kHz represents a frequency of 50Hz in seismic field data. Having the same scale factor for length and time allows the velocity of the medium to remain unscaled.

In physical modeling, the sources and receivers are ultrasonic piezoelectric transducers. A piezoelectric material has the property that, if deformed by external mechanical pressure, electric charges are produced on its surface, thus acting as a seismic receiver. If placed in an electrical field, a transducer changes its form producing mechanical pressure simulating a seismic source (Krautkrämer and Krautkrämer, 1975). Compressional and shear-wave (P and S) piezoelectric transducers are used, as both sources and receivers, in acquiring the physical model seismic data. As receivers, the P- and S-transducers are sensitive to displacements normal and tangential to the contact face of the transducer, respectively, and represent vertical and horizontal component geophones. As a source, the P- or S-transducers generate both P- and S-waves. Generally, the P-transducer emanates dominating P-wave and the S-transducer emanates dominating S-waves. Transducers of different sizes were employed in the acquisition of the physical model data used in this thesis. More specific details regarding the transducers based on their specific usages, e.g. collecting transmission gather or reflection gathers, will be given individually for each experiment. As two examples, contact P-transducers were used to collect the transmission gathers of Chapter 2 (Figure 1.6), and pin P-transducers were used to collect the

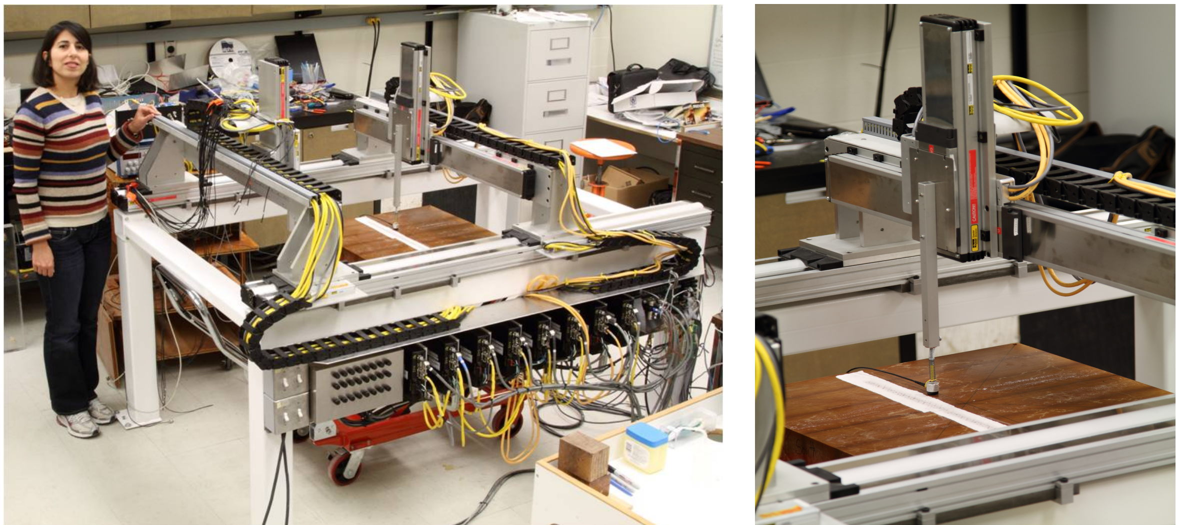

(a) (b)

Figure 1.5: (a) Physical modeling system at the University of Calgary/CREWES Project. (b) Zoomed of one of the positioning arms. The contact circular transducer is a S-transducer and a strip of napkin at the contact is used to provide good coupling.

reflection gathers of Chapter 3 (Figure 1.7).

The modeling system is equipped with a robotic positioning system which has a positioning error of less than 0.1mm. There are separate arms for positioning the source and receiver (Figure 1.5) transducers. Vertical stacking of repeated source excitations for each receiver position, and the progressive re-positioning of the receiver transducer, generate a seismic gather. The vertical stacking processes ensured a high signal-to-noise ratio for the collected physical model datasets.

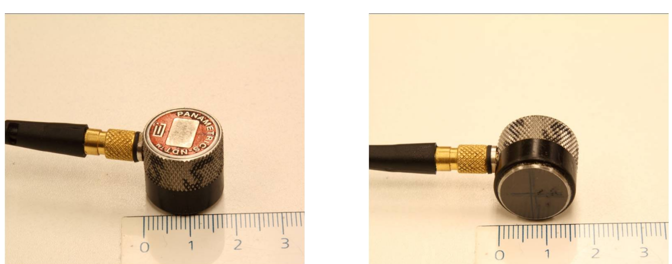

(a) (b)

Figure 1.6: The P-transducer Panametric $V103$ with a diameter of 13mm and a nominal central frequency of 300kHz. (a) The contact transducer attached to a surface. (b) The contact surface of the transducer.

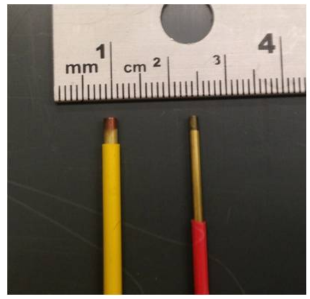

Figure 1.7: Piezoelectric Dynasen CA-1136 pin transducers with the piezoelectric element being 1.36mm and 1.1mm in diameter, with a nominal central frequency of 500kHZ.

The location of a transducer is assigned to the location of the center of its contact face. Thus, the stored coordinates in trace headers show the location of the center of the transducers. The first source and receiver are nearly always manually positioned according to a predefined coordinate system. Once the initial source-receiver offset is set, the subsequent increments in offset are computer controlled, and as a consequence are accurately known. The source pulse is highly repeatable over many hours of acquisition. The pulse excitation is provided by a high voltage pulse generator which has independent voltage control. More details about the University of Calgary laboratory equipment and set-up can be found in Wong et al. (2009).

1.3.2 The simulated fractured medium

In the physical modeling of anisotropic media, and fractured media in particular, the first challenge is to produce a model that is reasonably representative of real earth geology. Hsu and Schoenberg (1993) and Luo and Evan (2004) simulated a fractured medium by constructing a physical layer consisting of closely spaced parallel isotropic sheets of Plexiglas. Phenolic material has been used to simulate a fractured medium for qualitative amplitude analysis (e.g., Uren et al., 1990; Brown et al., 1991; Cheadle et al., 1991; Tadepalli, 1995; Chang and Gardner, 1997; Mah and Schmitt, 2001a; Wang and Li, 2003). Phenolic materials, because of their micro-layered texture, can be used to simu-

Figure 1.8: Phenolic material from manufacturer.

late finely layered rocks, such as some sandstones, shale, or fractured limestone (Chang and Gardner, 1997). The phenolic material exhibits seismic anisotropy with apparent orthorhombic symmetry (Brown et al., 1991; Cheadle et al., 1991; Karayaka and Kurath, 1994).

For the purpose of this thesis, a physical model is constructed from phenolic material. This simulated fractured layer is made of LE-grade^{TM} phenolic material, which is composed of laminated sheets of linen fabric bonded together with phenolic resin (Figure 1.8), and has a density of 1390 kg/m^3. A manufactured board of phenolic material is milled to provide flat and perpendicular surfaces parallel to the layering, the warp, and the weave of linen fabric, as closely as possible. Hence, the symmetry of phenolic materials is relatively well controlled (Mah and Schmitt, 2001b). To construct the simulated fractured layer used in this study, the original board of phenolic material with horizontally-laid linen fabric was cut into slabs along planes orthogonal to the plane of the linen layers. These were rotated 90° and bonded together with epoxy under uniform high pressure. This constructed layer simulates a homogeneous horizontal layer with vertical fractures of a single orientation. It has an approximate area of $57 \times 57\text{cm}^2$ and a thickness of 7cm (Figure 1.9 and 1.10). Note that the LE grade phenolic material is different from the CE-grade phenolic material studied by Brown et al. (1991) and Mah and Schmitt (2001a).

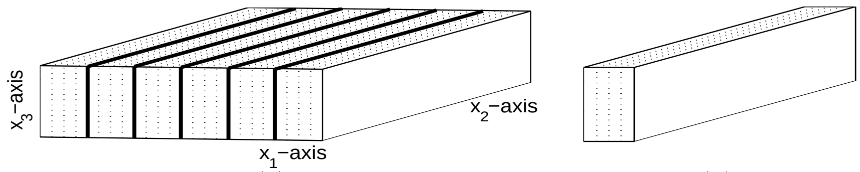

(a) (b)

Figure 1.9: (a) The simulated fractured medium in this study. The dark lines indicate glued seams between separate phenolic blocks. (b) A slab of phenolic material with dashed lines displaying the linen planes.

Figure 1.10: The constructed phenolic layer used for this study. The slab contacts were epoxy glued under a press machine.

1.4 Hardware and software used

The physical modeling work presented in this thesis was done using the physical modeling facility operated by the CREWES Project of the Department of Geosciences at the University of Calgary. The physical modeling data were acquired by Dr. Joe Wong. The author was involved in the majority of the data collection procedure. The computer software to run the physical modeling machine was written by Dr. Joe Wong. The construction of the phenolic experimental layer, and preparation of the solid interfaces to ensure a properly welded contacts were done by Mr. Eric Gallant of the University of Calgary. The ultrasonic transducers, used in the data acquisition of chapter 2, were from Olympus®. The piezoelectric pin transducers, used in the data acquisition in chapter 3, were from Dynasen Inc. The phenolic material was purchased from Johnston Industrial Plastics.

The majority of the programming was done in the MATLAB programming language. This includes the AVAZ inversions, amplitude corrections procedures, the (τ, p) transform, and velocity log smoothing. Synthetic data were generated using finite-difference code written in MATLAB by Dr. Gary Margrave of the University of Calgary. A number of other MATLAB-based programs coded, including the PP raytracing code, by Dr. Gary Margrave, were also utilized in this research. The physical model data were filtered in PROMAX using the radial trace filtering by Mr. David C. Henley of the CREWES Project. All plots in this thesis were generated in MATLAB. The five-layered model was generated using Google SketchUp by Ms. Sayeh Moayerian. Word processing and thesis assembly was done on a laptop computer using WinEdt 6.0 with a LaTeX engine.

1.5 Thesis objectives and organization

The main objective of this thesis is to investigate the effect of natural vertical fractures on 3D seismic data by employing physical seismic modeling. First, an initial characterization of the simulated fractured medium is explained. Second, the suitability of physical model data collected over the simulated fractured medium, generated by finite-size source and receiver transducers, is discussed in the context of a quantitative amplitude analysis. Third, applying amplitude inversions to 3D physical model data enables a determination of the accuracy of amplitude analysis in providing information about fracture orientation and intensity.

This thesis is organized as follows.

Chapter 2 presents the method for the initial characterization of the simulated fractured medium by determining all its elastic stiffness coefficients. Some descriptions of orthorhombic symmetry, relationships linking the phase and group velocities to the orthorhombic stiffness coefficients, are given. Previous work on determining the stiffness coefficients, and methods to measure the phase and group velocities using finite-size transducers, are investigated. The stiffness coefficients of the experimental phenolic layer are determined from group velocities using a linearized expression between the group velocities and the stiffness coefficients. The accuracy of the estimates is confirmed by comparing the measured phase and group velocities to those predicted by the stiffness coefficient estimates. The experimental phenolic layer is found to approximate a weakly anisotropic medium with HTI symmetry, which makes it an appropriate model for use in the simulation of a fractured medium.

Chapter 3 presents the acquisition of the 3D reflection physical model data over a five-layered medium including the simulated fractured medium and top water layer. The targets are reflection amplitudes from the top of the fractured layer. The processing steps to extract the reflection coefficients from the reflection amplitudes of the target event are developed. The effect of finite-size transducers on reflection amplitudes is investigated and removed from recorded amplitudes. The corrected reflection amplitudes follow the theoretical amplitudes predicted by the Zoeppritz equations, indicating the suitability of the physical model data for a quantitative amplitude analysis.

Chapter 4 presents the plane-wave approximation for PP reflection coefficients from a boundary of two HTI media. Knowing the fracture orientation, the chapter develops the AVAZ inversion to extract anisotropy parameters of the simulated fractured medium from pre-stack P-wave amplitudes. The method to determine the fracture orientation from azimuthal amplitude variation is rigorously investigated, followed by the AVAZ inversion of small-incident-angle data for fracture orientation. The AVAZ inversions are then applied to the physical model data. Finally, some criteria on how to apply a successful AVAZ inversion to elucidate fracture orientation and intensity are discussed by comparing the inversion results with the results already obtained from traveltime analysis in Chapter 2.

1.6 Thesis contributions

The contributions of this thesis can be summarized as follows

- Determination of stiffness coefficients of an orthorhombic physical model, the simulated fractured medium, from group velocities along various directions. The method is based on a relatively new approximate relationship by Daley and Krebes (2006) between group velocity and stiffness coefficients.
- The PP reflection amplitudes from the top of the simulated fractured layer, after required AVO corrections, reveal a clear azimuthal variation caused by the simulated fractured layer, and agreed with amplitudes predicted theoretically. Hence, the suitability of 3D physical model data for a quantitative amplitude analysis of anisotropic targets was confirmed.
- Applying AVAZ inversions, written in MATLAB, to obtain fracture orientation and intensity from P-wave reflection data, demonstrated that it is possible to relate the difference in P-wave azimuthal AVO variations directly to the fracture intensity of the simulated fractured layer. Some sensitivity analysis for successful AVAZ inversions using physical model data was applied.

Chapter 2

Determination of stiffness coefficients

The initial characterization of the constructed phenolic layer is presented in this chapter. The elastic properties of the experimental phenolic layer are estimated by determining all of its density-normalized stiffness coefficients, $A_{ij} = C_{ij}/\rho$, from group velocity measurements obtained from traveltimes.

The methods of measuring the phase and group velocities from physical modeling transmission gathers are explained. The group velocity measurements are straightforward and reasonably accurate, whereas the phase velocities measurements require specialized physical modeling setups. The phase and group velocities along various directions are measured from the transmission gathers collected over the phenolic model. The group velocity measurements are then used to estimate the density-normalized stiffness coefficients of the phenolic model. An approximate explicit expression for the qP wave group velocity (Song and Every, 2000; Daley and Krebes, 2006) is used to estimate the off-diagonal stiffness coefficients. The predicted phase and group velocities from the estimates of stiffness coefficients are closely comparable to the measured velocities. The estimated density-normalized elastic coefficients will be used to evaluate the accuracy of the AVAZ inversion (Chapter 4) in predicting the anisotropy parameters of the phenolic layer.

2.1 Background

In anisotropic media, the velocity of seismic waves varies with the direction of propagation. The phase velocity is the wavefront's propagation velocity in the direction normal to the wavefront, and the group (ray) velocity is the energy propagation velocity along the raypath from the source to the receiver (Figure 2.1).

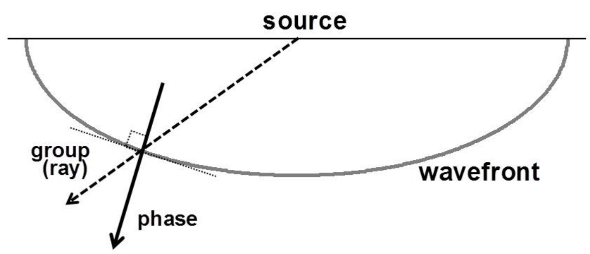

Figure 2.1: The wavefront, group (ray) direction, and phase direction in a homogeneous anisotropic medium.

In anisotropic media, the polarization of the body waves are not, in general, longitudinal or transverse to the direction of the wave propagation, because of the differences of elastic properties with direction (Musgrave, 1970). There are then, in general, three body-waves which propagate through an anisotropic medium, called quasi-P, quasi-S_V, and quasi-S_H[1] (qP, qS_V, qS_H).

2.1.1 Stiffness coefficient matrix

This section follows Thomsen (1986) in describing the stiffness coefficient matrix. An elastic material is defined as one in which each component of stress, σ_{ij}, is linearly dependent upon every component of strain, e_{kl}, (Nye, 1957). Since each directional index may assume values of 1, 2, 3 (representing the directions x, y, z), there are nine such relations, each involving one component of stress and nine components of strain. These nine equations may be written compactly as

$$\sigma_{ij} = \sum_{k=1}^{3} \sum_{l=1}^{3} c_{ijkl} e_{kl}, i, j = 1, 2, 3, \tag{2.1}$$

where the $3 \times 3 \times 3 \times 3$ elastic stiffness coefficients tensor, c_{ijkl}, completely characterizes the elasticity of the medium. Because of the symmetry of stress ($\sigma_{ij} = \sigma_{ji}$), only six

[1]Quasi-S waves are also called qS_1 and qS_2.

of these equations are independent. Because of the symmetry of strain ($e_{kl} = e_{lk}$), only six of the terms on the right-hand side of each set of equation 2.1 are independent. Hence, without loss of generality, the elasticity may be represented more compactly with a change of indices, following the Voigt recipe for indexes (ij or kl): $11 \to 1$, $22 \to 2$, $33 \to 3$, $32 = 23 \to 4$, $31 = 13 \to 5$, $21 = 12 \to 6$, so that the $3 \times 3 \times 3 \times 3$ tensor c_{ijkl} may be presented by the 6×6 matrix C_{ij} where both i and j range over $1, 2, ..., 6$.

In this thesis, the density-normalized stiffness coefficients ($A_{ij} = C_{ij}/\rho$), which have the dimensions of (velocity)^2, are dealt with exclusively. Each symmetry class has its own pattern of nonzero, independent components A_{ij}. For example, for isotropic media the density-normalized stiffness matrix assumes the simple form

$$\begin{bmatrix} A_{33} & A_{33}-2A_{44} & A_{33}-2A_{44} & & & \\ A_{33}-2A_{44} & A_{33} & A_{33}-2A_{44} & & 0 & \\ A_{33}-2A_{44} & A_{33}-2A_{44} & A_{33} & & & \\ & & & A_{44} & & \\ & 0 & & & A_{44} & \\ & & & & & A_{44} \end{bmatrix}. \tag{2.2}$$

The simplest anisotropic case of broad geophysical applicability has one distinct direction, while the other two directions are equivalent to each other. This case called transverse isotropy, or hexagonal symmetry, has five independent elastic coefficients. The stiffness matrix of the horizontal transverse isotropy (HTI), with the unique axis along the x_1-axis and the isotropic plane being (x_2, x_3) (Figure 1.9), is characterized by independent elastic coefficients $A_{11}, A_{33}, A_{44}, A_{55}, A_{13}$, and its matrix of density normalized stiffness coefficients follows as (Musgrave, 1970)

$$\begin{bmatrix} A_{11} & A_{13} & A_{13} & & & \\ A_{13} & A_{33} & A_{33}-2A_{44} & & 0 & \\ A_{13} & A_{33}-2A_{44} & A_{33} & & & \\ & & & A_{44} & & \\ & 0 & & & A_{55} & \\ & & & & & A_{55} \end{bmatrix} . \tag{2.3}$$

Note that the off-diagonal elastic coefficient $A_{23} = A_{33} - 2A_{44}$, related to the isotropic plane (x_2, x_3), obeys the isotropy relation.

An orthorhombic medium with three distinctive axes has nine independent stiffness coefficients. Consider the reference Cartesian coordinate system, (x_1, x_2, x_3), associated with the orthorhombic symmetry planes. In this reference coordinate system, the nine independent orthorhombic density-normalized stiffness coefficients are the six diagonal terms (A_{ii}) plus three off-diagonal terms (A_{23}, A_{13}, A_{12}). The resulting symmetric stiffness matrix is

$$\begin{bmatrix} A_{11} & A_{12} & A_{13} & 0 & 0 & 0 \\ A_{12} & A_{22} & A_{23} & 0 & 0 & 0 \\ A_{13} & A_{23} & A_{33} & 0 & 0 & 0 \\ 0 & 0 & 0 & A_{44} & 0 & 0 \\ 0 & 0 & 0 & 0 & A_{55} & 0 \\ 0 & 0 & 0 & 0 & 0 & A_{66} \end{bmatrix} . \tag{2.4}$$

An HTI model is a degenerated case of an orthorhombic symmetry with only five independent elastic coefficients.

2.1.2 How to estimate orthorhombic stiffness coefficients.

Anisotropic stiffness coefficients can be estimated from phase or group velocities related to quasi-body waves. For the orthorhombic symmetry planes, there are exact explicit relations between the stiffness coefficients and the phase velocities obtained from the solution of the Christoffel equation. Consequently, the stiffness coefficients are most often determined using the measured phase velocities (e.g., McSkimin, 1967; Vestrum et al., 1999; Mah and Schmitt, 2001a). For group velocity, there are no known exact explicit relationships to the anisotropic stiffness coefficients. Using iterative least-squares fitting, the stiffness coefficients have been estimated from group velocities measured over a various directions (e.g., Every and Sachse, 1992; Kim et al., 1995; Okoye et al., 1996; Vestrum et al., 1999).

In an orthorhombic media, along the coordinate principal directions (i.e. x_1-, x_2-, and x_3-axis), phase and group velocities are equal. The quasi-body wave velocities along the coordinate principal axes determine diagonal stiffness coefficients (Table 2.1). Three qP velocities specify the $A_{ii}(i = 1 : 3)$, and three qS velocities specify $A_{ii}(i = 4 : 6)$. The off-diagonal stiffness coefficients, however, are not individually related to the phase or group velocity along some arbitrary directions. Next the relation between off-diagonal density-normalized stiffness coefficients and group velocity is described.

Table 2.1: Body waves' velocities along the principal axes for an orthorhombic medium. Here V_{ij} $(i, j = 1, 2, 3)$ is the body wave velocity which propagates along the x_j-axis and polarized along the x_i-axis. For example V_{11} is the qP velocity propagating along the x_1-axis, and $V_{23}(= V_{32})$ is the qS velocity propagating along the x_3-axis and polarizing along the x_2-axis.

	Propagation		
Polarization	x_1	x_2	x_3
x_1	$V_{11} = \sqrt{A_{11}}$	$V_{12} = \sqrt{A_{66}}$	$V_{13} = \sqrt{A_{55}}$
x_2	$V_{21} = \sqrt{A_{66}}$	$V_{22} = \sqrt{A_{22}}$	$V_{23} = \sqrt{A_{44}}$
x_3	$V_{31} = \sqrt{A_{55}}$	$V_{32} = \sqrt{A_{44}}$	$V_{33} = \sqrt{A_{33}}$

2.2 Theory

Let $\vec{N} = (N_1, N_2, N_3) = (sin\Theta cos\Phi, sin\Theta sin\Phi, cos\Theta)$ be a unit vector in the direction of group velocity (ray direction), where Θ is the polar angle measured from the x_3-axis and Φ is the azimuthal angle measured from the x_1-axis. An approximate linearized expression for the qP group velocity (Song and Every, 2000; Daley and Krebes, 2006) in terms of the A_{ij} in an orthorhombic medium is

$$\begin{aligned} \frac{1}{V^2(\vec{N})} \simeq & \frac{N_1^2}{A_{11}} + \frac{N_2^2}{A_{22}} + \frac{N_3^2}{A_{33}} - \\ & \frac{E_{23}N_2^2N_3^2}{A_{22}A_{33}} - \frac{E_{13}N_1^2N_3^2}{A_{11}A_{33}} - \frac{E_{12}N_1^2N_2^2}{A_{11}A_{22}}, \end{aligned} \tag{2.5}$$

where the quantities E_{ij}, are

$$\begin{aligned} E_{23} &= 2(A_{23} + 2A_{44}) - (A_{22} + A_{33}), \\ E_{13} &= 2(A_{13} + 2A_{55}) - (A_{11} + A_{33}), \\ E_{12} &= 2(A_{12} + 2A_{66}) - (A_{11} + A_{22}). \end{aligned} \tag{2.6}$$

The E_{ij} are called anellipsoidal deviation terms, as they describe the deviation of the wavefront from ellipsoidal anisotropy (see Appendix A). Equation 2.5 explicitly represents the qP group velocity in terms of the nine orthorhombic A_{ij}. Daley and Krebes (2006) derived equation 2.5 solving the eikonal equation by the method of characteristics. Their orthorhombic qP group velocity formula is identical with that presented by Song and Every (2000) where the results were not established by rigorous derivation but were consistent with the numerical results.

Assuming the diagonal A_{ij} are known, the off-diagonal stiffness coefficients may be obtained from the qP group velocity expression, equation 2.5. It can be written as

$$D = BE_{23} + FE_{13} + LE_{12}, \tag{2.7}$$

where the coefficients D, B, F, L are defined as follows

$$D = (\frac{{N_1}^2}{A_{11}} + \frac{{N_2}^2}{A_{22}} + \frac{{N_3}^2}{A_{33}}) - \frac{1}{V(\vec{N})^2},$$
$$B = \frac{{N_2}^2{N_3}^2}{A_{22}A_{33}}, F = \frac{{N_1}^2{N_3}^2}{A_{11}A_{33}}, L = \frac{{N_1}^2{N_2}^2}{A_{11}A_{22}}. \tag{2.8}$$

Incorporating qP velocity measurements in m different directions, equation 2.7 can be used to obtain a linear system of m equations in the three unknowns (E_{23}, E_{13}, E_{12}). The linear system of equations has the form:

$$\begin{pmatrix} B_1 & F_1 & L_1 \\ \vdots & \vdots & \vdots \\ B_n & F_n & L_m \end{pmatrix} \begin{pmatrix} E_{23} \\ E_{13} \\ E_{12} \end{pmatrix} = \begin{pmatrix} D_1 \\ \vdots \\ D_n \end{pmatrix}. \tag{2.9}$$

Or, in a matrix notation, $GE = D$. The unknown vector E will result from a damped least-squares inversion, as $E = (G^TG + \mu)^{-1}G^TD$ where the μ is the damping factor. Knowing the deviation terms and diagonal A_{ij}, the off-diagonal A_{ij} can be determined from equation 2.6 as

$$\begin{aligned} A_{23} &= (E_{23} - 4A_{44} + A_{22} + A_{33})/2, \\ A_{13} &= (E_{13} - 4A_{55} + A_{11} + A_{33})/2, \\ A_{12} &= (E_{12} - 4A_{66} + A_{11} + A_{22})/2. \end{aligned} \tag{2.10}$$

The group velocity measurements should be along various directions, and the number of them should be larger than three to obtain an over-determined and well-posed system of equations. A larger number of m results in a more stable solution. The accuracy of these estimations is dependent on the accuracy of the diagonal A_{ij}. Some numerical tests of this inversion for off-diagonal stiffness coefficients are presented in Appendix B.

2.3 Velocity measurements

For rock samples, seismic velocities are often measured using relatively large ultrasonic transducers in a transmission geometry (Bouzidi and Schmitt, 2009). Using two flat-faced transducers attached to the model in various propagation directions, body-wave velocities can be measured by picking arrival times. According to Dellinger and Vernik (1994) and Vestrum (1994) such measurements estimate group velocities if the source-receiver separation is large compared to the transducer size. If the transducers are large compared to their separation, they will approximately transmit and receive plane waves over a large spatial interval (Figure 2.2), thus enabling direct phase velocity measurement (Dellinger and Vernik, 1994; Vestrum, 1994). To measure phase velocity from small samples, the specimen gets appropriate cuts along various directions to make the desired contact plane for the flat-faced large transducers. Then the phase velocity along the direction normal to the cut planes can be measured. The next section describes measuring the group and phase velocity on large physical models which simulate some geological features rather than small core samples.

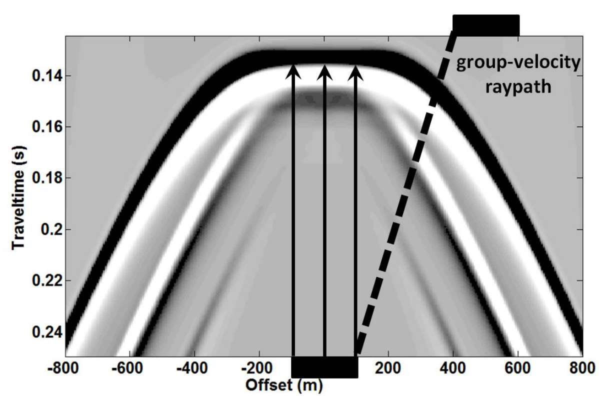

Figure 2.2: An illustration of the wavefront radiated and recorded by large circular physical model transducers (modeled by an acoustic finite-difference method). The black parallel vectors show the travel of the plane-wave portion of the wavefront. The transducer's size is chosen to be half of the layer thickness to exaggerate the plane-wave generation.

2.3.1 Group velocity

Consider a physically modeled transmission gather, where the source transducer is located on one side of the model and the receiver's profile is positioned on the other side. Treating the physical model as a homogeneous layer, for point source and receiver transducers, the length of the straight line connecting the source and receiver divided by the first arrival traveltimes yields the group velocity in the source-receiver raypath direction. For large source and receiver transducers, the effective source-receiver raypath is the straight line connecting the nearest edges of source and receiver transducers (Figure 2.2). Brown et al. (1991) calculated the group velocities in various directions by dividing such effective source-receiver raypaths by the first arrival traveltimes of each mode. In this thesis their method in measuring the group velocities is followed, hence the effective size of transducers needs to be known. The effective size of transducers is defined by the active portion of the piezoelectric crystal, and might be slightly different from the given size by the manufacturer. The appropriate effective transducer size is decided from recordings in an isotropic homogeneous plexiglas layer in advance. A justification for considering the nearest edges distance as the raypath taken by the first arrival energy is provided below.

A circular physical model transducer can be considered as a continuous source/receiver array. Using finite-difference modeling over an isotropic layer with a constant velocity of 3500m/s, for this thesis a transmission gather, utilizing source and receiver arrays representing a transducer with the diameter of 13mm (Figure 2.3a), is generated. To generate the transmission gathers, acoustic finite-difference software is used which utilizes a nine-point approximation to the Laplacian operator. The time steps were chosen to be small enough ensuring that grid dispersion is as small as possible. A minimum phase wavelet with the dominant frequency of 50HZ is used as the initial wavelet. In the finite-difference generated transmission gather, the change in wavelet shape from near to far offset is apparent and is due to finite-size source and receivers. Figure 2.3b shows the measured group velocity, obtained from first arrival times divided by the straight-line raypath length, versus the group angle (the direction along nearest elements of the source and receiver arrays) with an error of ±10m/s. Using the edge-to-edge distance rather than the center-to-center distance between the source and receiver transducers, is a simple geometrical correction.

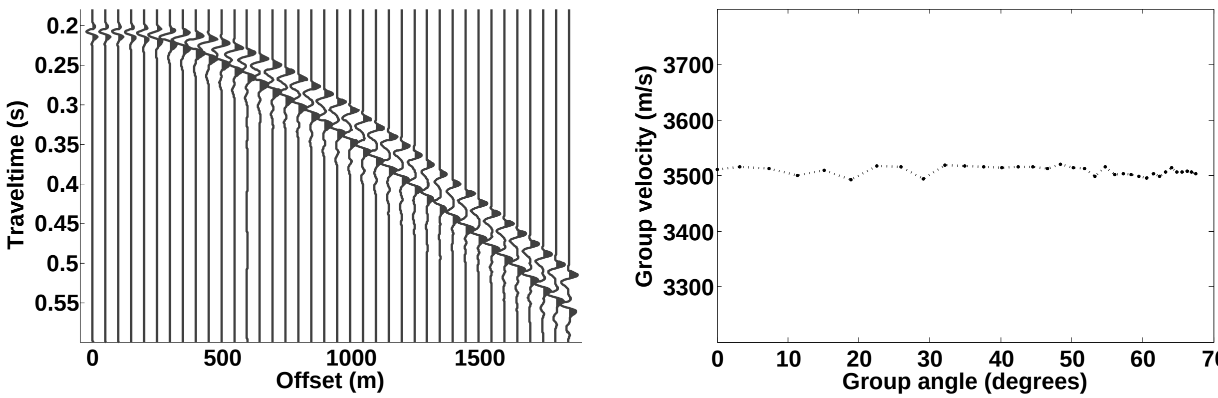

(a) (b)

Figure 2.3: (a) Finite-difference generated transmission gather over a constant velocity layer with a velocity of 3500m/s and source and receiver size of 13mm. (b) Measured group velocity.

Figure 2.4 shows the group velocities of the experimental phenolic layer measured from physical model transmission gathers acquired with 1.3mm, 6mm, and 13mm transducers. The measurements from these three transducer sizes are consistent to within the picking error, and independent of the size of the transducer used. A short gate automatic gain control was applied to facilitate a careful first break picking.

2.3.2 Phase velocity

Kebaili and Schmitt (1997) presented a method using the (τ, p) transform to measure phase velocity from two transmission shot gathers with two different shot depths. Consider two transmission shot gathers recorded with the shots at depths of d_1 and d_2, acquired by point sources and receivers. In a transmission gather the first arrival of each

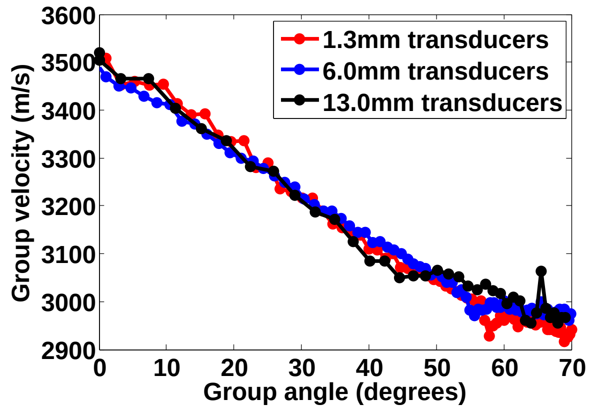

Figure 2.4: Group velocity measured from transmission data acquired with three transducer's size using an edge-to-edge correction.

mode, for example P-wave, approximately appears as an hyperbolic event (Figure 2.5b). Taking the (τ, p) transform, the first arrival hyperbola will be approximately mapped onto an ellipse [2]. In each transmission gather, consider the line with the slope of p_0 ($t = \tau_1 + p_0 x$ and $t = \tau_2 + p_0 x$) tangent to the first arrival hyperbola (Figure 2.5b). These lines designate plane waves traveling with the horizontal slowness of p_0, intercepting the time axis at τ_1 and τ_2. Summation along these two lines produces the two points, (τ_1, p_0) and (τ_2, p_0), at each (τ, p) event, respectively. Effectively, the p_0 plane wave has traveled the vertical distance of $d_2 - d_1$ with the vertical slowness of $q_0 = (\tau_2 - \tau_1)/(d_2 - d_1)$ from the source at d_1 to the source at d_2. Therefore, for any particular horizontal slowness, of p_0, in the (τ, p) domain, the two (τ_1, p_0) and (τ_2, p_0) points, picked from the transform of the first arrival hyperbolic events, will estimate the phase velocity as $v_{p_0} = ({p_0}^2 + {q_0}^2)^{-1/2}$.

For a point source and receivers, in this thesis two finite-difference transmission gathers are generated through an isotropic layer with the constant velocity of 3500m/s, with the shot depths at $d_1 = 500m$ and $d_2 = 400m$ (Figure 2.6). For each p_0, the corresponding (τ_1, p_0) and (τ_2, p_0), are picked from the ellipses in the (τ, p) transforms of the two gathers. Figure 2.7a shows the measured phase velocities versus phase angle. As is ap-

[2]Note, pure hyperbola and ellipse events are only true for isotropic case

parent, the Kebaili and Schmitt (1997) method successfully measures the constant phase velocity of 3500m/s with an error of ±50m/s due to picking uncertainty. Assuming a point source and a sufficient number of point receivers, the picking in the (τ, p) transform can be done consistently on first arrival, peak, or trough within this error range.

Next, the same finite-difference transmission gathers are repeated, using source and receivers with the size of 13mm. The receivers were attached to the top surface, and the source receiver at the side of the layer with its top edge at the depths of d_1 and d_2. Figure 2.7b shows the measured phase velocity comparing the results when it was picked on the first arrival, peak or trough. The measured phase velocity has the error range of ±400m/s whether peak or trough was picked (Figure 2.7b), and seems more accurate with the error of ±150m/s when first arrival was used. Such large errors can be believed that are related to the loss of resolution caused by the finite-size sources and receivers, which was simulated by using source/receiver arrays. Essentially, the array effect is a spatial averaging and the resulting distortion is less for first arrivals than for subsequent arrivals. For physical model data acquired over anisotropic models, this wave interference plus the presence of noise in the data reduces the reliability of phase velocity measurements. Hence, for phase velocity measurements smaller transducers, resembling point sources and receivers, as used in Mah and Schmitt (2001a), are desired. This contrasts with the results in the previous section where we showed that the measurement of group velocity is less sensitive to transducer size.

2.4 Group velocity measurements over the phenolic layer

3C transmission seismic data over the phenolic model were collected to facilitate the group velocity measurements. The vertical, radial, and transverse component data were acquired, utilizing P-transducers, radially polarized S-transducers, and transversely polar-

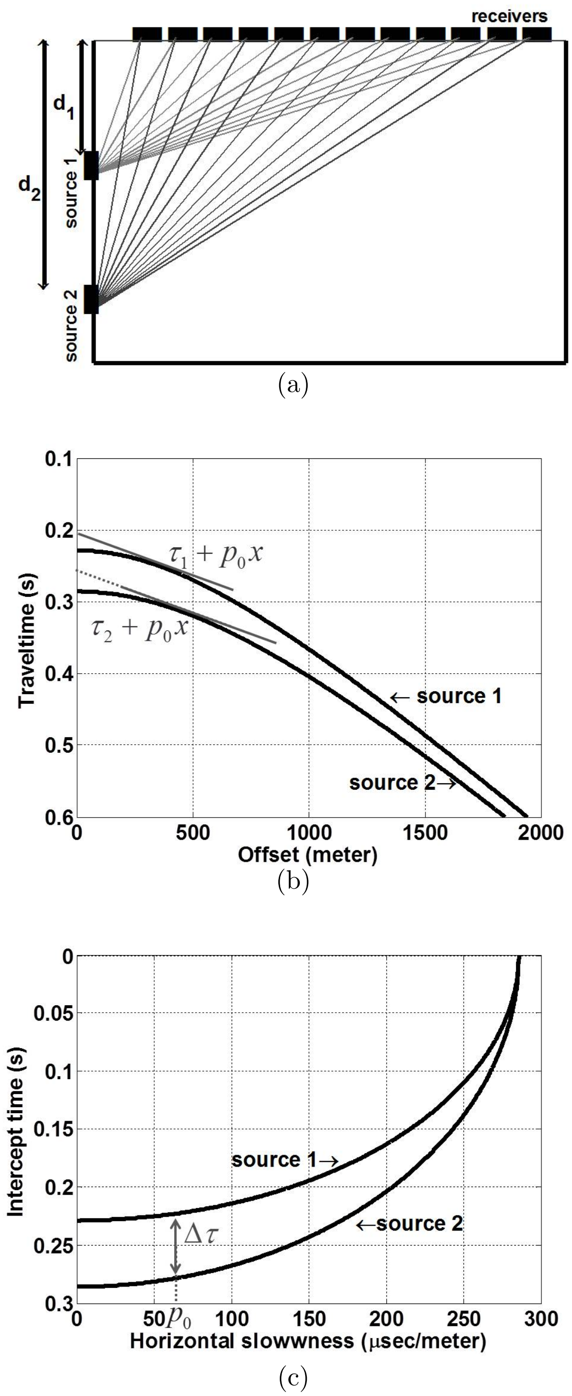

Figure 2.5: (a) Schematic view of the acquisition geometry of the two transmission gather required for measuring the phase velocity. (b) The two traveltime versus offset curves for the two transmission gathers with different source positions. (c) (τ, p) transforms of the traveltime curves in (b), note the determination of $\Delta\tau$ at a given constant horizontal slowness p_0 (Mah and Schmitt, 2001a).

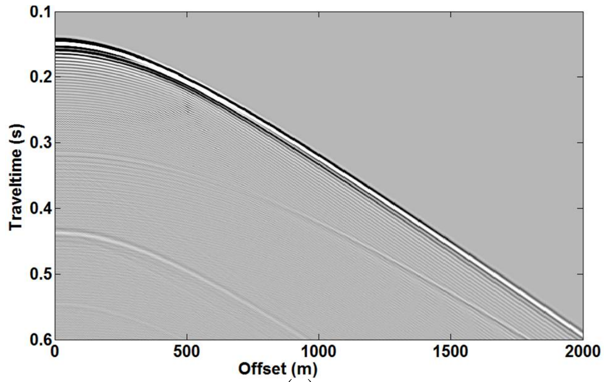

(a)

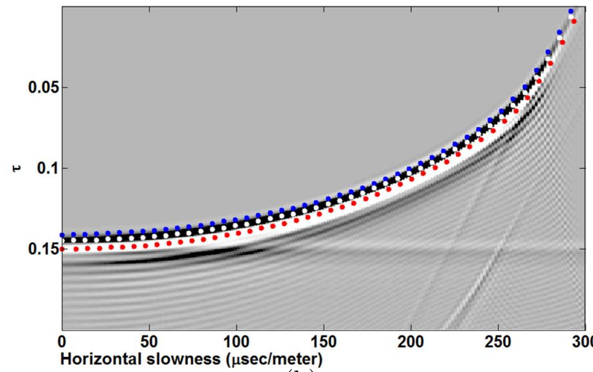

(b)

Figure 2.6: (a) Finite-difference generated transmission gather assuming point source and receivers, with the shot depths at $d_1 = 500m$, over a constant velocity layer with the velocity of 3500m/s. (b) The (τ, p) transform of the gather in (a), the picks on first breaks are shown in blue, on peaks are shown in white, and on trough are shown in red. Two of such transmission gathers, with the shot depths at $d_1 = 500m$ and $d_2 = 400m$, were used in the estimation of phase velocities.

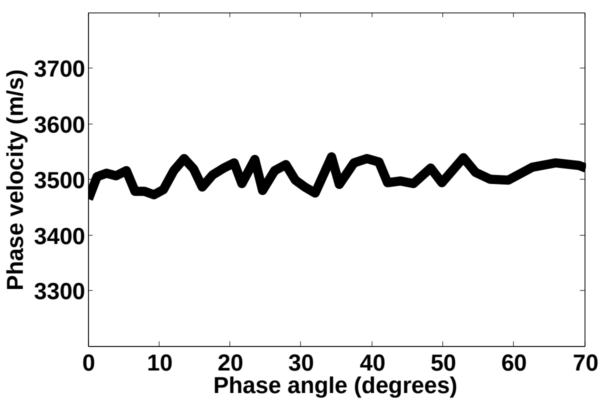

(a)

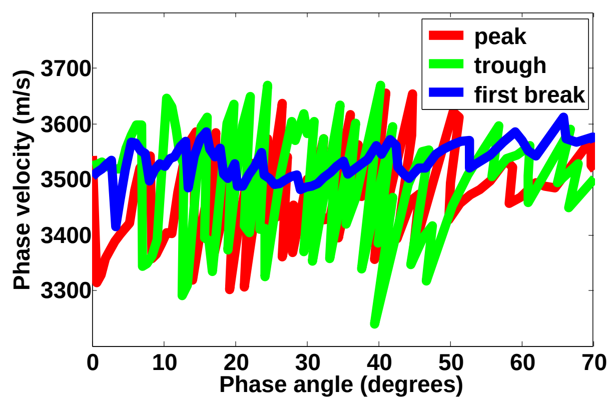

(b)

Figure 2.7: Phase velocity measured from finite-difference data gathered over an isotropic layer with the constant velocity of 3500m/s. (a) Point source and receiver data. (b) 13mm transducer data.

ized S-transducers, as source and receivers, respectively. For each component, the source and receiver transducers always had identical polarizations. The P- and S-transducers are Panametric $V103$ and $V153$ with diameter of a 13 mm and a nominal central frequency of 300 kHz. The reference Cartesian coordinate system used for the was chosen with to be the same as the orthorhombic symmetry system. As the symmetry of phenolic materials is relatively well controlled, the Cartesian axes were aligned with the symmetry planes of the phenolic layer. Figure 2.8 shows the 3C data from one of the transmission shot gathers. The shear-wave splitting phenomenon is observed between the radial and transverse components, with the zero-offset arrivals of the qS_V- and qS_H-waves at approximately 0.45ms and 0.41ms respectively.

The transmission receiver lines were positioned along azimuths of 0°, 90°, 45°, and 135° at the top surface (Figure 2.9a-d) with the source located at the bottom, and 0°, 90° azimuth lines at the top surface with the source also at the top with a distance from the receiver line (Figure 2.9e-f). The group velocity along different directions in the (x_1, x_3), (x_2, x_3), azimuth 45°, and azimuth 135° planes are estimated from the transmission profiles in Figure 2.9a-d. The group velocity along different directions in the (x_1, x_2) plane are estimated from the profiles in Figure 2.9e-f. The qP and qS velocities along the (x_1, x_2, x_3) axes are listed in Table 2.2. The errors of ±70m/s and ±35m/s are considered for the qP- and qS-velocities measured from physical model data, using 0.1mm error in distance and 0.004s error for first arrival time picks (1/8 of the dominant wavelength). To examine how much heterogeneity effects the velocity measurements, these measurements are also repeated by a pulse through transmission on several phenolic slabs individually. It is found that the mean values are within the range of error from the ones measured from transmission seismic data. This indicates the validity of the homogeneous assumption for the experimental phenolic layer.

The qP group velocities are determined from qP first arrival traveltimes picked on

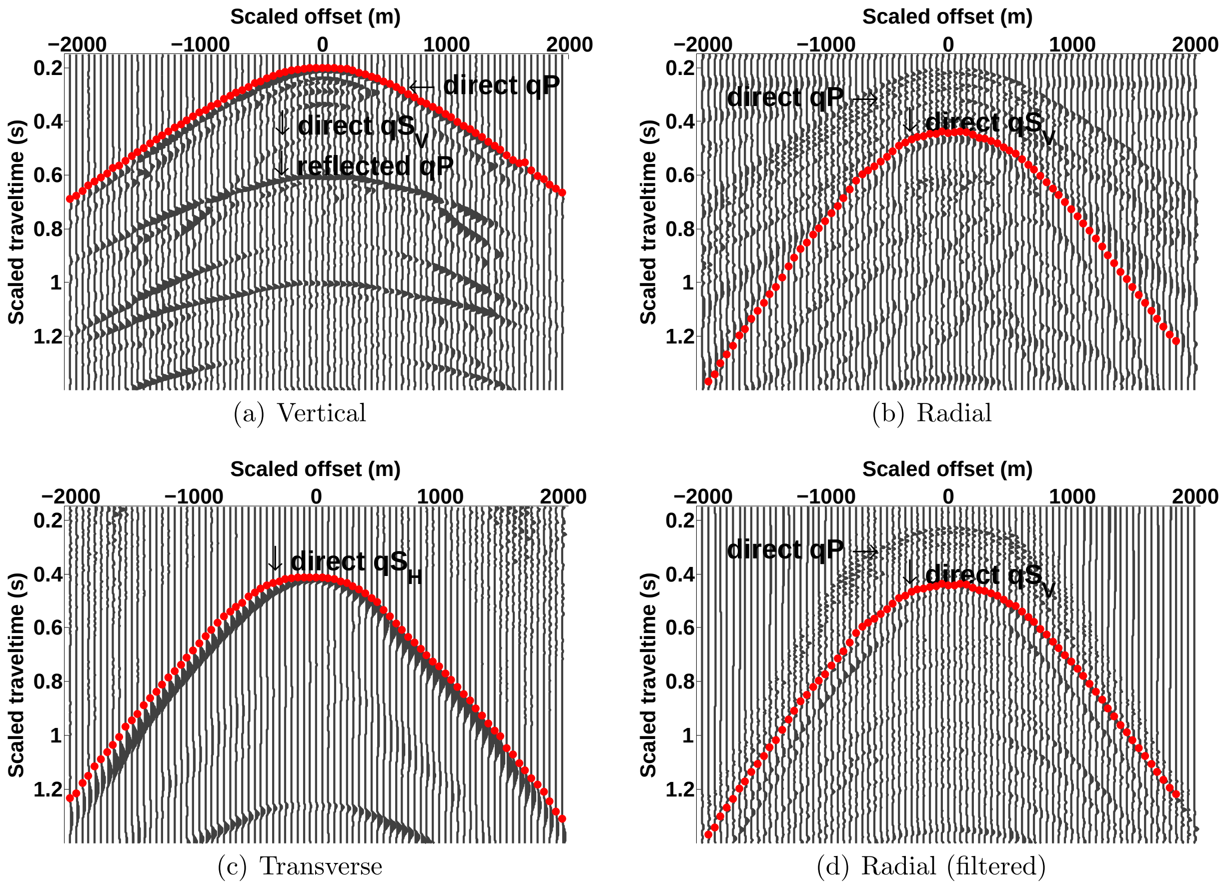

(a) Vertical (b) Radial (c) Transverse (d) Radial (filtered)

Figure 2.8: The 3C transmission data acquired along the x_1-axis (Figure 2.9a), with the wave propagation at the (x_1, x_3) plane. (a) Raw vertical-component data. (b) Raw radial-component data. (c) Raw transverse-component data. (d) Filtered radial-component data (radial filtering). Red dots are first arrival picks of each mode. Displayed data have a long-gate automatic gain control applied for the vertical and transverse components. The radial component data have been displayed with a shorter window automatic gain control to boost the direct qS_V arrival. The three components have similar noise levels.

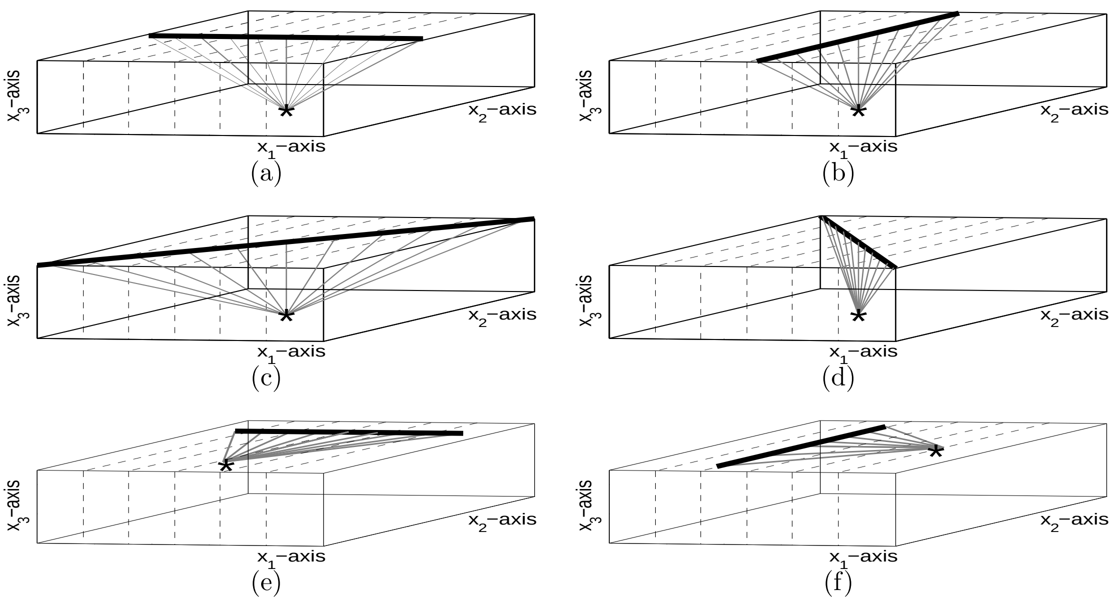

Figure 2.9: Transmission profiles. Receiver lines are shown with bold lines, sources by $\star$, the raypaths connecting source-receivers with thin lines, slab joints with dash lines. (a-d) Receiver lines at top surface along 0°, 90°, 45°, and 135° (with respect to x_1-axis), with the source at bottom surface. (e-f) Receiver lines at top surface along 0°, and 90° with the source also at the top surface.

the vertical component data. The qS$_V$ and qS$_H$ group velocities are obtained from the qS-wave first arrivals picked on the radial and transverse data components. The qP and qS$_H$ first arrivals are strong and easy to pick. The qS$_V$ first arrivals, however, are more difficult to identify and pick (Figure 2.8) from raw radial component data. The qS$_V$ first arrivals, however, are more difficult to identify and pick (Figure 2.8) from raw radial component data. The horizontal component of the reflected qP-wave appears rather strong in the radial-component data, and because of its velocity (almost twice that of the shear waves) greatly interferes with the first arrivals of the qS$_V$-wave, making the picking of the direct arrival of the qS$_V$-wave difficult, especially for the middle-angle range. To overcome this difficulty, radial trace filtering (Henley, 2003) was applied to the radial component data (see Appendix G for a description of radial trace filtering). This estimate-and-subtract method attenuates the interference from events whose local

Table 2.2: Phenolic qP- and qS-velocity (m/s) in principal directions. Here V_{ij} ($i, j = 1, 2, 3$) is the body wave velocity which propagates along the x_j-axis and polarized along the x_i-axis. For example V_{11} is the qP-wave velocity propagating along the x_1-axis, and $V_{23}(= V_{32})$ is the qS-wave velocity propagating along the x_3-axis and polarizing along the x_2-axis.

V_{11}	V_{22}	V_{33}	V_{23}	V_{13}	V_{12}
2950 ± 70	3640 ± 70	3500 ± 70	1700 ± 35	1530 ± 35	1510 ± 35

dip differs from that of the qS_V first arrival event. Done carefully, this type of the radial trace filtering does not introduce traveltime changes to the target event (static shift) and also preserves the amplitude (Henley, 2003).

The qP and qS group velocity surfaces for the symmetry planes, polar plots of group velocity versus propagation angle are shown in Figure 2.10. The qS_H wavefronts are purely ellipsoidal. The qP wavefronts deviate slightly from the ellipsoidal with smaller velocities (at middle-angle range) compared to the ellipse. The qS_V wavefronts also deviate from the sphere with slightly larger velocities (at middle-angles range) compared to the circle.

2.5 Determining A_{ij}, the density-normalized elastic constants

The diagonal A_{ij} are determined from direct measurements of qP- and qS-wave velocities, obtained from transmission traveltimes, along the x_1-, x_2-, and x_3-axes. The off-diagonal A_{ij} are determined from the linear inversion of the measured qP group velocities along various directions, as explained previously. The estimated A_{ij} of the experimental phenolic layer, and their statistical uncertainties are listed in Table 2.3. The statistical uncertainties are estimated by introducing small random perturbations, representing uncertainty, in the measured group velocities and observing the corresponding changes in the A_{ij}.

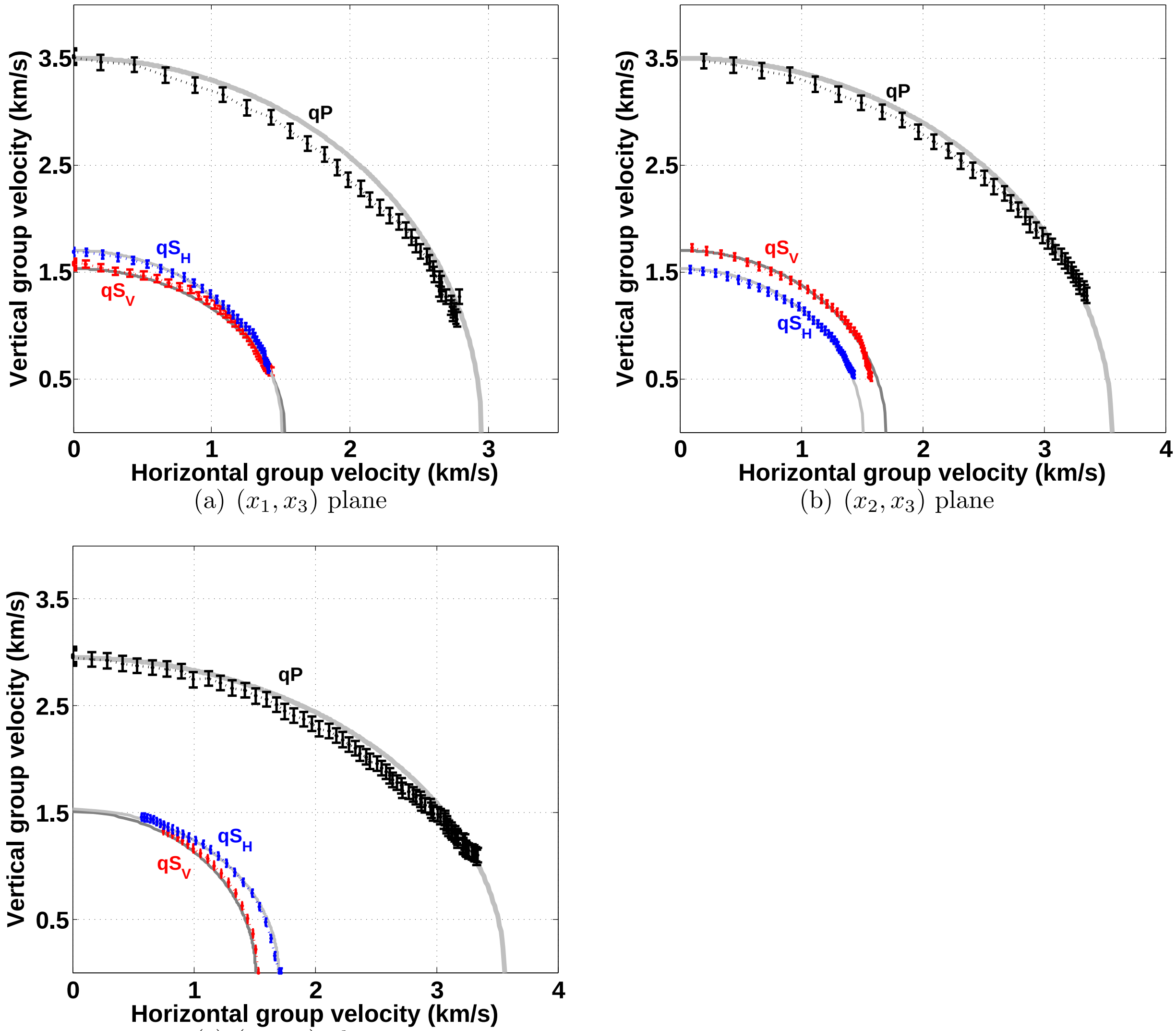

(a) (x_1, x_3) plane

(b) (x_2, x_3) plane

(c) (x_1, x_2) plane

Figure 2.10: The group velocity surfaces for the three modes (qP, qS_V, qS_H) in the three symmetry planes. An elliptical wavefront is plotted for comparison in solid. The measured velocities in the 0° and 90° directions, are considered to be the major and minor axes of the ellipse. Group angles are plotted with respect to the vertical axis for the (x_1, x_3) and (x_2, x_3) planes, and with the x_1-axis for the (x_1, x_2) plane.

2.5.1 Verification of the accuracy of estimated A_{ij}

As an accuracy test for the estimated A_{ij}, the phase and group velocities predicted by these estimations are calculated, and compared to the measured velocities. First the predicted phase velocities are calculated and then their values are used to calculate the group velocities. The exact explicit orthorhombic phase velocity expression, for the symmetry planes, is given by Tsvankin (2001), and the expression relating the phase and group velocities is given in Appendix C. For the symmetry plane, Figure 2.11 compares the measured qP group velocities from transmission data collected by 1.33mm transducers and group velocities calculated from the estimated A_{ij}. The theoretical velocities match the measured velocities reasonably well. Some small discrepancies between the theoretical group velocities and measured group velocities could be due to our assumption of homogeneity of the simulated fractured layer or employing an approximate orthorhombic group velocity expression rather than the exact form.

Table 2.3: Density-normalized stiffness coefficients of the simulated fractured layer. The A_{ij} have the units of $(\mathrm{km/s})^2$.

$$\begin{vmatrix} 8.70 \pm 0.49 & 4.68 \pm 0.21 & 5.07 \pm 0.21 & 0 & 0 & 0 \\ & 13.25 \pm 0.49 & 5.13 \pm 0.23 & 0 & 0 & 0 \\ & & 12.25 \pm 0.49 & 0 & 0 & 0 \\ & & & 2.89 \pm 0.12 & 0 & 0 \\ & & & & 2.34 \pm 0.12 & 0 \\ & & & & & 2.28 \pm 0.12 \end{vmatrix}$$

2.6 Phase velocity measurements over the phenolic layer

For each of the symmetry planes, two transmission seismic data gathers with sources at two different depths from the receiver plane are acquired. This is the geometry studied above and used by Kebaili and Schmitt (1997) to estimate phase velocities. The P-

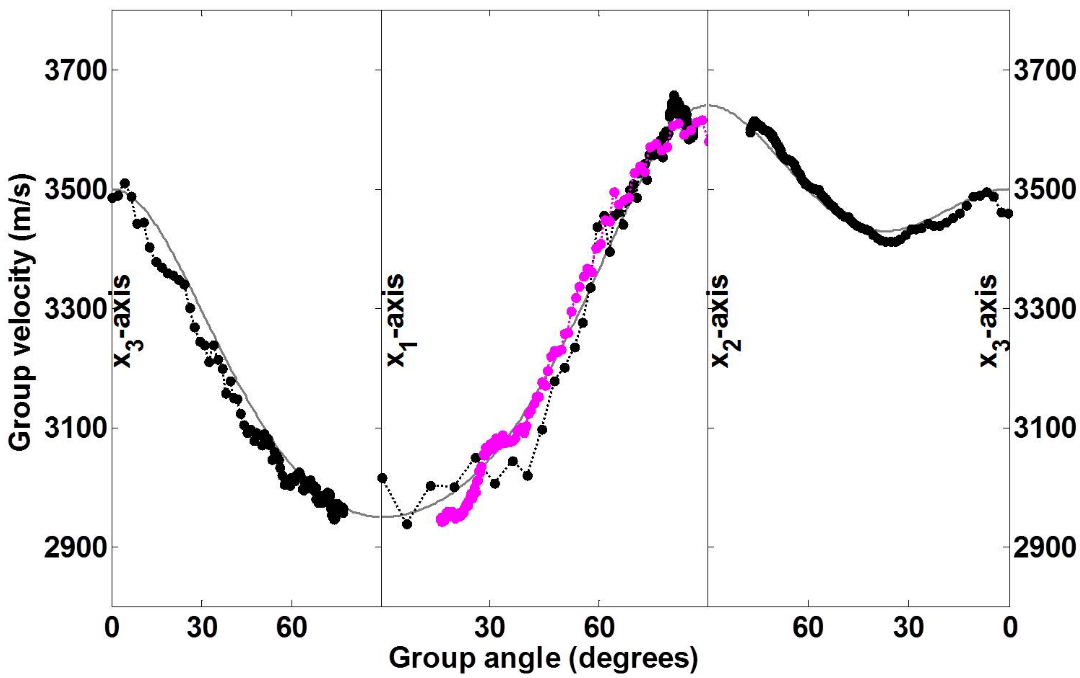

Figure 2.11: The group velocities versus propagation angle in the symmetry planes (x_1, x_3), (x_2, x_3) and (x_1, x_2). The solid gray lines are theoretical velocities and the dotted lines are measured ones. In (x_1, x_2) plane the black dotted line measured from a receiver profile along x_2-axis, the magenta dotted line measured from a receiver profile along x_1-axis.

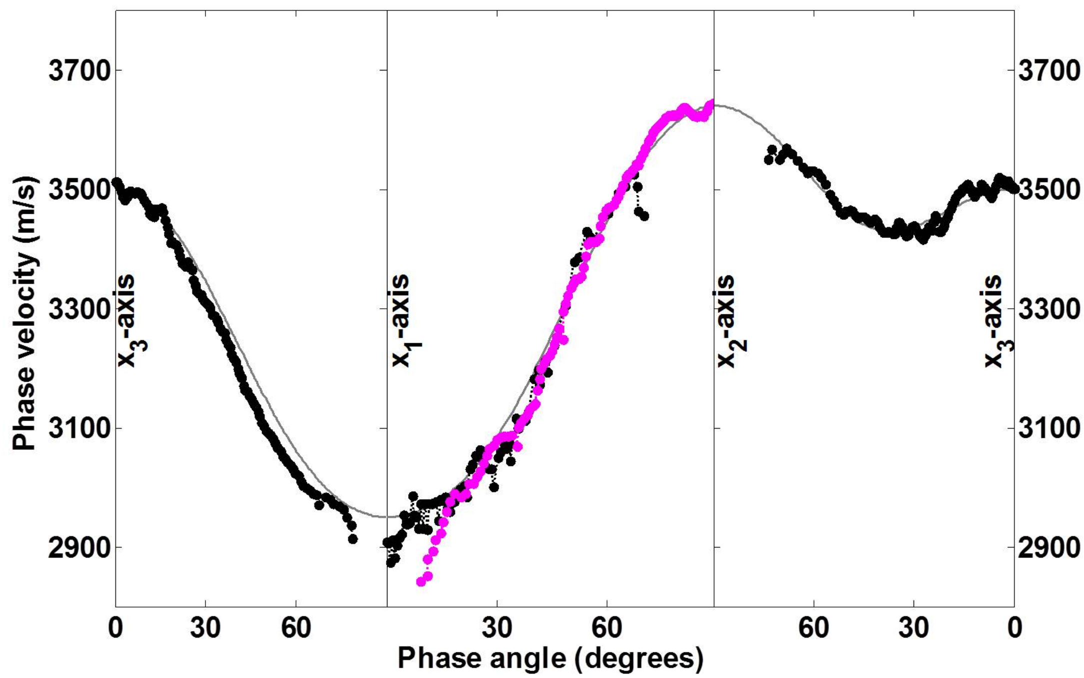

Figure 2.12: The phase velocities versus phase angle in the symmetry planes (x_1, x_3), (x_2, x_3) and (x_1, x_2). The solid gray lines are theoretical velocities and the dotted lines are measured ones. In (x_1, x_2) plane the black dotted line measured from a receiver profile along x_2-axis, the magenta dotted line measured from a receiver profile along x_1-axis.

transducers (piezoelectric pin CA-1136) with each piezoelectric element being 1.33mm in diameter is used to produce the vertical component data. Using the method discussed in Kebaili and Schmitt (1997), the phase velocities for the three symmetry planes are measured. A great care picking on the (τ, p) transforms is been taken, a small window AGC used in order to enable a consistent first arrival picking. The measured phase velocities are compared to the theoretical velocities predicted from the estimated A_{ij} (Figure 2.12). Good agreement within the error range of velocity measurements was obtained. This indicates that the estimated A_{ij} from group velocity measurements are able to be used to obtain the phase velocities with high accuracy. The estimated phase and group velocities for the symmetry planes are compared together in Figure 2.13. The phase velocities have larger values than group velocities except for the principal directions that they are equal.

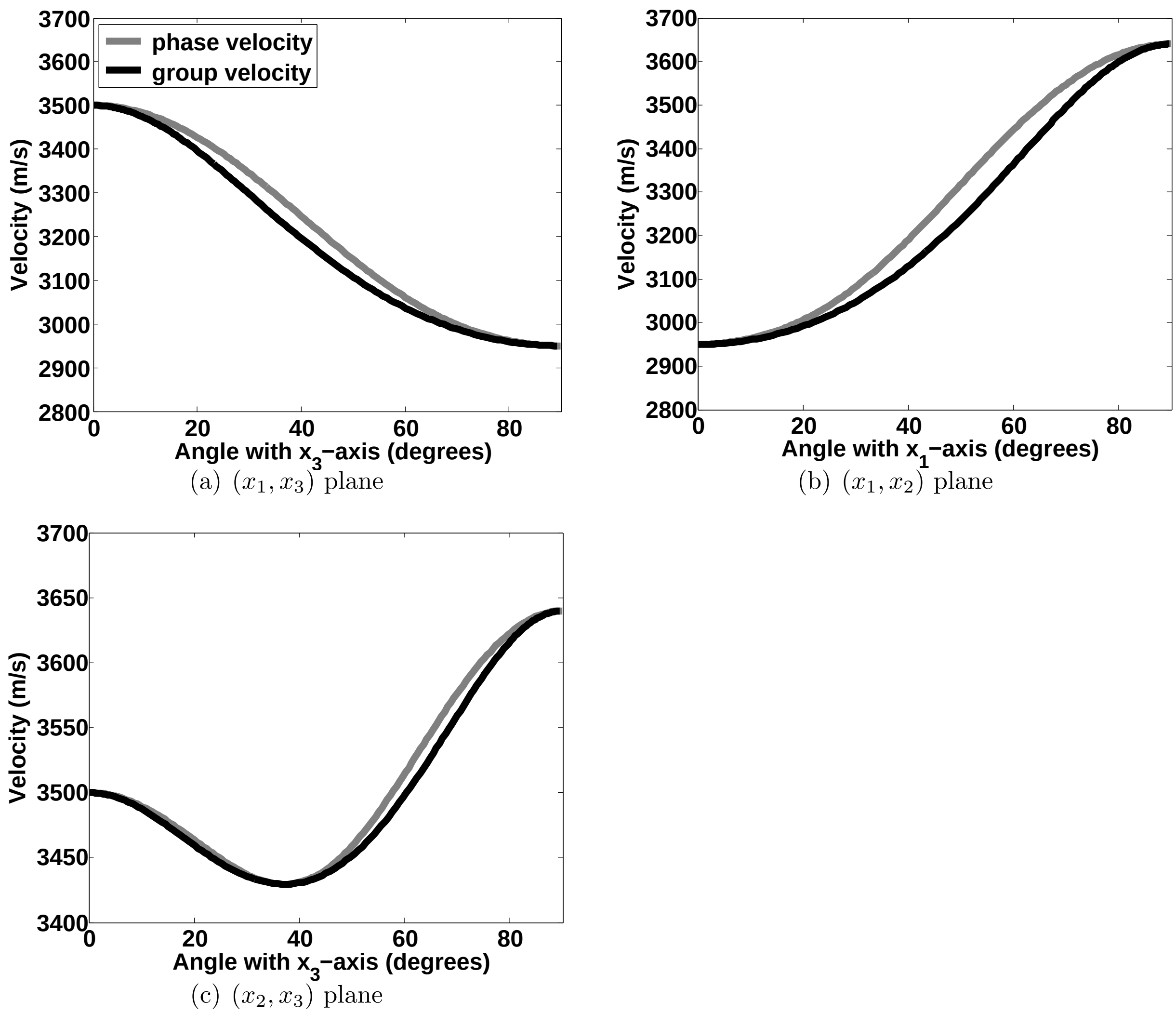

Figure 2.13: Comparison of the estimated phase and group velocities in the symmetry planes. The phase and group velocities are plotted versus phase and group angles respectively.

2.7 Thomsen-style anisotropy parameters

The stiffness coefficients, A_{ij} of the experimental phenolic layer characterize the anisotropy of the medium, while the strengths of anisotropy are less obvious. The dimensionless orthorhombic anisotropic parameters are defined in Tsvankin (1997), and express the measure of anisotropy similar to the well-known Thomsen (1986) coefficients ϵ, δ, and γ for VTI media. Using expressions for the orthorhombic parameters in terms of the stiffness coefficients, given in Table 2.7, these anisotropy parameters for the experimental phenolic layer and their statistical uncertainties are listed in Table 2.4.

Table 2.4: Values of the orthorhombic anisotropic parameters of the phenolic layer.

$\delta^{(2)} = -0.178 \pm 0.002$	$\delta^{(1)} = -0.102 \pm 0.001$	$\delta^{(3)} == 0.066 \pm 0.004$
$\epsilon^{(2)} = -0.145 \pm 0.003$	$\epsilon^{(1)} = 0.041 \pm 0.0003$	$V_{P0} = 3500 \pm 70$ m/s
$\gamma^{(2)} = -0.106 \pm 0.002$	$\gamma^{(1)} = -0.013 \pm 0.0003$	$V_{S0} = 1700 \pm 35$ m/s

The values of the A_{ij} reveal that the experimental layer approximates an HTI medium with the x_1-axis being the symmetry axis and the (x_2, x_3) plane is a nearly isotropic plane. The x_1-axis with a qP-velocity of 2950m/s can be considered as the slow direction, and the (x_2, x_3) plane with the fast velocity of $3570m/s$ (average of 3640m/s for x_2-axis, and 3500m/s for x_3-axis) can be considered as the fast plane. The qS-velocity in the (x_1, x_3) and (x_1, x_2) planes (slow planes) are 1520 (average of 1510m/s and 1530m/s), and in the (x_2, x_3) is 1700m/s. If we treat the experimental phenolic layer as an HTI medium with the x_1-axis as the symmetry axis, the five effective HTI anisotropic parameters required in investigating the azimuthally AVO responses of the medium $(\alpha, \beta, \epsilon^{(V)}, \delta^{(V)}, \gamma)$, defined by Rüger (2001) (Table 2.5), are as in Table 2.6.

Converting these HTI parameters to their equivalent Thomsen (1986) coefficients ϵ, δ, and γ which carry the conventional meaning of anisotropy, the fractional differences

Table 2.5: Anisotropy parameters for an HTI medium with the symmetry axis along the x_1-axis (Rüger, 2001).

$\epsilon^{(V)} = \dfrac{A_{11} - A_{33}}{2A_{33}}$	$\delta^{(V)} = \dfrac{(A_{13} + c_{55})^2 - (A_{33} - A_{55})^2}{2A_{33}(A_{33} - A_{55})}$	$\gamma = \dfrac{A_{44} - A_{55}}{2A_{55}}$

Table 2.6: Anisotropic parameters of the simulated HTI layer.

$\alpha = V_{P0} = 3500\text{m/s}$
$\beta = V_{S0} = 1700\text{m/s}$
$\delta^{(V)} = \delta^{(2)} = -0.185$
$\epsilon^{(V)} = \epsilon^{(2)} = -0.145$
$\gamma = \frac{A_{44}-A_{55}}{2A_{55}} = 0.117$

of the fast and slow velocities, results in the following values: $\epsilon = 0.204, \gamma = 0.117$, and $\delta = -0.15$. These values indicate the weak anisotropy (defined as $\epsilon, \delta, \gamma \ll 1$) for our experimental phenolic layer.

Table 2.7: Tsvankin (1997) orthorhombic parameter relations to the stiffness coefficients.

$\delta^{(2)} = \frac{(A_{13}+A_{55})^2-(A_{33}-A_{55})^2}{2A_{33}(A_{33}-A_{55})}$	$\delta^{(1)} = \frac{(A_{23}+A_{44})^2-(A_{33}-A_{44})^2}{2A_{33}(A_{33}-A_{44})}$	$\delta^{(3)} = \frac{(A_{12}+A_{66})^2-(A_{11}-A_{66})^2}{2A_{11}(A_{11}-A_{66})}$
$\epsilon^{(2)} = \frac{A_{11}-A_{33}}{2A_{33}}$	$\epsilon^{(1)} = \frac{A_{22}-A_{33}}{2A_{33}}$	$V_{P0} = \sqrt{A_{33}}$
$\gamma^{(2)} = \frac{A_{66}-A_{44}}{2A_{44}}$	$\gamma^{(1)} = \frac{A_{66}-A_{55}}{2A_{55}}$	$V_{S0} = \sqrt{A_{55}}$

2.8 Discussions

In this chapter the group velocity in various directions are obtained by measuring direct-arrival traveltimes on physically modeled 3C transmission gathers acquired by 13mm transducers which are commonly used in physical modeling. The effect of relatively large physical model transducers were mitigated by using a single geometric edge-to-edge correction assuming a known effective diameter for the transducers. The effective diameter of the large transducers should be carefully decided from velocity measurements over a known isotropic layer in advance to any anisotropic experiment. The qP-velocity measurements by 13mm transducers were consistent with the ones by smaller transducers. The qS_V-waves from 13mm transducers were difficult to identify and pick. Hence it is not clear that the edge-to-edge correction is as effective as it was for qP-waves. Because the small S-transducers were not available at the time of this experiment, the difficulty in picking might be due to existence of shear-wave singularity for the phenolic experimental layer. Acquiring physical model data with small S-transducers might be considered to solve this difficulty. Using very small point transducers, the measurements of group velocities obviously will not need an extra edge-to-edge correction. However, very small transducers do not usually produce a powerful enough signal for the large physical models. In addition, they have coupling issues.

The group velocity measurements are easy and straightforward but the theoretical linkage between group velocities and stiffness coefficients is not well known. However, the energy propagation, group velocities are the ones normally resulting from seismic gathers, including the NMO velocities. The author wishes to draw the readers attention to the approximate group velocity expression of Daley and Krebes (2006) and suggest that is has significant practical utility. A qP group velocity approximation in a general 21-parameter weakly anisotropic medium is presented in Daley and Krebes (2007). An approximation for orthorhombic qS-waves is also available (Song and Every, 2000).

The characterization of physical models is usually done by employing the phase velocities, as the theoretical link between stiffness coefficients and phase velocities are well understood. Accurate measurement of phase velocities, however, is more difficult than group velocities and the results depend strongly on the size of the transducers used. It

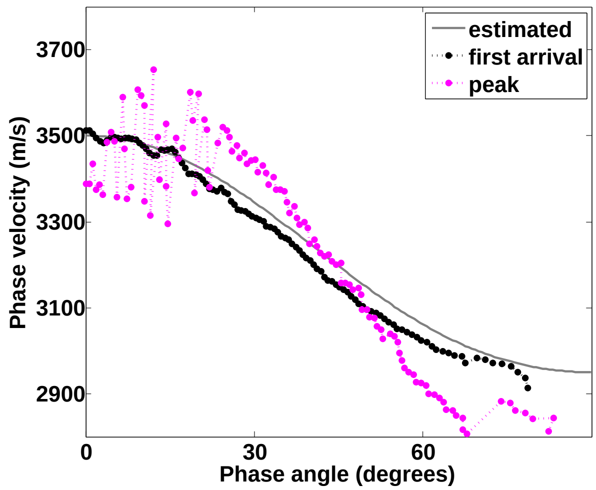

Figure 2.14: Measured phase velocity picked on first arrival compared to picked on strong peak.

been shown that the phase velocities measured, using the (τ, p) transform analysis of 1.3mm transducers, by a careful picking on first arrivals of the (τ, p) ellipse, are consistent with the theoretical phase velocities predicted by stiffness coefficients estimated by inversion of the group velocity measurements. Picking consistently on the strong peak or trough of the ellipse will result in different trends for the phase velocities (Figure 2.14). The wavefront generated by individual points on the large transducers are superimposed. Thus the requirement of picking along a wavefront from a point source is violated.

Homogeneity of the simulated fractured medium is assumed in this work, so it is believed that the frequency dispersion in this experimental layer in minimal. The observed changes in the wavelet, in our transmission data, should be due mainly to the effect of transducer size (Figure 2.3). A P-wave shot gather is numerically modeled over an isotropic homogenous model with the dimensions of our simulated fractured layer, using finite difference modeling with the source and receiver array length equal to our transducer's size. This modeling indicates the apparent change in wavelet shape from near to far offset is due mostly to the large size of the source and receiver transducers rather than a frequency dispersion effect (Figure2.15).

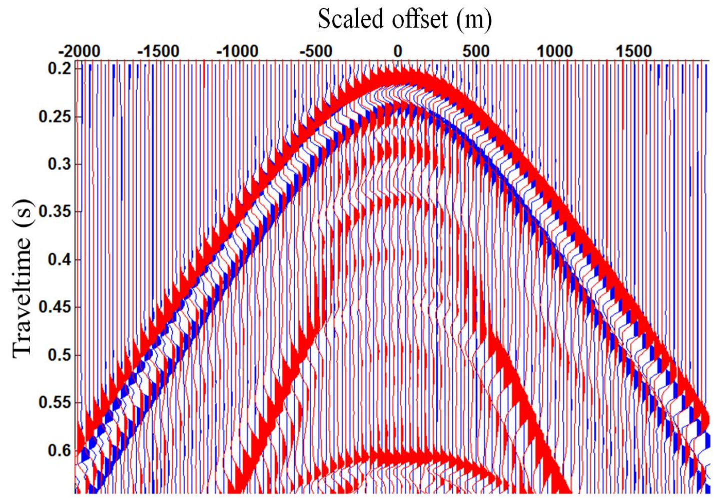

Figure 2.15: (blue) P-wave transmission gather generated by finite-difference acoustic modeling over an isotropic layer with the velocity of 3500m/s. (red) Vertical component data acquired at (x_1, x_3) plane. Here the focus is direct arrival qP-wave. There is good match for wavelet at the near-offset traces. Because of anisotropy and increasing velocity toward x_1-axis, the two seismic gathers do not quite match at the far-offset traces.

2.9 Summary

A straightforward method to characterize an orthorhombic material in a physical modeling setting is presented. The utility and value of group-velocity measurements to estimate the stiffness coefficients is demonstrated. After the edge-to-edge correction, correcting for the size of the transducers, the qP-velocity measurements are found to be less sensitive to transducer size. qP phase velocities are determined from the (τ, p) transform analysis of transmission data acquired by very small transducers, resembling point sources and receivers. It is shown that the accuracy of the phase velocities is greatly dependent to the size of the transducers used.

Our inversion method is based on a relatively new approximate relationship between group velocity and orthorhombic stiffness coefficients. The orthorhombic qP velocity expression by Song and Every (2000) and Daley and Krebes (2006) enables in off-diagonal stiffness coefficients estimates. It is showed that the estimates of stiffness coefficients, for our physical layer, are consistent with the qP group and phase velocity data, by comparing measured group and phase velocities produced by small transducer data with the calculated theoretical velocities predicted by the estimated stiffness coefficients. The estimated density-normalized stiffness coefficients suggest that the experimental phenolic layer, with relatively well controlled symmetry, approximates a weakly anisotropic HTI layer, or equivalently a vertically fractured transversely isotropic layer.

Chapter 3

3D physical model reflection data for azimuthal AVA

The next step for physical modeling to become more upstream is the verification of the suitability of physically modeled data in a quantitative amplitude analysis. A seismic experiment utilizing a physical geological model has been conducted to acquire single-component, multi-offset, multi-azimuth, 3D reflection seismic data, to verify the suitability of physically-modeled data for AVAZ (amplitude variation with angle and azimuth) analysis. This chapter details the acquisition and the processing of the physical model reflection data.

The model consisted of five layers with the phenolic layer, simulating a vertically fractured medium with a single set of fractures, in the middle. Two isotropic media layers were above, and two below the anisotropic (fractured) layer with the uppermost and lower layers being water. The upper and lower layers welded to the phenolic layer were homogeneous isotropic plexiglas.

The amplitudes reflected from the top of the fractured layer, the target event, have been picked from the primary reflection. The acquisition was designed to avoid the overlapping of the primary and ghost events. Data have been filtered to avoid the wave interferences from the top reflectors, to enable amplitude picking of the target event. The picked reflection amplitudes have been corrected using standard AVO corrections for marine data, and additionally, a directivity correction has been applied to compensate for the effects of the large physical model transducers. A successful quantitative investigation of the AVO behavior of the P-wave reflections, from the two isotropic-isotropic (water-plexiglas) and isotropic-anisotropic (plexiglas-phenolic) interfaces, which agreed with the theoretical predictions, is presented. The corrected reflection amplitudes from the plexiglas-phenolic interface will be used for AVAZ analysis of Chapter 4.

3.1 Laboratory set-up

The model consists of five layers, which are water (scaled thickness: 700 m), plexiglas (scaled thickness: 500 m), simulated fractured layer (scaled thickness: 690 m), plexiglas (scaled thickness: 250 m), and water (scaled thickness: 300 m) (Figure 3.1). The simulated fractured layer and the two plexiglass layers were machined, to ensure flat and smooth surfaces, and were glued with melted wax and placed in a high pressure environment to cure so as to ensure the simulation of a welded contact. These three layers were submerged in a large water tank and located above the base water layer by adjustable screws fastened near the corners of the tank. The adjustable screws allow for accurate leveling of the model. The model was leveled carefully to ensure that the interfaces had no dip, by equating the reflection traveltimes from the upper interface at each corner, within the limits of the experimental recordings of the system. Some elastic properties of the modeling material are listed in Table 3.1. The complete elastic properties of the anisotropic phenolic layer was presented in Chapter 2 (table 2.3).

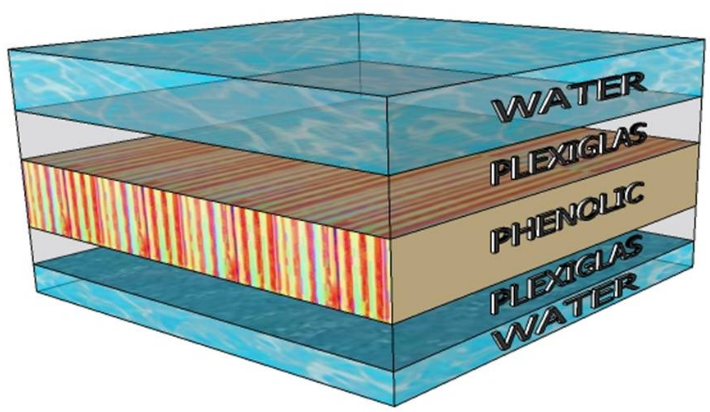

Figure 3.1: The five-layered earth model used in the acquisition of 3D reflection data.

As receivers these transducers simulated vertical component geophones. These trans-

	P-velocity (m/s)	S-velocity (m/s)	Density (g/cc)
Water	1485	~ 0.0	1.00
Plexiglas	2745	1380	1.19
Phenolic	3570 ($\|$) 2900 ($\perp$)	1700 ($\|$) 1520 ($\perp$)	1.39

Table 3.1: A summary of the physical properties of the materials used.

ducers produced an acoustic wavelength of ~ 2.8mm, corresponding to a wavelet with a scaled center frequency of 52Hz for P-waves. In this experiment a strong voltage (325 V) was used to image the reflection from the top of the fractured layer without clipping the first reflector amplitudes.

For the reflection data, the first source- and receiver-transducer location are manually positioned according to a predefined coordinate system. The source and receiver arms should be reset according to this one coordinate system. Having finite-size transducers, this coordinate assignment is not perfect; as for the origin this is set visually. Therefore, the effective first source-receiver distance is not automatic. To check the accuracy of the first source-receiver offset using the positions of the receivers (from trace headers), the first-break traveltimes can be fitted by least-squares to obtain the first source-receiver offset and the accurate velocity of the first (water) layer. Determining the first source-receiver offset is explained in Appendix D. As previously mentioned, once the initial source-receiver offset is set, the subsequent increments in offset are computer controlled, and as a consequence are accurately known.

3.2 Data acquisition

A common-midpoint (CMP) shooting arrangement similar to that employed in Chang and Gardner (1997) is used. The seismic traces are gathered with respect to one CMP point for a range of offsets and azimuths. The acquisition coordinate system was chosen to coincide with the symmetry planes of the fractured layer; the vertical is the x_3-axis, the x_1-axis is aligned with the symmetry axis, and the x_2-axis coincides with the fracture plane of the simulated fractured layer (Figure 3.2). A total of nine large-offset CMP seismic lines were recorded along azimuthal directions of 0°, 14°, 27°, 37°, 45°, 53°, 63°, 76°, and 90° measured from the x_1-axis. Figure 3.2 shows the acquisition geometry. During data acquisition, elastic waves were generated and received by a source-receiver pair starting with (S_1, R_1), collecting the first trace of each azimuth line. The source-receiver pair was then moved outwards to collect other traces at the current azimuth. As the robotic positioning system was only able to make movements along the principal axis of x_1 and x_2, to acquire the azimuth lines the source and receiver were moved at $(\Delta x, \Delta y)$ intervals. The scaled $(\Delta x, \Delta y)$ intervals are $(40, 0)$, $(40, 10)$, $(40, 20)$, $(40, 30)$, $(40, 40)$, $(30, 40)$, $(20, 40)$, $(10, 40)$, and $(0, 40)$, corresponding to the nine azimuths, respectively. The maximum scaled offset is 3100m, mapping a CMP point at the top of the fractured layer to the scaled depth of 1890m.

Figure 3.3 shows the CMP seismic line acquired along an azimuth of 0° (fractured symmetry axis) and 90° (fracture plane), with the transducers' tip at the water surface. Five events are recognizable from the reflection data. The three strong PP reflections from the plexiglass top (labeled "A"), fracture top (labeled "B") and base layer (labeled "E"), a strong PS reflection from the fracture top (labeled "C"), and a weak PP reflection from the bottom of the fractured layer (labeled "D"). The reflections from the plexiglas top and fractured top (labeled "A and "B"), appearing at approximately 0.95s and 1.3s,

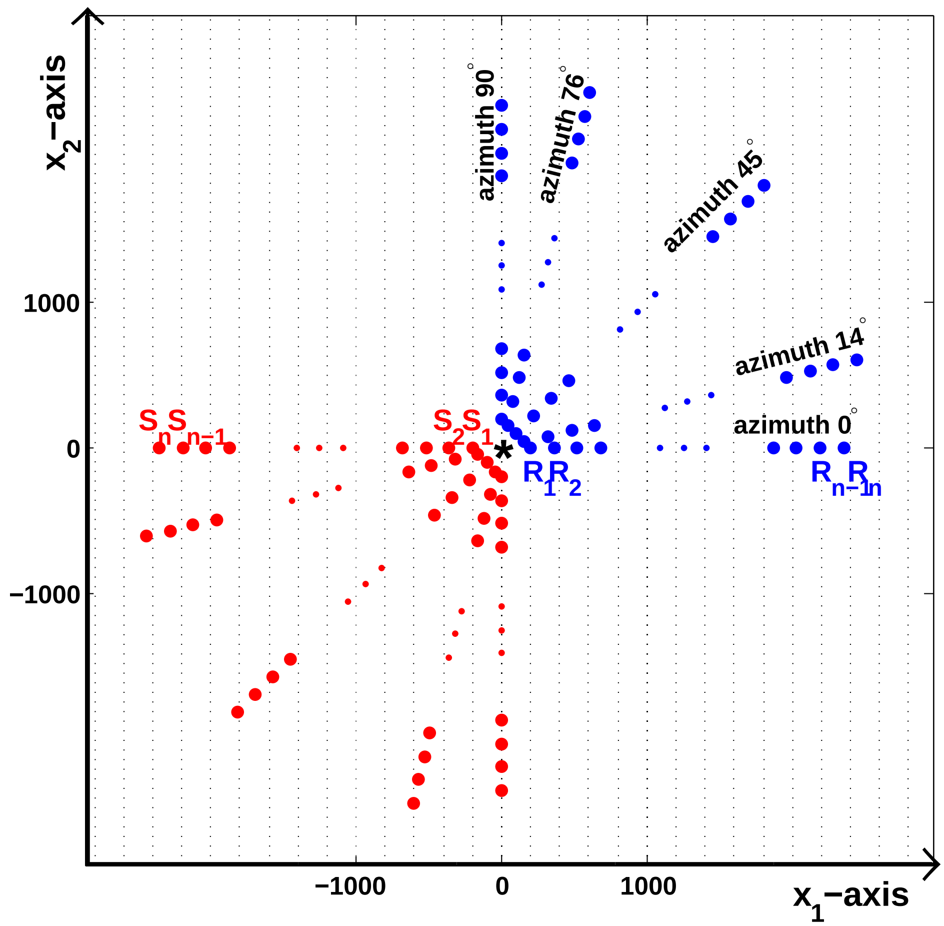

Figure 3.2: A map view of the acquisition geometry of the CMP survey lines. The thin background lines schematically display the fracture plane direction with the line spacing not representative of the fracture density distribution. The azimuth angle of survey lines is with respect to the symmetry axis of the simulated fractured layer. The imaged CMP point is indicated by an $\star$. Receivers are shown in blue, and the sources are shown in red. The x_1- and x_2-axis are showing the scaled dimensions in meters. Only five azimuth lines from a total of nine are displayed. The maximum number of traces in each azimuth line is 291. A total of 2499 traces was acquired in the experiment.

are examined in the amplitude analysis.

In these physical modeling experiments, as the sources and receivers are located near the water surface, primary and ghost reflections are expected. The interference of primary and ghost reflections corrupt the amplitude information required for an amplitude analysis, and therefore should be avoided. Hence, the azimuth lines were acquired with the transducers' tip 2.5mm within the water, so that the primary and ghost events are separated. This decision is based on a preliminary experiment designed to examine the behavior of the ghosts. In this experiment, the source and receiver were kept at a fixed offset of 10mm, and seismograms were recorded at 0.2mm depth intervals as both transducers were raised from a depth of 10mm up to zero depth (at which the active tips of the transducers were nominally coplanar with the water surface). Figure 3.4 shows a suite of seismograms from this experiment. For each reflector, three events are collected, a primary, a ghost, and a constant traveltime event. The primary has a time moveout towards earlier times as tip depth increases. This is as expected since, as tip depth increases, the lengths of the raypaths from the tips to the reflecting interface decreases (Figure 3.5a). For the ghost, the arrival times increase as tip depth increases, which is also expected (Figure 3.5b), since the total raypaths for this ghost includes segments from the tips to the surface (lengths increase with tip depth) and segments from the surface to the reflecting interface (lengths are independent on tip depth). The third event has an almost constant traveltime, and has a traveltime as if the source and receiver were both located at the water surface, and therefore there is no apparent change in travel path length as tip depth changes. This constant traveltime event is generated by two single-sided ghost events at the source or receiver (Figure 3.5c). The existence of two single-sided ghosts makes the constant traveltime event appear strong. In appendix B, it is shown the single-sided ghost event has a constant traveltime as if the wave was generated at water contact with the source transducer, reflected from the CMP point between

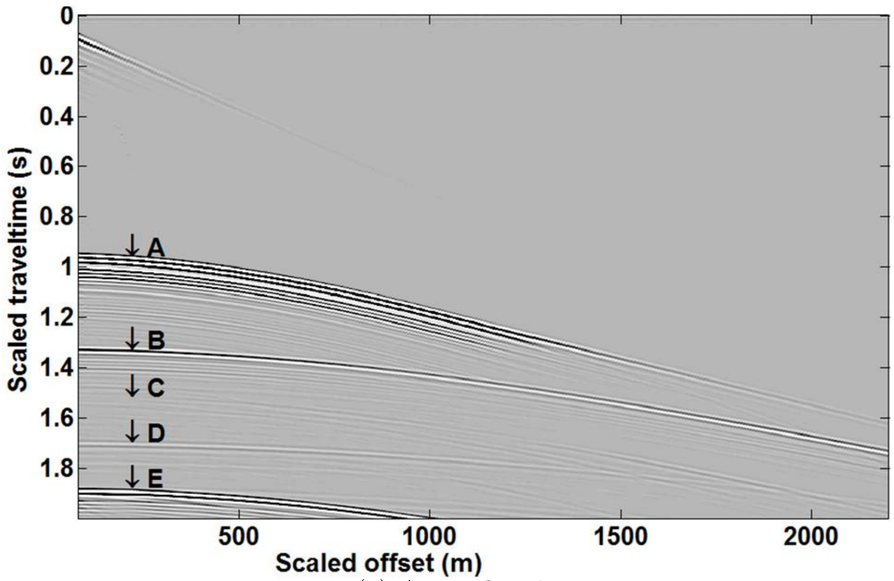

(a) Azimuth 90°

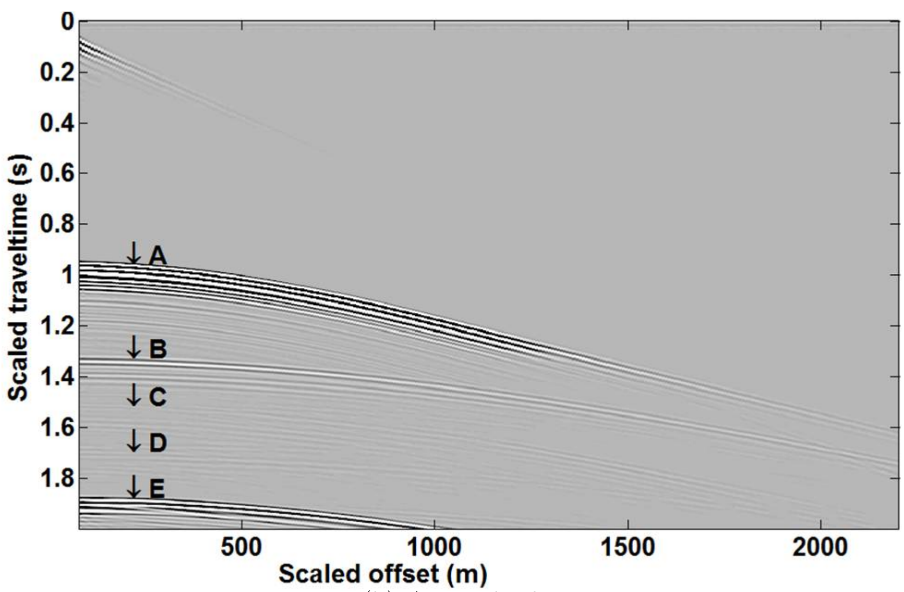

(b) Azimuth 0°

Figure 3.3: Sample CMP gather acquired over azimuth 90° and 0° data with transducers touching the water surface. A long gate (900ms) automatic gain control is applied. In the display, event "A" is the PP reflection from the top of the plexiglas layer, event "B" is the PP reflection from the top of the fractured layer (our target), event "C" is the PS reflection from the top of the fractured layer, event "D" is the PP reflection from the bottom of the fractured layer, and event "E" is a water bottom multiple. The PP reflection event from the bottom of the fractured layer (D) in 0° azimuth data, is hardly visible due to the higher amplitude decay along the fractures' symmetry axis.

the source and receiver, and recorded at water contact with the receiver transducer. An optimum transducers' tip depth within the water was chosen to be $2.5mm$, as it is the minimum transducer tip depth at which the primary and ghosts events can be recorded completely separately. A larger transducer tip depth is not desired as the ghost events from the upper reflector leak into the lower reflectors.

The 3D reflection data used for amplitude analysis were collected with the transducer's tip 2.5mm inside the water, Figure 3.6 shows the CMP gathers acquired along 0° and 90° azimuths. With the transducers inside the water, the reflections do not appear sharp and focused and the wavelet seems to be stretched out due to the presence of ghost events following the primary. However, for the purpose of using this dataset for a quantitative amplitude analysis, keeping the reflection amplitudes away from any interference with ghost events is of great importance.

3.3 Data processing

For each azimuth line, the P-wave reflections from the reflecting interfaces of interest were identified, and the arrival times and reflection amplitudes were picked using an automatic picker available in the CREWES MATLAB library[1]. The amplitudes of the first reflector, water-plexiglas, are picked from the primary event of the raw data. The second reflector, plexiglas-phenolic, was weak and hard to pick as its primary event suffers from severe wave interferences from top reflectors (first-arrival and water-plexiglas events). Figure 3.7-top is a blown up plot on the plexiglas-phenolic reflector for azimuths 0° and 90°, and clearly shows the wave interferences. To overcome the difficulty of picking the second reflector amplitudes, radial trace filtering (Henley, 2003) was applied to the data (appendix G). This estimate-and-subtract method attenuates the interference of the other events with the target event. Figure 3.7-middle shows the data after radial

[1]From "plotimage" software.

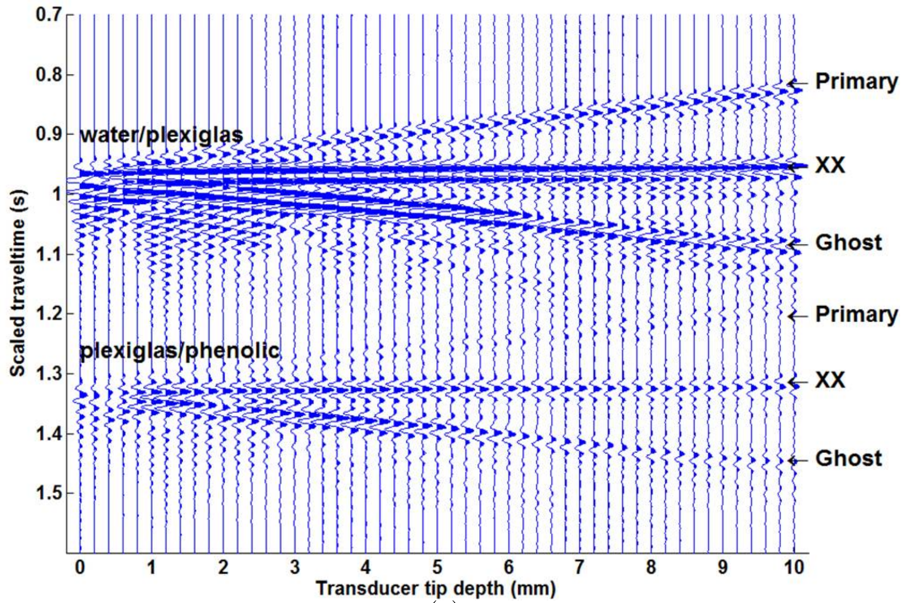

(a)

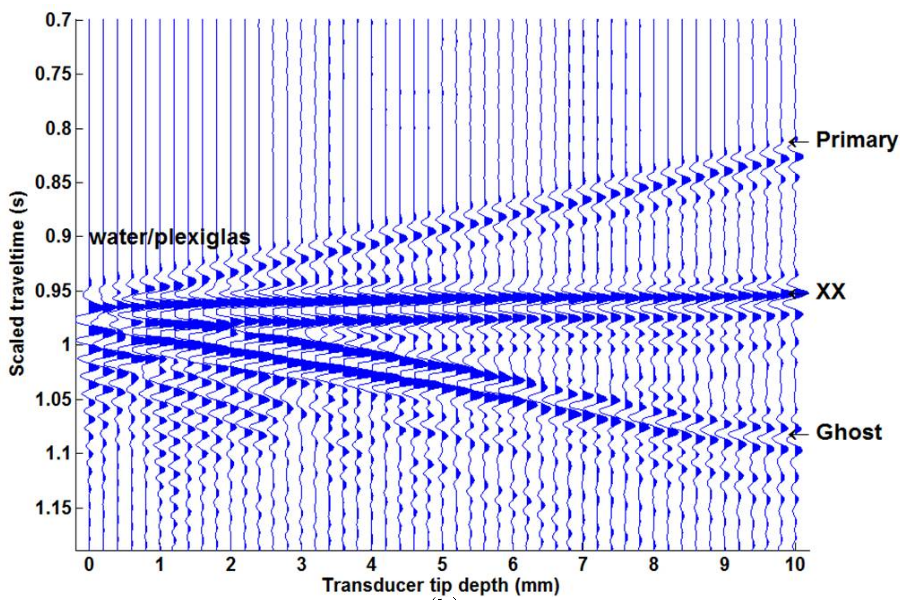

(b)

Figure 3.4: (a) Data acquired at a single source-receiver offset of 10mm with different transducer depths in water. b) Expanded time scale to show detail of the reflections from the water-plexiglas interface.

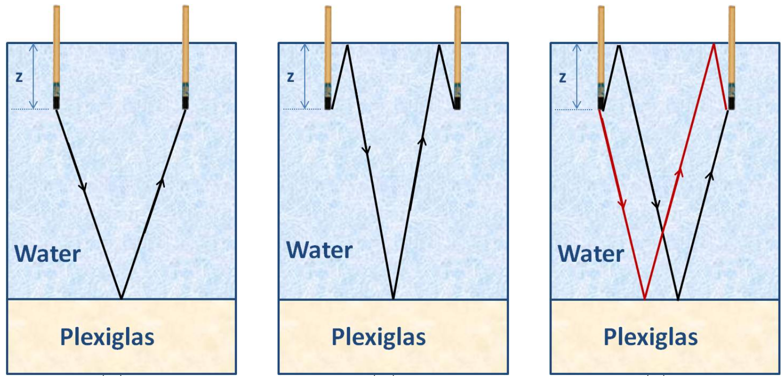

(a) (b) (c)

Figure 3.5: (a) Primary raypath. (b) Ghost raypath. (c) Asymmetric raypaths, two single-sided source and receiver ghosts, identified as "XX" in Figure 3.4.

trace filtering. The target event appears intact and clean after radial trace filtering. The applied filtering was successful in the attenuation of most of the interfering arrivals with the target event (Figure 3.7-bottom). To examine whether radial trace filtering does affect the amplitudes, the picked amplitudes from raw and filtered data are compared, for all azimuths. It is found that the amplitudes of the target are preserved after radial trace filtering. Figure 3.8 shows the target amplitudes picked from raw and filtered data for the 0° and 90° azimuths. The overall trend of the target amplitudes is preserved after filtering, an essential precondition to an amplitude analysis.

3.3.1 Amplitude corrections

Field recordings of seismic data, as well as physical model data, do not directly indicate target reflection coefficients due to numerous factors. The most important factors that disturb seismic amplitudes are geometrical spreading, transmission loss, anelastic attenuation, interference of primary and ghost reflections due to a free surface, interbed multiples, and source/receiver array response (e.g., Spratt et al., 1993). Such effects alter amplitudes and are independent of the model properties and should be compensated for, so that the reflection amplitudes represent the reflection coefficients of an interface.

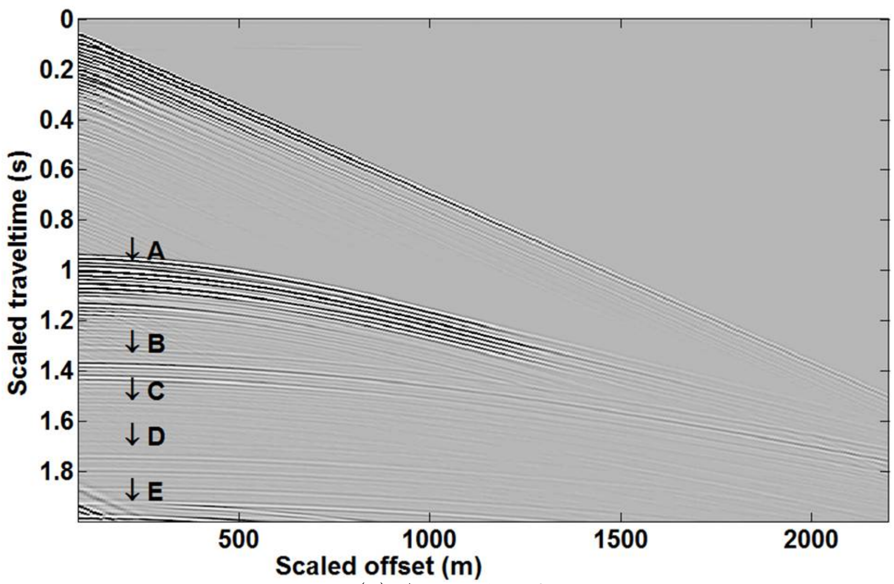

(a) Azimuth 90°

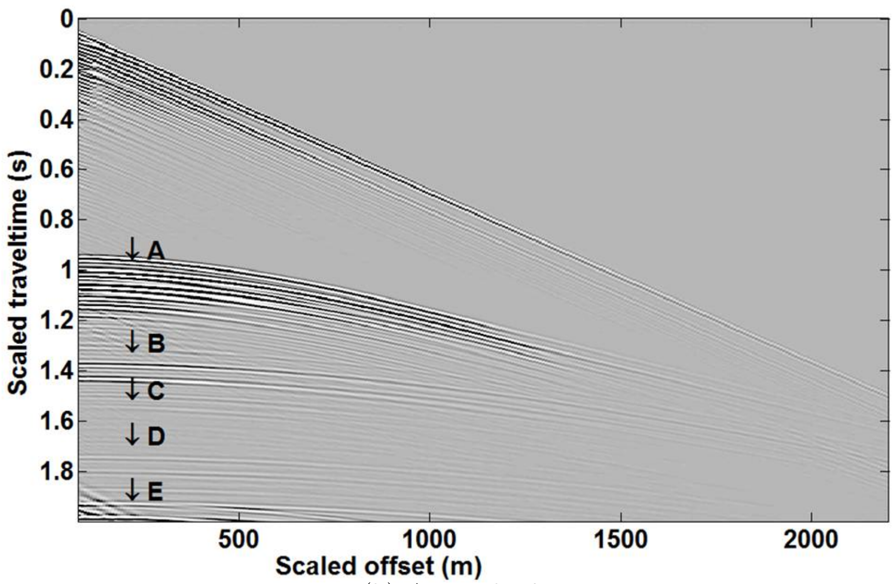

(b) Azimuth 0°

Figure 3.6: Sample CMP gather acquired over 90° and 0° azimuth data with transducers 2.5mm inside the water. A long gate (900ms) automatic gain control is applied. The events A, B, C, D, and E are as defined in Figure 3.3. The arrows point to the primary reflections. Note, primary events are weaker than their subsequent ghost events.

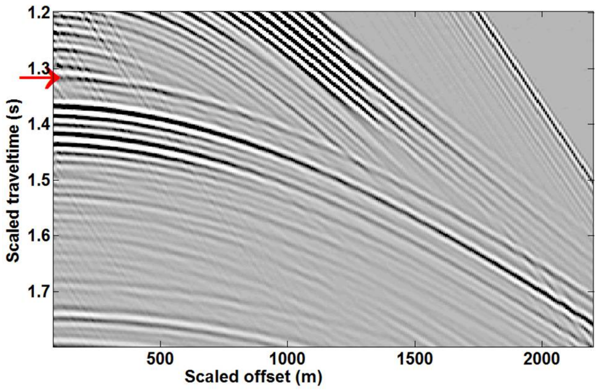

(a) Azimuth 90°, raw data

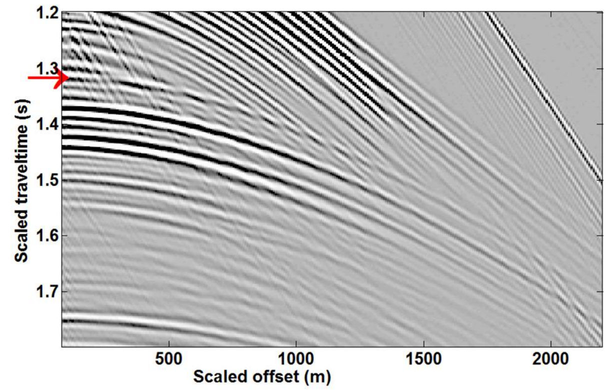

(b) Azimuth 0°, raw data

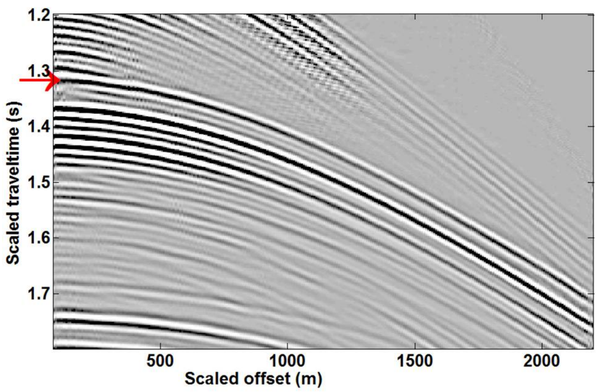

(c) Azimuth 90°, filtered data

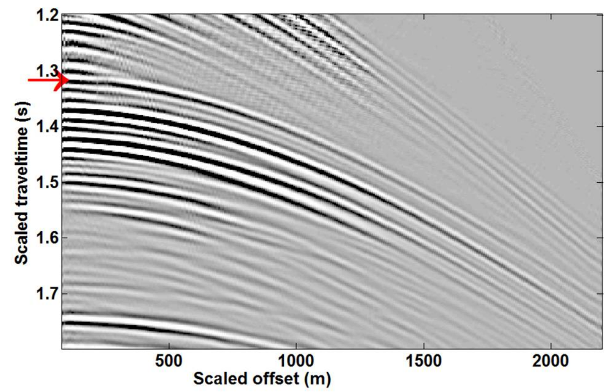

(d) Azimuth 0°, filtered data

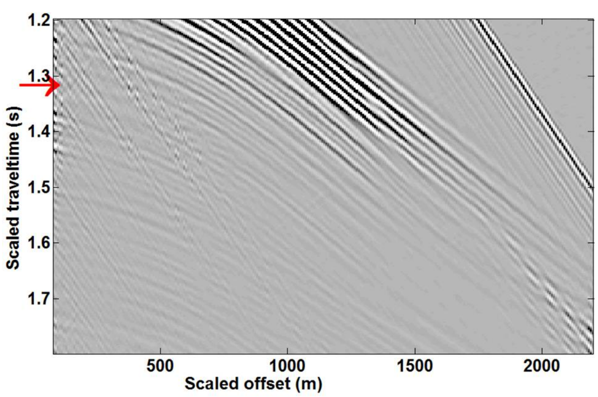

(e) Azimuth 90°, difference

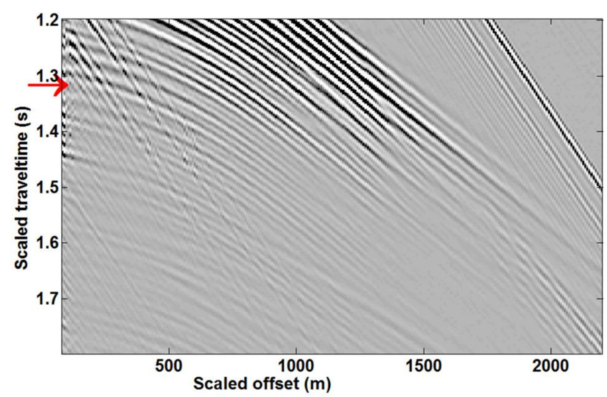

(f) Azimuth 0°, difference

Figure 3.7: Azimuths 0° and 90° data zoomed around the plexiglas-phenolic reflection, the target is pointed to by an arrow. The top plots show the raw data, followed by the filtered data, and the bottom row shows the difference of the raw data (top row) and the filtered data (middle row).

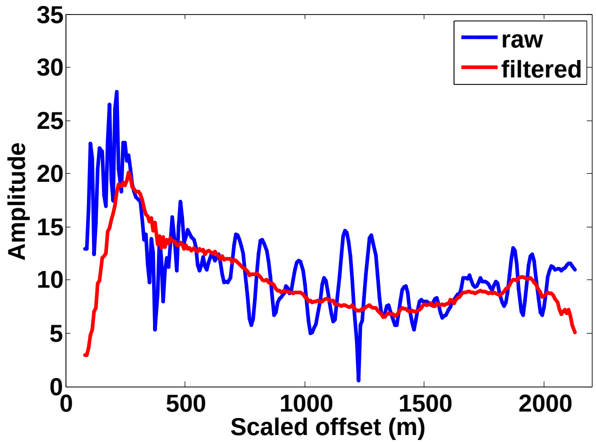

(a) Azimuth 90°

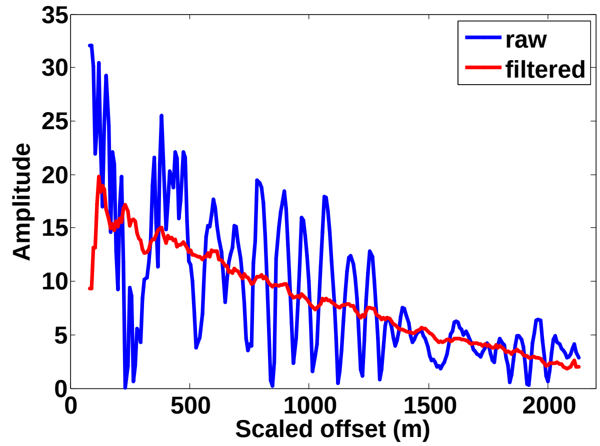

(b) Azimuth 0°

Figure 3.8: Picked amplitude from raw and filtered CMP data along azimuths of 90° and 0°.

Duren (1992) presented AVO corrections on marine data to reveal amplitude behavior with offset. In this thesis I follow Duren (1992) and apply a deterministic amplitude correction to the physical model reflection amplitudes. As previously explained, the acquisition design avoids overlapping primary and ghost events, and the interference of interbed multiples with our target event. Assuming homogeneity of the model layers and ignoring anelastic attenuation, the effects of geometrical spreading, emergence angle, transmission losses, and source/receiver array (which is called source/reciever directivity here) are the relevant factors for the physical model reflection amplitudes.

For a horizontally layered medium as shown in Figure 3.9, the recorded vertical-component reflection amplitude (along a CMP profile at azimuth ϕ) can be considered as

$$A(x, f) = \frac{SD(\theta_s, f)D(\theta_h, f)L(x)\cos\theta_h}{D_g(x)}R_T(\theta_T) \tag{3.1}$$

where f is the frequency, x is the source-receiver offset, θ_s is the source radiated ray direction, θ_h is the emergence angle at the receiver, θ_T is the incident angle at the target

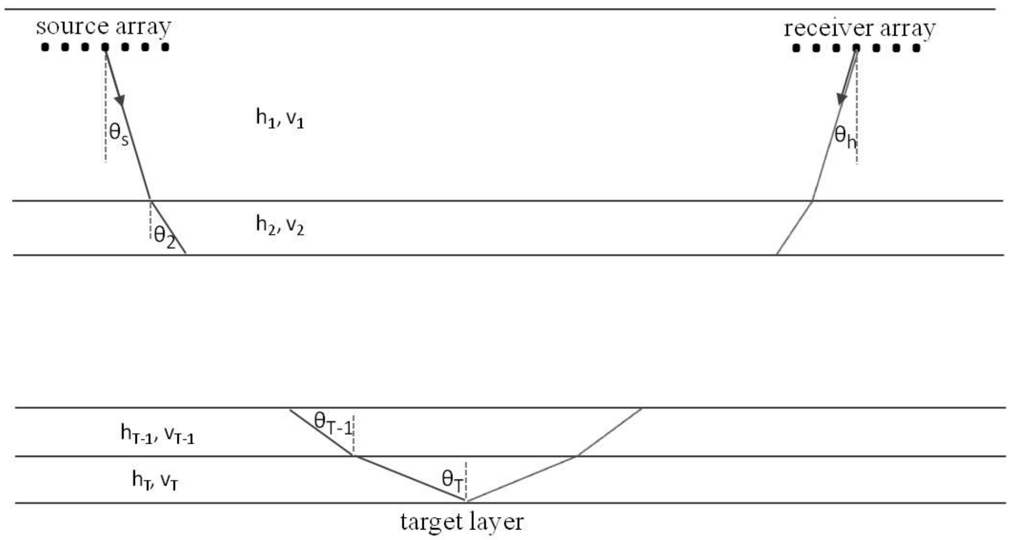

Figure 3.9: Raypath geometry for horizontally layered subsurfaces (Duren (1991)).

reflector, and

$$
\begin{aligned}
A(x, f) &= \text{vertical-component recorded reflection amplitude,} \\
S &= \text{overall scalar related to source strength,} \\
D(\theta_s, f) &= \text{source directivity along the } \theta_s \text{ direction,} \\
D(\theta_h, f) &= \text{receiver directivity along the } \theta_h \text{ direction,} \\
R_T(\theta_T) &= \text{target's reflection coefficient,} \\
D_g(x) &= \text{geometrical spreading,} \\
L(x) &= \text{transmission loss.}
\end{aligned}
$$

Each of the factors in equation 3.1 should be compensated for so that the physical model reflection amplitude, $A(x, f)$, after corrections, estimates the reflection coefficient, $R_T(\theta_T)$. Assuming a horizontally stratified subsurface and using ray theory, the subsurface factors in equation 3.1 can be estimated. For a given offset and target depth, the primary's raypath is being traced, employing Snell's law, using a PP ray-tracing function from the CREWES MatLab library[2], to determine the ray incident angle at the target reflector, the emergence angle at the receiver location, the geometrical spreading, and the transmission loss. Appendix F presents the corrections for these subsurface factors in greater detail. In the next section, the directivity correction for physical model transducers, $D(\theta, f)$, is presented.

3.3.2 Source/receiver directivity

Actual sources and receivers in the field are generally very small compared to seismic wavelengths, and are treated as point sources and receivers. The physical model transducers, with their larger dimensions, cannot be treated as point sources/receivers. They produce the seismic wavefield where amplitudes are directionally biased. An illustration of the produced pressure field is shown in Figure 3.10, showing that less energy propagates at high angles (i.e., far offsets). The directionality behavior of physical model transducers can be best described by a seismic array. It is well known that the radiated wavefield from a source array has a directivity pattern. (Parkes et al., 1984; Duren, 1988). Directivity is defined as the ratio of radiated energy density in a particular direction to the average radiated energy (Duren, 1988). A numerical model of the directivity of a circular source transducer is presented next.

Consider a source transducer. Assuming Huygens's principle, a transducer can be regarded as an array of point sources where each individual element radiates the same waveform simultaneously with the others. Take a coordinate system with the origin at the center of the source transducer, and the circular planar transducer in the $z = 0$ plane with the individual element location at $\vec{r_s} = (x_s, y_s, 0)$, and a point receiver in the (x, z) plane at $\vec{r} = (R\cos\theta, 0, R\sin\theta)$ (Figure 3.11). Consider a monochromatic acoustic wavefield radiated from individual points in the transducer and detected at the point

[2]traceray-pp.

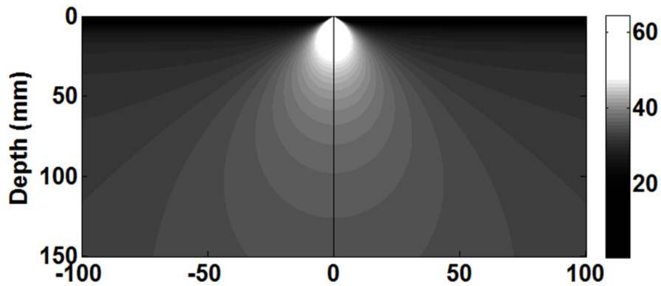

Figure 3.10: The calculated pressure field for a circular transducer of a diameter of 12mm as a function of depth and angle for a frequency of 200 kHz (after Buddensiek et al. (2009)).

receiver, described by the Helmholtz Green function

$$p_0 \frac{e^{ik|\vec{r}-\vec{r_s}|}}{|\vec{r}-\vec{r_s}|}. \tag{3.2}$$

Here p_0 is the initial pressure, $k = 2\pi/\lambda$ is the spatial wavenumber, and $\vec{r_s}$ is the location of the point source. The total far-field is the sum of individually radiated wavefields

$$P(\vec{r}, f) = p_0 \int_{-a}^{a} \int_{-\pi}^{\pi} \frac{e^{ik|\vec{r}-\vec{r_s}|}}{|\vec{r}-\vec{r_s}|} dr_s d\theta, \tag{3.3}$$

where $P(\vec{r}, f)$ is the pressure field, and a is the transducer radius. When $\vec{r}$ is much

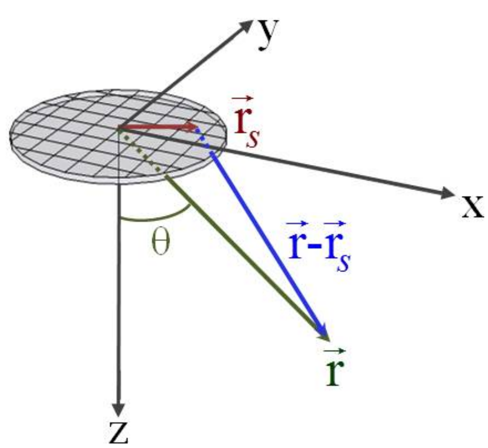

Figure 3.11: A circular source transducer in the $z = 0$ plane as a source array, with the point receiver at location $\vec{r}$.

greater than the transducer radius, equation 3.3 is described analytically (e.g., Schmerr, 1998; Kundu, 2003) as:

$$
\begin{aligned}
P(\vec{r}, f) &= p_0 \frac{e^{ikR}}{R} \frac{J_1(X)}{X}, \\
X &= \frac{\pi(2a)f}{v} \sin\theta,
\end{aligned}
\tag{3.4}
$$

where J_1 is the Bessel function of order 1 and v is the P-wave velocity. In this equation, the e^{ikR}/R term is the wavefield generated by a point source at the center of the transducer as detected at a point receiver at a distance R. The second term defines the directivity of the circular transducer assuming unit average energy. Hence, the directivity of the transducer is

$$
D(\theta, f) = \frac{J_1(X)}{X}. \tag{3.5}
$$

Figure 3.12 shows the directivity function for three transducer sizes. The transducers used in acquiring the physical model reflection data, with a diameter of 1.36mm have a directivity similar to Figure 3.12(a). The directivity equation for circular transducers is similar to the response of a linear array of length L given by

$$
\frac{\sin(\frac{\pi L f}{v} \sin\theta)}{\frac{\pi L f}{v} \sin\theta}. \tag{3.6}
$$

Equation 3.5 is used to compensate for the directivity effect of the employed source/reciever transducers. By reciprocity, the directional characteristic of a circular transducer is the same whether used as a source or a receiver.

3.4 AVO response of the water-plexiglas interface

The reflection amplitudes from the water-plexiglas interface were picked from the primary event on the raw data as previously mentioned. Figure 3.13 shows the offset and incident angle relation for the water-plexiglas reflector. The picked amplitudes were corrected for the effects included in equation 3.1. The relevant corrections are geometrical spreading,

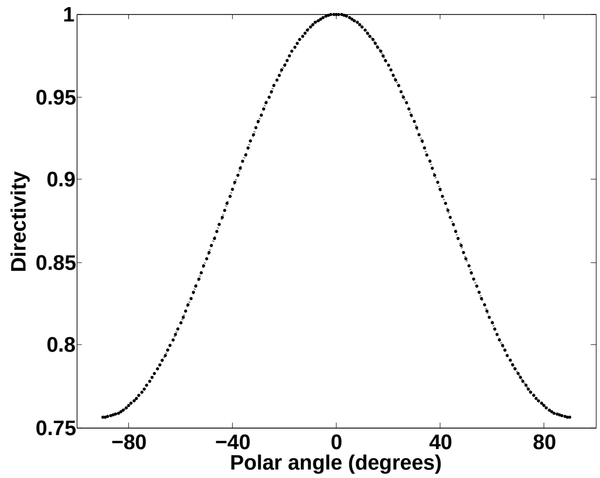

(a)

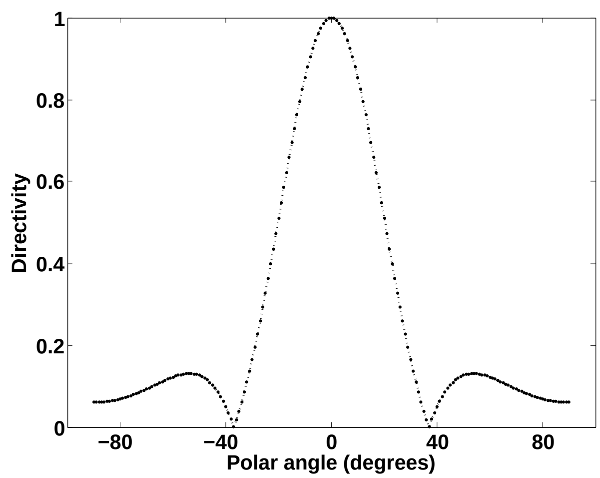

(b)

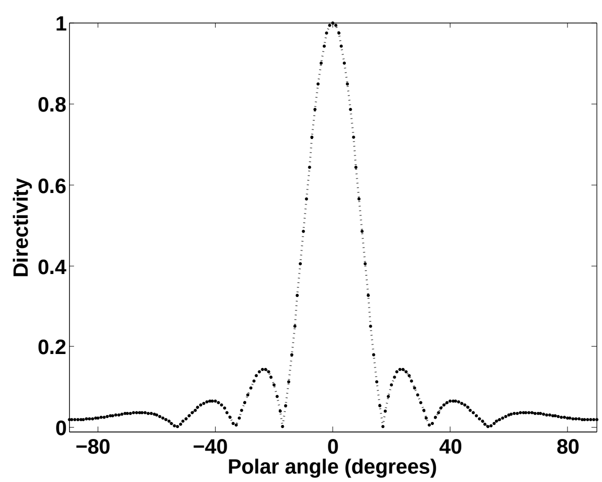

(c)

Figure 3.12: Directivity of a circular transducer with the diameter of (a) 1.3mm, (b) 6.0mm, (c) 12mm, for a frequency of 500kHz.

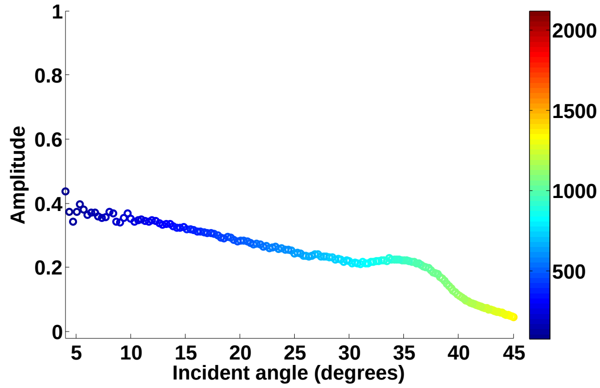

Figure 3.13: The picked amplitudes picked from the water-plexiglas reflector versus the incident angle. The colorbar displays the offset values.

emergence angle, and directivity. Figure 3.14 shows the raw amplitudes and cumulative results after each correction compared to the Zoeppritz solutions. The picked and corrected amplitudes are calibrated to the theoretical near-offset reflection coefficient, so that the amplitude variations between near and far offsets after each correction are revealed (see scaling in appendix F). The substantial improvement after each correction indicates the importance of each correction in preparing the amplitude data for an AVO analysis.

In the directivity correction (equation 3.5), deciding the effective diameter of the transducers, Buddensiek et al. (2009) method is followed. The value of the effective diameter is the value that gives the best match to the observed amplitudes. An effective diameter of 1.2mm was used for directivity correction. The nominal size of transducers from the manufacturer is 1.36mm.

The corrected amplitudes reflected from the water-plexiglas interface have been compared to the plane-wave and spherical-wave Zoeppritz solutions (Figure 3.14). The spherical-wave Zoeppritz equation, implemented as a JAVA applet by Ursenbach et al. (2006), is available from the CREWES website. The corrected water-plexiglas amplitudes agree very well with the amplitudes predicted by the Zoeppritz equations for mid-

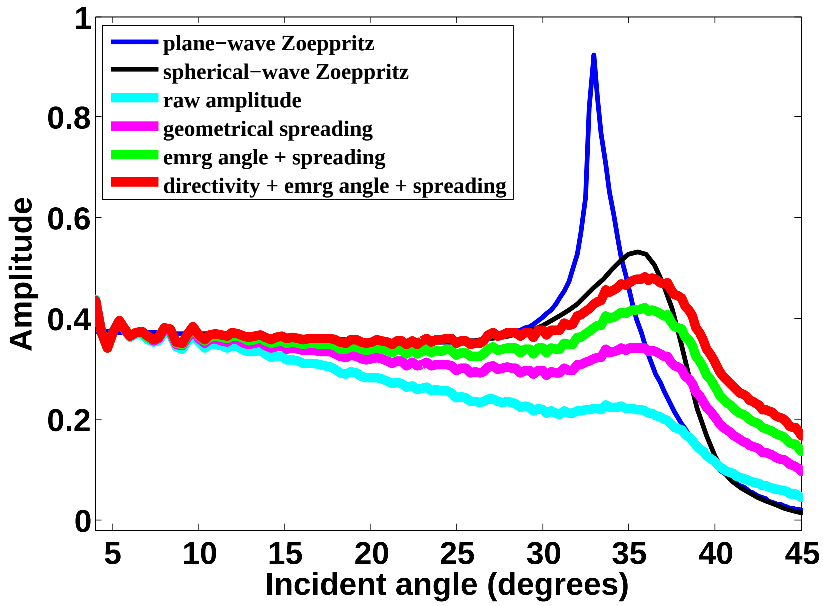

Figure 3.14: Reflection amplitudes from the water-plexiglas interface. The plane-wave Zoeppritz solution is shown in (blue), the spherical-wave Zoeppritz solution (black), raw amplitudes (light blue), and cumulative results after geometrical spreading correction (purple), after an emergence angle correction (green), and after a directivity correction (red).

dle range angles of incident, before the critically refracted arrivals are starting to appear (Figure 3.14). The corrected amplitudes deviate significantly from the theoretical amplitudes passed the critical angle (around 32°) with the corresponding offset around 1000m (see Figure 3.13 for the incident angle and offset relation). Passed the critical angle, amplitude picking was done on the strong head waves, rather than the weak post-critical reflection. Figure 3.15 shows a CMP gather with a short gate AGC applied to boost the weak post-critical reflection.

No azimuthal variations were observed for the water-plexiglas reflector, the interface of the two isotropic media. Figure 3.16 displays the corrected water-plexiglas amplitudes along the 0° and 90° azimuth lines.

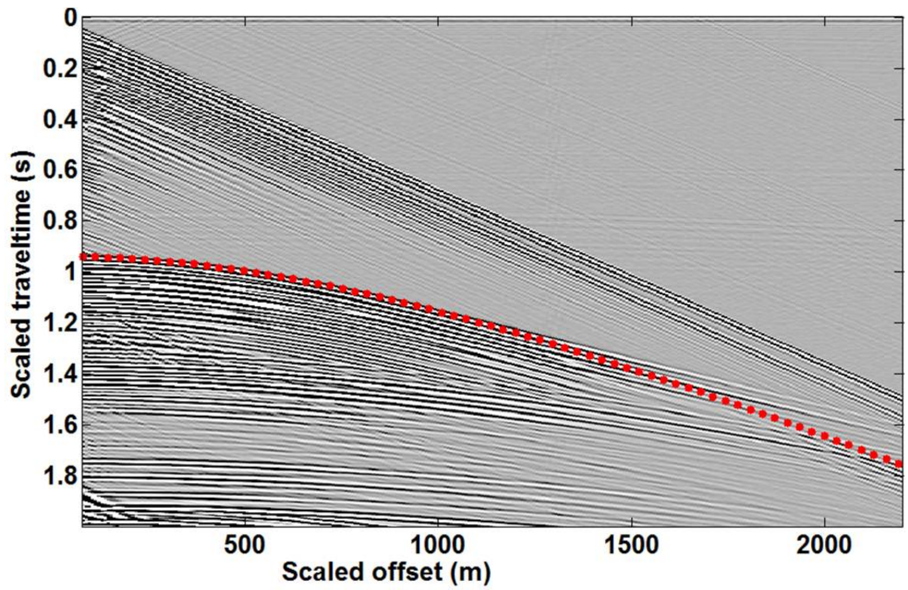

Figure 3.15: 0° azimuth data. The NMO curve of the water-plexiglas reflector is shown in red.

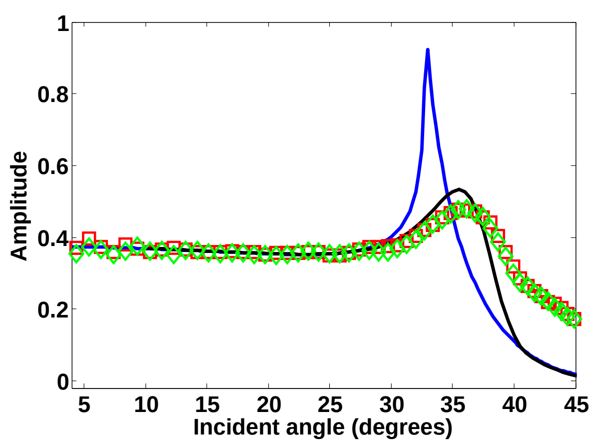

Figure 3.16: Water-plexiglas corrected amplitudes from the 0° azimuth (red squares) and 90° azimuth (green diamonds), to display that amplitudes are azimuthally invariant.

3.5 Azimuthal AVO of the plexiglas-phenolic interface

The reflection amplitudes from the plexiglas-phenolic interface, an isotropic-anisotropic interface, were picked from the primary event on the filtered data. Figure 3.17 shows the offset and incident angle relation for the plexiglas-phenolic reflector for the azimuths $0°$ and $90°$. Reflection amplitudes were then corrected for geometrical spreading, transmission loss, emergence angle, and directivity effects. The effective diameter of 1.2mm, derived from the top reflector, was consistently used in correcting amplitudes for all nine azimuths. The picked and corrected amplitudes, are calibrated to the theoretical near-offset reflection coefficient, similar to the case of water-plexiglas reflector. For the $90°$ azimuth, the direction of the isotropic plane of the fractured layer, the amplitudes are compared to the theoretical reflection coefficients from the Zoeppritz equations. The picked and corrected amplitudes, after each correction, are plotted in Figure 3.18a. Similar to the water-plexiglas reflector, each correction, except the directivity correction, provided a substantial improvement. For the plexiglas-phenolic reflector the directivity correction is minimal. At this reflector, being 1890m away from the transducers, the effect of the finite-size of the transducers is less pronounced. This is due to the smaller emergence angle for the amplitudes coming from the plexiglas-phenolic reflector. At the critical angle of the plexiglas-phenolic reflector (around $52°$ in azimuth $90°$), the emergence angle is approximately $25°$. In Figure 3.14, the small effect of the directivity correction for angles smaller than $25°$ can be seen.

Similar to the water-plexiglas reflector, the final corrected amplitudes follow the spherical-wave predicted amplitudes, with better agreement at incident angles closer to the critical angle, similar to that reported by Winterstein and Hanten (1985), Haase and Ursenbach (2007), and Alhussain et al. (2008). However, perfect agreement between the observed amplitudes and the spherical-wave predicted amplitudes is not observed either.

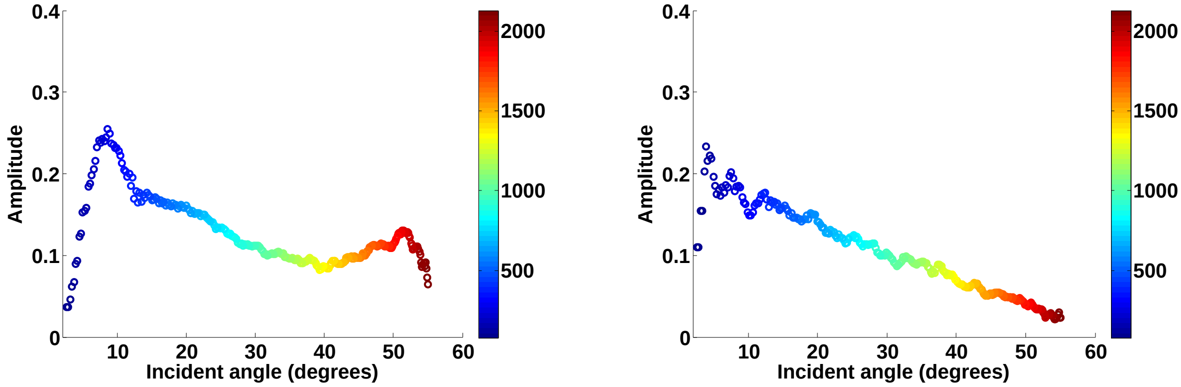

(a) Azimuth 90°

(b) Azimuth 0°

Figure 3.17: The reflection amplitudes from the plexiglas-phenolic reflector versus the incident angle. the colorbar displays the offset values.

This could be mostly due to the plane-wave nature of the applied corrections which are based on the assumption of relating the amplitudes to a single ray. However, the reflection of the spherical-waves involves reflections of not just the part corresponding to the specular ray but a bundle of rays within the ray beam around the central ray (Bleistein et al., 2001).

The corrected amplitudes of the plexiglas-phenolic reflector for the nine azimuths between 0° and 90° are shown in Figure 3.19a. The corrected amplitudes from only the 0°, 45°, and 90° azimuths are shown in Figure 3.19b. There is almost no azimuthal amplitude variation for the incident angles before 30°. The azimuthal variation starts to pick up after 30°. For the incident angles larger than 30°, a clear azimuthal amplitude variation is observed.

The amplitudes reflected from the top of the fractured layer follow the theoretically predicted reflectivity of Rüger's equation closely for incident angles up to the critical angle (around 52° at the 90° azimuth), Figure 3.20. See Chapter 4 for a definition of Rüger's equation for the PP reflection coefficient from a boundary of two HTI layers. Reflectivity amplitudes predicted by Rüger's equation are calculated using the elastic properties of plexiglas and the phenolic layer (Tables 3.1 and 2.6). Beyond about 50°,

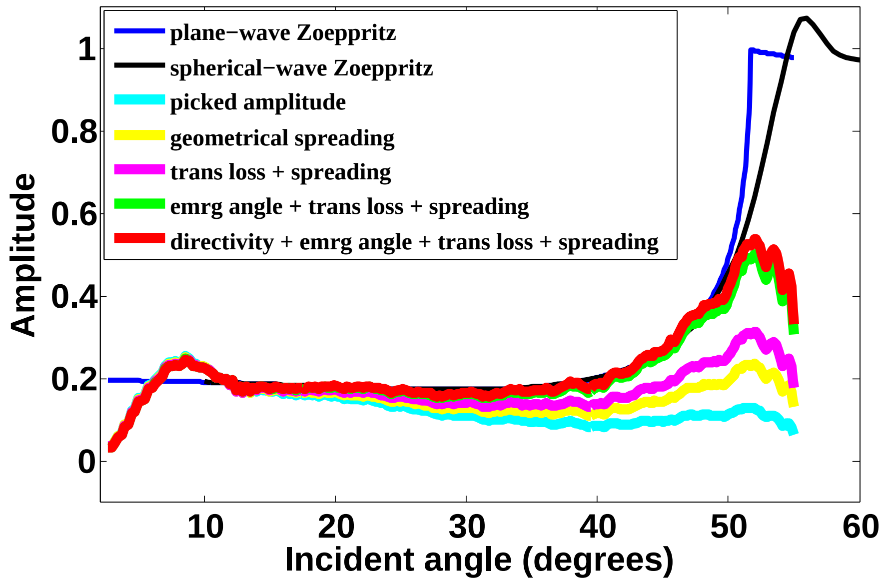

(a) Azimuth 90°

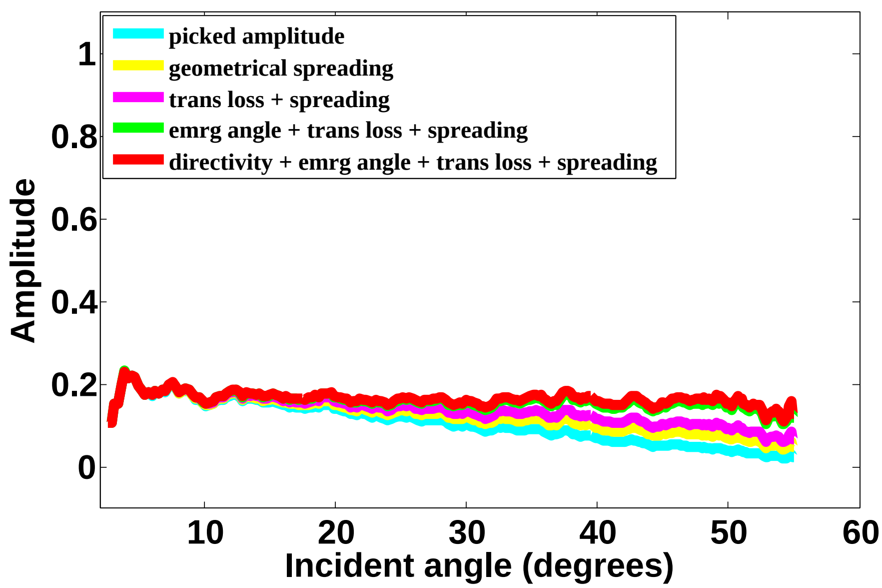

(b) Azimuth 0°

Figure 3.18: The reflection amplitudes of the plexiglas-phenolic interface.

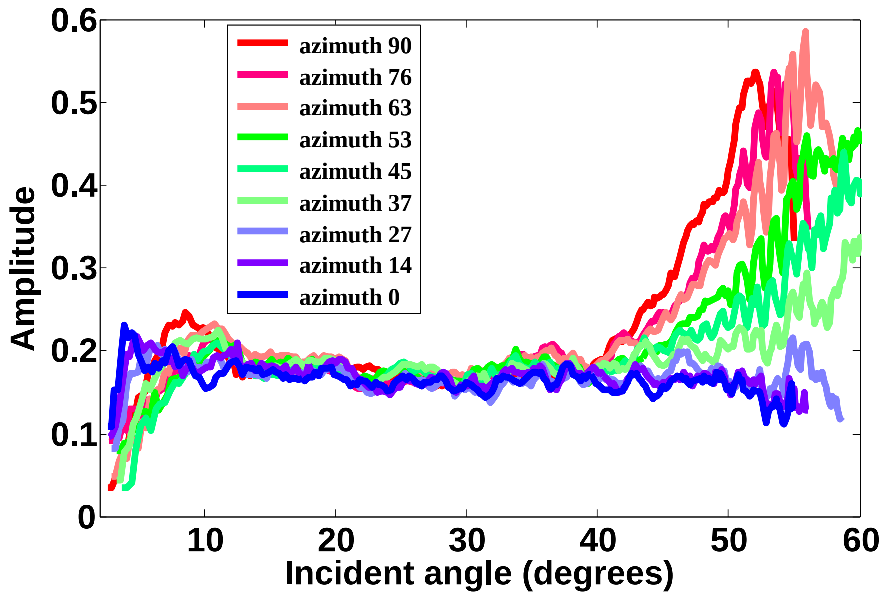

(a)

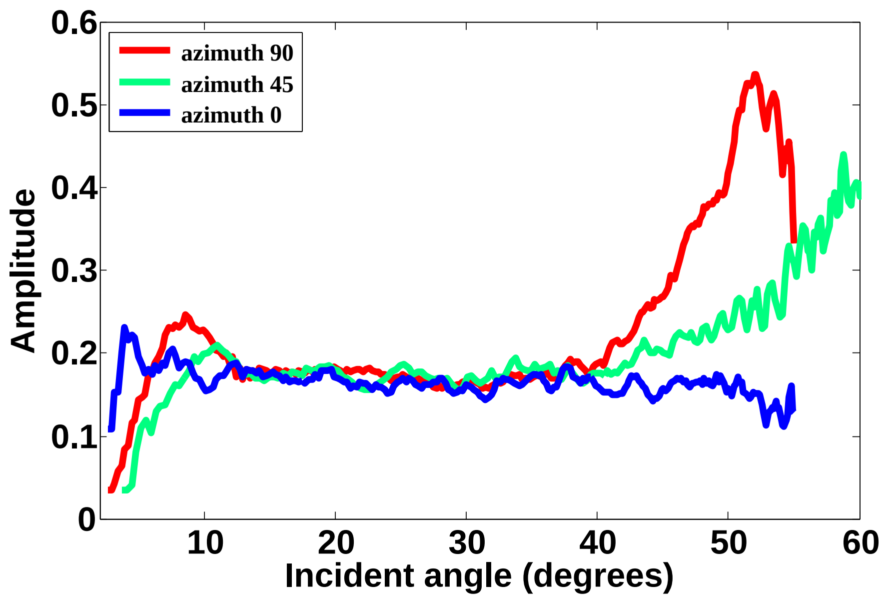

(b)

Figure 3.19: The corrected plexiglas-phenolic reflection amplitudes for (a) all nine azimuths, (b) only three azimuths.

the deviations of the experimental data from Rüger's prediction are due to the fact that Rüger's equation is valid only for plane waves. The corrected amplitudes reflected from the top of the fractured medium will be used as input to an AVAZ analysis to estimate Thomsen's anisotropic parameters of the fractured layer presented in Chapter 4.

3.5.1 The very near offset anomaly

Picking amplitudes of the plexiglas-phenolic reflector from the radial trace filtered data, there is an anomaly in the amplitude data at small incident angles, existing in nearly all azimuths (Figure 3.19). This anomaly is due to the inability of the radial trace filtering algorithm to attenuate a wave interference with the target event at very small incident angles. At very small incident angles, the interfering event has nearly the same dip as the target event (Figure 3.7c-d), any dip filter is unable to discriminate it from the target event, and consequently is unable to remove it, see appendix G. Whereas for the farther offsets, the larger move-out differences between the target event and the interfering events enable the radial trace filter to discriminate the unwanted linear event from the event of interest (Figure G.2a). Consequently, for large incident angles a clear attenuation was achieved, and amplitude data followed the expected trend nicely.

3.6 Discussions

The presented acquisition and processing of the 3D physical model data acquired, over a simple horizontal layering model, might seem rather straight forward. The most important challenges of the acquisition and processing of the physical model seismic data are discussed in Appendix I; the effect of not having welded contacts for the solid interfaces, and the directivity effect of the transducers, are discussed. Now knowing how to compensate for the directivity effect of the transducers, and how to deal with the acquisition of data from solid-solid interfaces, the explained acquisition and processing procedures

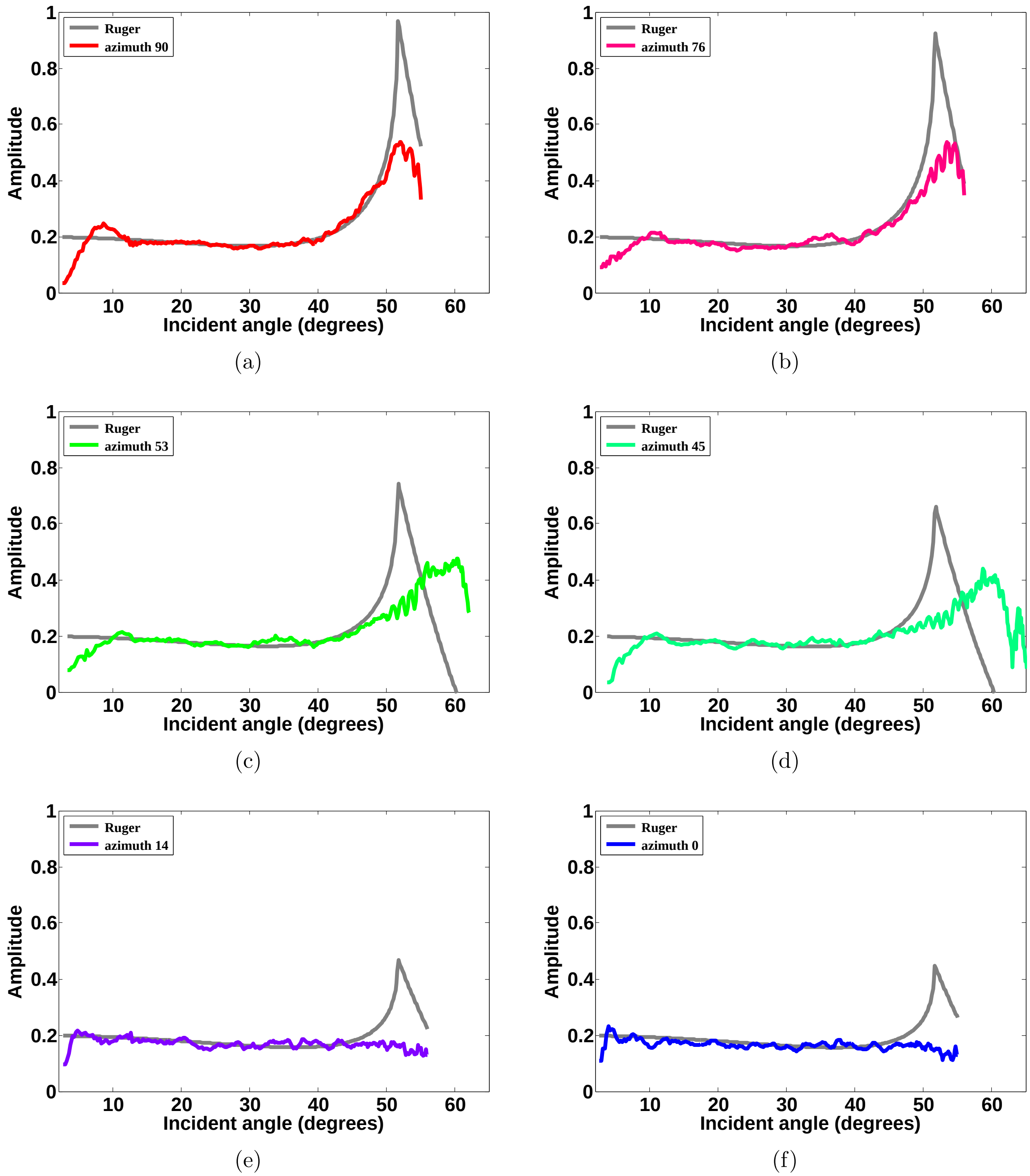

Figure 3.20: Plexiglas-phenolic corrected amplitudes compared to theoretical reflection coefficients predicted by Rüger's equation, from (a) azimuth 90°, (b) azimuth 76° (c) azimuth 53°, (d) azimuth 45°, (e) azimuth 14°, and (f) azimuth 0°.

can be applied to obtain physical seismic data over more complicated models.

The presented physical model reflection data were processed with no deconvolution techniques applied. The model has large-contrast, isolated reflectors which are resolvable without applying deconvolution. Once data were scaled in a manner suitable for AVO, there was no need to apply a deconvolution. The overall scalar that calibrated the amplitudes to the near-vertical reflection coefficient predicted by the Zoeppritz equations, can also be considered as removing the source signature for a single reflector. Most deconvolution techniques applied to the previous physical model data (Appendix I) increased noise level by boosting noise dominated high frequencies. A careful deconvolution requires measuring the transducer's emitted wavelet and designing a deconvolution operator, which would probably have to be varied with direction (angle). A proper deconvolution should improve the data quality, especially the ghost reverberations at near offsets, but was beyond the scope of this study.

A piezoelectric transducer produces a wavelet with a restricted bandwidth around its resonance frequency (Buddensiek et al., 2009). Figure 3.6 shows the amplitude spectrum of one of the physical model seismic traces used in this Chapter with the transducers' tips just slightly inside the water. It displays the restricted bandwidth and the strong amplitude at the scaled resonance frequency of 50Hz, while the notches in the amplitude spectrum are caused by ghosts events. In the case of using physical model data in a frequency sensitive inversion, in particular when the low-frequency content is important, such restricted band width should be considered. Nevertheless, the restricted bandwidth does not affect our amplitude analysis, as the interest of this work is the frequency band width of $0 - 50$Hz. Also, this restricted frequency band width, and the missing low frequency content, were taken care of by applying an overall scalar which calibrated the amplitudes to near-vertical reflection coefficient values.

Another characteristic of a piezoelectric transducer is the change of the radiated waveform with offset (Buddensiek et al., 2009), which is due to the large size of the transducer, as previously discussed in Chapter 2. The change in wavelet shape from near to far offsets is quite pronounced for the transducers with a size of 14mm Figure 2.3a. Nevertheless, for the amplitude analysis presented in this chapter, this effect can also be neglected as the size of the transducers (1.36mm) is smaller than the emitted wavelength (the acoustic wavelength is 2.8mm). Additionally, reflection data do not show a noticeable change in the wavelet shape between near and far offset traces.

Enabling the amplitude picking for the target event, radial trace filtering was applied to the reflection data. Reflection amplitudes appears to be unaltered on the filtered data, preserving the overall trend they have in the unfiltered data. Radial filtering was preferred over other coherent noise attenuation techniques, such as the regularly used filtering in the (f, k) transform domain, as the (f, k) technique, true to its reputation, greatly smears amplitudes.

Summary

The suitability of physical model seismic data for a quantitative amplitude analysis is being investigated. The reflection amplitudes from one isotropic-isotropic and one isotropic-anisotropic interface are subjected to corrections to make them represent reflection coefficients, and therefore can be used in an AVO analysis. The azimuthal AVO was clearly observed from the amplitudes reflected from the top of a simulated fractured layer, and agreed with theoretical amplitudes.

Real wave propagation occurs in physical modeling, so that the physical model seismic data can be treated as field data. While the traveltimes in physical modeling are reliable, the large, highly-directional transducers distort the seismic amplitudes, and their effect should be compensated for before any amplitude analysis. The directional amplitude responses of the transducers has been mitigated using an array-type (directivity) correction.

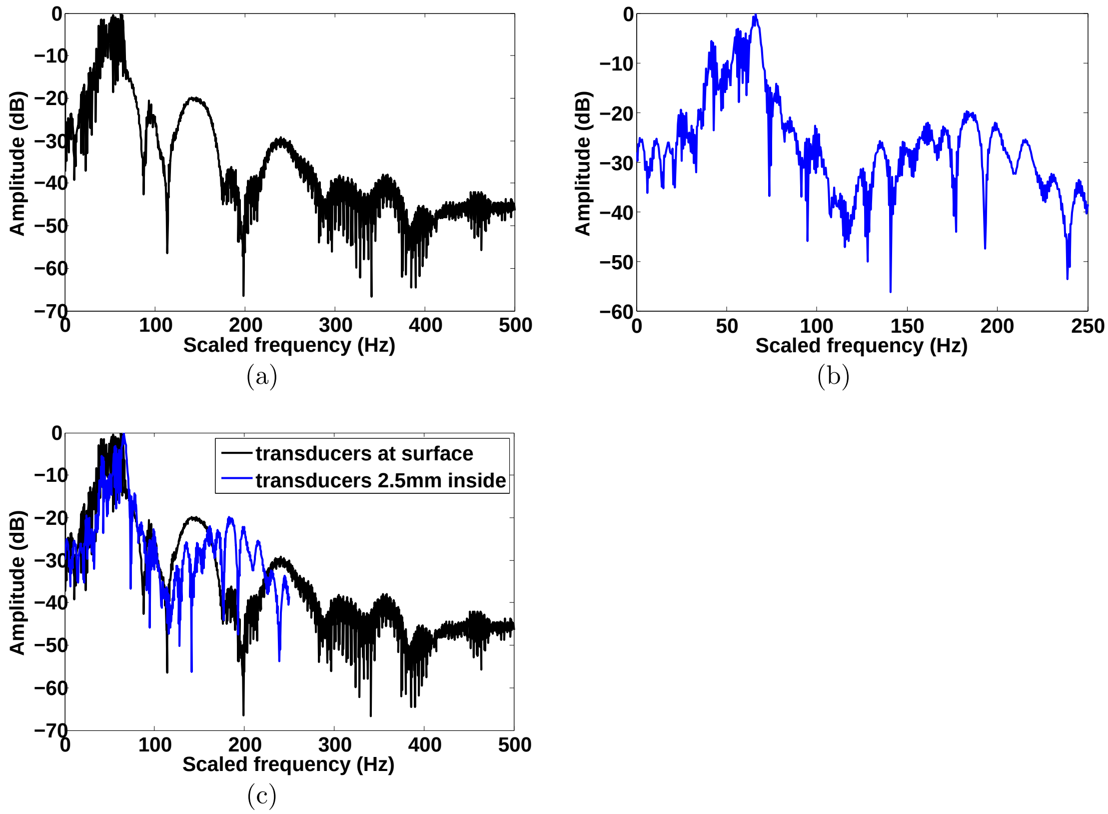

Figure 3.21: Amplitude spectrum of two of the physical model traces. (a) Transducers' tip touching the water surface, the data has time sample interval of 1ms. (b) The transducers' tip was 2.5mm inside the water, the time sample interval was 2ms. (c) Comparing the two traces.

Chapter 4

AVAZ inversion for fracture orientation and intensity

The pre-stack amplitude inversions of P-wave data for fracture orientation and intensity are presented in this chapter. The method was tested on multi-azimuth multi-offset physical model reflection data. The acquisition and processing of the data acquired over the simulated fractured medium were explained in Chapter 3. This chapter follows the method used by Jenner (2002) for amplitude inversion to extract the fracture orientation. Testing this method on the reflection amplitudes from the top of the simulated fractured layer, it is demonstrated that the orientation estimate is quite accurate. With the fracture orientation known, the linear PP reflection coefficient approximation given by Rüger (1997) was modified to invert for anisotropy parameters ($\epsilon^{(V)}, \delta^{(V)}, \gamma$), in addition to the isotropic terms ($\Delta\alpha/\alpha, \Delta\beta/\beta, \Delta\rho/\rho$). Wide-angle data are required for an accurate AVAZ inversion applied to the reflection amplitudes from the top of the simulated fractured layer, since the material shows only slight azimuthal amplitude variations for angles less than 37°. The results for all three anisotropy parameters from AVAZ inversion compare very favorably to those obtained previously by a different technique (traveltime inversion in Chapter 2). This result makes it possible to compute the shear-wave splitting parameter, γ, related directly to fracture intensity, from a quantitative analysis of only the PP reflected data, independent of the S-wave measurements required to determine the shear-wave splitting parameter more conventionally.

4.1 Background

For an isolated interface, the Zoeppritz equations Aki and Richards (1980) predict that the reflected amplitude changes as a function of angle of incidence. This is the basis of AVO (Amplitude Variations with Offset) or more properly AVA (Amplitude Variations with Angle). The Zoeppritz equations are derived for the idealized situation of two half-spaces in welded contact. In Aki and Richards (1980) it is assumed that these half-spaces are elastic and, in particular, isotropic. Daley and Hron (1977), Thomson (1988), Rüger (1997), and Tsvankin (2001) derived the AVO relationships for transverse isotropy anisotropy and beyond. For isotropic media, AVO inversion is a well established seismic exploration methodology to predict the earth's elastic parameters and thus rock and fluid properties. Among the many researcher who contributed to this topic, I like to mention Smith and Gidlow (1987); Lortzer and Berkhout (1993); Jin et al. (2000); Margrave et al. (2001); Downton (2005).

In a fracture-detection study, the ultimate goal of using an AVO inversion is to obtain information about the direction of fracture orientation and the magnitude of fracture intensity from 3D seismic data. Open natural fractures may hold fluid and can provide pathways for hydrocarbon flow. Detailed information about fracture intensity and orientation can help optimizing the drilling at sweet spots (Zheng, 2006). As previously mentioned in Chapter 1, depending on the stress regime that causes fracturing, the fracture orientation (however random) has a dominant direction confirmed by geological field measurements (Nelson, 1985).

It is assumed that a medium with a single set of natural vertical fractures can be described as an HTI medium, meaning that the direction of the dominant fracture face is in the direction of the isotropic plane of the HTI model. The azimuthal dependence of P- and S-wave stacking velocities and reflection amplitudes has been used to extract information related to the fracture intensity and orientation. Shear-wave splitting due to fractures has been historically used to detect fracture orientation (from the direction of the fast S-wave), while the shear-wave splitting parameter, γ, has been determined from an analysis of time delays of split shear waves (Crampin, 1981). Using P-wave NMO velocity variation with azimuth (VVAZ), fracture orientation is considered to be in the direction of the fast P-wave. Some indicator of fracture intensity results from estimating the Thomsen δ parameter (e.g., Tsvankin, 2001; Grechka and Tsvankin, 1998). Zheng and Wang (2005) used a target-oriented VVAZ approach, in which the differential residual NMO travel times between the top and the base of a fractured layer is used to invert for fracture orientation and the δ parameter. Quantitative amplitude analysis is also used for fracture detection, as in amplitude variation with angle and azimuth (AVAZ) method (Gray et al., 2002; Hunt et al., 2010). Jenner (2002) used the small-incident-angle approximation of the Rüger (1997) equation, which is a plane-wave approximation of the PP reflection coefficient for a boundary between two HTI layers, to directly invert for fracture orientation and the anisotropic gradient (a combination of δ and γ parameters) from azimuthal amplitude data.

4.2 Rüger's equation

Rüger's equation relates the AVO response to the anisotropy parameters, and provides physical insight into the reflection amplitudes. It is a plane-wave approximation for the PP reflection coefficient at a boundary between two HTI media with the same symmetry axis direction, Rüger (1997). Rüger's equation for HTI media with the symmetry axis along the azimuth φ_0 is

$$
\begin{aligned}
R_{PP}^{HTI}(\theta,\varphi) \cong & \frac{1}{2}\frac{\Delta Z}{\bar{Z}} \\
& + \frac{1}{2}\left\{\frac{\Delta\alpha}{\bar{\alpha}} - \left(\frac{2\bar{\beta}}{\bar{\alpha}}\right)^2\frac{\Delta G}{\bar{G}} + \left[\Delta\delta^{(V)} + 2\left(\frac{2\bar{\beta}}{\bar{\alpha}}\right)^2\Delta\gamma\right]\cos^2(\varphi-\varphi_0)\right\}\sin^2\theta \\
& + \frac{1}{2}\left\{\frac{\Delta\alpha}{\bar{\alpha}} + \Delta\epsilon^{(V)}\cos^4(\varphi-\varphi_0) + \Delta\delta^{(V)}\sin^2(\varphi-\varphi_0)\cos^2(\varphi-\varphi_0)\right\}\sin^2\theta\tan^2\theta.
\end{aligned} \tag{4.1}
$$

where θ is the incident angle (with respect to the vertical direction), φ is the source-receiver azimuth, α is the vertical P-wave velocity (fast P velocity), $Z = \rho\alpha$ is the P-wave impedance, β is the vertical S-wave velocity ($S^{\parallel}$-wave, fast S velocity), $G = \rho\beta^2$ is the shear modulus, and Δ denotes the difference in the elastic properties across the boundary. The average values of elastic properties of the two layers is denoted by the terms with overscores. $(\epsilon^{(V)}, \delta^{(V)}, \gamma)$ are the Thomsen-style anisotropy parameters for HTI media, as defined by Rüger (1997) (Table 2.5). As previously mentioned in Chapter 2, $\epsilon^{(V)}$ describes the difference between vertical and horizontal P-wave velocities, γ describes the difference between fast and slow S-wave velocities, and $\delta^{(V)}$ describes the departure from isotropy for near vertical propagation.

Reformulating Rüger's equation as a function of P- and S-wave velocities using

$$
\begin{aligned}
\frac{\Delta Z}{\bar{Z}} &= \frac{\Delta\alpha}{\bar{\alpha}} + \frac{\Delta\rho}{\bar{\rho}}, \\
\frac{\Delta G}{\bar{G}} &= 2\frac{\Delta\beta}{\bar{\beta}} + \frac{\Delta\rho}{\bar{\rho}},
\end{aligned} \tag{4.2}
$$

the results is the following which has a form analogous to equation 4.1,

$$\begin{aligned}
R_{PP}^{HTI}(\theta,\varphi) \cong {} & \left(\frac{1}{2\cos^2\theta}\right)\frac{\Delta\alpha}{\bar{\alpha}} - \left(\frac{4\beta^2}{\alpha^2}\sin^2\theta\right)\frac{\Delta\beta}{\bar{\beta}} \\
& + \left(\frac{1}{2} - \frac{2\beta^2}{\alpha^2}\sin^2\theta\right)\frac{\Delta\rho}{\bar{\rho}} \\
& + \left(\frac{1}{2}\cos^4(\varphi-\varphi_0)\sin^2\theta\tan^2\theta\right)\Delta\epsilon^{(V)} \\
& + \left(\frac{1}{2}\cos^2(\varphi-\varphi_0)\sin^2\theta + \frac{1}{2}\cos^2(\varphi-\varphi_0)\sin^2(\varphi-\varphi_0)\sin^2\theta\tan^2\theta\right)\Delta\delta^{(V)} \\
& + \left(\frac{4\beta^2}{\alpha^2}\cos^2(\varphi-\varphi_0)\sin^2\theta\right)\Delta\gamma.
\end{aligned} \tag{4.3}$$

The first three terms are Aki and Richards (1980) approximation for the PP reflection coefficient at a boundary between two isotropic media. The second three azimuthally dependent terms indicate the influence of each of the anisotropy parameters on the PP reflection coefficient approximation. In this thesis, the AVAZ inversion for fracture intensity is based on equation 4.3.

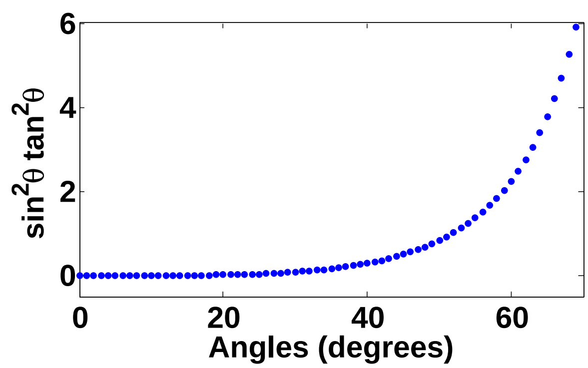

Figure 4.1: Function $\sin^2\theta\tan^2\theta$ plotted versus the angle in degrees.

4.3 Jenner's method

Considering only small incident angle data (e.g., less than 40°), for which the value of the $\sin^2\theta\tan^2\theta$ term is very small and can be neglected (Figure 4.1), equation 4.1 can then be written as:

$$R_{PP}^{HTI}(\theta,\varphi) \cong I + \big(G_1 + G_2\cos^2(\varphi-\varphi_0)\big)\sin^2\theta, \tag{4.4}$$

where

$$I = \frac{1}{2}\frac{\Delta Z}{\bar{Z}}, \tag{4.5}$$

$$G_1 = \frac{1}{2}\left(\frac{\Delta\alpha}{\bar{\alpha}} - \left(\frac{2\bar{\beta}}{\bar{\alpha}}\right)^2\frac{\Delta G}{\bar{G}}\right), \tag{4.6}$$

$$G_2 = \frac{1}{2}\left(\Delta\delta^{(V)} + 2\left(\frac{2\bar{\beta}}{\bar{\alpha}}\right)^2\Delta\gamma\right). \tag{4.7}$$

Equation 4.4 describes the behavior of R_{PP}^{HTI} at small incident angles as a function of the AVO intercept (I) and gradient [1]. The gradient term

$$Q = G_1 + G_2\cos^2(\varphi-\varphi_0), \tag{4.8}$$

is composed of the azimuthally invariant term G_1, and an anisotropic term G_2, and is non-linear in the three unknowns (G_1, G_2, φ_0). The goal is to apply a linear inversion of the PP amplitude data for these three unknowns. The following describes how to bypass this non-linearity and apply a linear inversion.

Using the identity $\sin(\varphi-\varphi_0)^2 + \cos(\varphi-\varphi_0)^2 = 1$, the gradient term, equation 4.8 becomes

$$Q = (G_1+G_2)\cos^2(\varphi-\varphi_0) + G_1\sin^2(\varphi-\varphi_0). \tag{4.9}$$

For any particular incident angle, if the AVO gradient does not change sign azimuthally, the gradient versus azimuth vector delineates a curve that closely resembles an ellipse (Rüger, 1997) with the semi-axes aligned with the symmetry plane directions of the fracture system (Figure 4.2). Taking (y_1, y_2) to be a coordinate system aligned with the

[1] Conventinally, the coefficient of the $\sin^2\theta$ term is called the AVO gradient.

fracture system, every point of the gradient satisfies

$$\begin{aligned} y_1 &= r\cos(\varphi - \varphi_0), \\ y_2 &= r\sin(\varphi - \varphi_0), \end{aligned} \tag{4.10}$$

where r is the vector magnitude. Then, the gradient term can be written as:

$$Q = \frac{1}{r}\left((G_1 + G_2)y_1^2 + G_1 y_2^2\right). \tag{4.11}$$

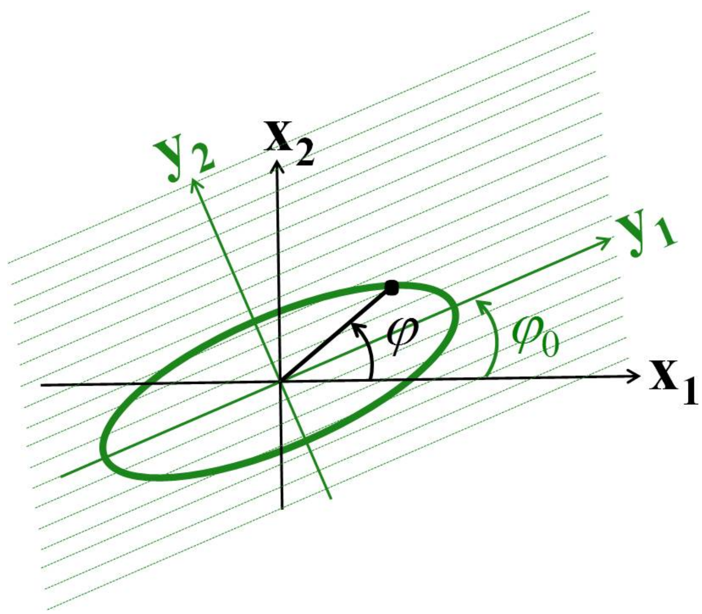

Figure 4.2: Reference coordinate system. (x_1, x_2) is the acquisition coordinate system, and (y_1, y_2) is the coordinate system aligned with the fracture system. φ is the source-receiver azimuth, and φ_0 is the fracture orientation azimuth.

By expanding the trigonometric terms of equation 4.9, the gradient term can be written as

$$Q = W_{11}\cos^2\varphi + 2W_{12}\cos\varphi\sin\varphi + W_{22}\sin^2\varphi, \tag{4.12}$$

where the W_{ij} terms are functions of (G_1, G_2, φ_0). Using this form hides the non-linearity with respect to the fracture orientation in the W_{ij} coefficients. The acquisition coordinate system, (x_1, x_2), can be thought of as a φ_0 rotated version of the (y_1, y_2) coordinate system (Figure 4.2). In the acquisition coordinate system, every point of the gradient follows

$$\begin{aligned} x_1 &= r\cos\varphi, \\ x_2 &= r\sin\varphi. \end{aligned} \tag{4.13}$$

If one writes the gradient ellipse in equation 4.12 in the acquisition coordinate system, the ellipse equation inherits a nonlinear term $x_1 x_2$, of the form

$$Q = \frac{1}{r}\left(W_{11}x_1^2 + 2W_{12}x_1x_2 + W_{22}x_2^2\right). \tag{4.14}$$

Equation 4.14 is a quadratic form, and can be written in matrix form,

$$\frac{1}{r}\begin{bmatrix} x_1 & x_2 \end{bmatrix}\begin{bmatrix} W_{11} & W_{12} \\ W_{12} & W_{22} \end{bmatrix}\begin{bmatrix} x_1 \\ x_2 \end{bmatrix} = \frac{1}{r}\left(X^T \mathbf{W} X\right). \tag{4.15}$$

The matrix $\mathbf{W}$ is symmetric, and therefore orthogonality diagonalizable (e.g., Lax, 1997). The eigenvalues of the matrix W are

$$\lambda_{1,2} = 0.5\left[(W_{11} + W_{22}) \pm \sqrt{(W_{11} - W_{22})^2 + 4W_{12}^2}\right]. \tag{4.16}$$

Denoting the eigenvectors of the matrix W as y_1' and y_2', equation 4.14 can be rewritten in the form;

$$Q = \frac{1}{r}\left(\lambda_1 {y_1'}^2 + \lambda_2 {y_2'}^2\right). \tag{4.17}$$

Comparing coefficients from equations 4.17 and 4.11, the eigenvectors of y_1' and y_2' can be considered as the unit vectors along the ellipse's semi-major and semi-minor axes (Figure 4.2); one also obtains: $G_1 + G_2 = \lambda_1$ and $G_1 = \lambda_2$, hence:

$$\begin{aligned} G_1 &= 0.5\left(W_{11} + W_{22} - \sqrt{(W_{11} - W_{22})^2 + 4W_{12}^2}\right), \\ G_2 &= \sqrt{(W_{11} - W_{22})^2 + 4W_{12}^2}. \end{aligned} \tag{4.18}$$

From the eigenvalue problem, it is known that the orthogonal rotation matrix, R_{φ_0}, relates the two coordinate systems as follows

$$\begin{bmatrix} y_1 \\ y_2 \end{bmatrix} = R_{\varphi_0} \begin{bmatrix} x_1 \\ x_2 \end{bmatrix}, \tag{4.19}$$

where the rotation angle (φ_0) obeys (e.g., Lax, 1997)

$$\tan 2\varphi_0 = \frac{2W_{12}}{W_{11} - W_{22}}. \tag{4.20}$$

This results in two values for φ_0 where $\varphi_0^{(1)} = \pi/2 + \varphi_0^{(2)}$. Using the trigonometric identity $\tan 2\varphi_0 = \dfrac{2\tan\varphi_0}{1-\tan^2\varphi_0}$, one can obtain the two values of φ_0 as:

$$\tan \varphi_0 = \frac{W_{11} - W_{22} \pm \sqrt{(W_{11} - W_{22})^2 + 4W_{12}^2}}{2W_{12}}. \tag{4.21}$$

Equation 4.21 is used by Jenner (2002) without rigorous derivation, and is equivalent to the equation introduced by Grechka and Tsvankin (1998) to determine the fracture orientation from the azimuthal variation of the NMO velocity.

4.4 AVAZ inversion for fracture orientation

Substituting equation 4.12 into equation 4.4, the small-incident-angle approximation to the PP reflection coefficient becomes

$$R_{PP}^{HTI} = I + \left(W_{11}\cos^2\varphi + 2W_{12}\cos\varphi\sin\varphi + W_{22}\sin^2\varphi\right)\sin^2\theta. \tag{4.22}$$

Incorporating the corrected pre-stack PP reflection amplitudes from different azimuths and small incident angles as the input data (D_{nm}), equation 4.22 can be used to express a linear system of "nm" equations in three unknowns:

$$\begin{bmatrix} \cos^2\varphi_1 \sin^2\theta_{11} & 2\cos\varphi_1 \sin\varphi_1 \sin^2\theta_{11} & \sin^2\varphi_1 \sin^2\theta_{11} \\ \vdots & \vdots & \vdots \\ \cos^2\varphi_1 \sin^2\theta_{n1} & 2\cos\varphi_1 \sin\varphi_1 \sin^2\theta_{n1} & \sin^2\varphi_1 \sin^2\theta_{n1} \\ \vdots & \vdots & \vdots \\ \vdots & \vdots & \vdots \\ \cos^2\varphi_m \sin^2\theta_{1m} & 2\cos\varphi_m \sin\varphi_m \sin^2\theta_{1m} & \sin^2\varphi_m \sin^2\theta_{1m} \\ \vdots & \vdots & \vdots \\ \cos^2\varphi_m \sin^2\theta_{nm} & 2\cos\varphi_m \sin\varphi_m \sin^2\theta_{1m} & \sin^2\varphi_m \sin^2\theta_{1m} \end{bmatrix}_{(nm\times 3)} \begin{bmatrix} W_{11} \\ W_{12} \\ W_{22} \end{bmatrix}_{(3\times 1)} = \begin{bmatrix} R_{11} - I \\ \vdots \\ R_{n1} - I \\ \vdots \\ \vdots \\ R_{1m} - I \\ \vdots \\ R_{nm} - I \end{bmatrix}_{(nm\times 1)} \tag{4.23}$$

where m is the number of azimuths, and n is the number of incident angles at each azimuth. The AVO intercept, I, can be calculated using a smooth vertical P-wave velocity and density. The matrix form of equation 4.23 can be written as,

$$G_{nm\times 3} X_{3\times 1} = D_{nm\times 1}. \tag{4.24}$$

The unknown vector $X = (W_{11}, W_{12}, W_{22})$ can be obtained from a damped least-squares inversion, as $X_{est} = (G^T G + \mu I)^{-1} G^T D$, where μ is the damping factor[2]. Here, X_{est} is obtained by using singular value decomposition, SVD, of the coefficient matrix G (Appendix H). After the AVAZ inversion, knowing W_{ij}, equation 4.21 is used to estimate the fracture orientation.

4.5 AVAZ inversion for fracture intensity

Assuming the fracture orientation, φ_0, as known, the PP reflection coefficient in equation 4.3 can be considered as a function of six parameters ($\frac{\Delta\alpha}{\alpha}, \frac{\Delta\beta}{\beta}, \frac{\Delta\rho}{\rho}, \Delta\epsilon^{(V)}, \Delta\delta^{(V)}, \Delta\gamma$).

[2] I is the 6×6 Identity matrix.

Equation 4.3 can be written as

$$R_{PP}^{HTI} = A\frac{\Delta\alpha}{\bar{\alpha}} + B\frac{\Delta\beta}{\bar{\beta}} + C\frac{\Delta\rho}{\bar{\rho}} + D\,\Delta\epsilon^{(V)} + E\Delta\delta^{(V)} + F\Delta\gamma, \tag{4.25}$$

where A, B, C, D, E, and F are defined as in equation 4.3. These coefficients are functions of θ, the azimuth, and the velocity model, as

$$\begin{aligned}
A &= \left(\frac{1}{2\cos^2\theta}\right), \qquad (4.26)\\
B &= -\left(\frac{4\beta^2}{\alpha^2}\sin^2\theta\right),\\
C &= \left(\frac{1}{2} - \frac{2\beta^2}{\alpha^2}\sin^2\theta\right),\\
D &= \left(\frac{1}{2}\cos^4(\varphi-\varphi_0)\sin^2\theta\tan^2\theta\right),\\
E &= \left(\frac{1}{2}\cos^2(\varphi-\varphi_0)\sin^2\theta + \frac{1}{2}\cos^2(\varphi-\varphi_0)\sin^2(\varphi-\varphi_0)\sin^2\theta\tan^2\theta\right),\\
F &= \left(\frac{4\beta^2}{\alpha^2}\cos^2(\varphi-\varphi_0)\sin^2\theta\right).
\end{aligned}$$

Incorporating the corrected pre-stack PP amplitudes from different azimuths and incident angles (e.g., wide-angle up to $(5° - 7°)$ before the critical angle) as the input data in D_{mn} below, equation 4.25 can be used to express a linear system of "mn" equations in six unknowns:

$$\begin{bmatrix}
A_{1\varphi_1} & B_{1\varphi_1} & C_{1\varphi_1} & D_{1\varphi_1} & E_{1\varphi_1} & F_{1\varphi_1}\\
\vdots & \vdots & \vdots & \vdots & \vdots & \vdots\\
A_{n\varphi_1} & B_{n\varphi_1} & C_{n\varphi_1} & D_{n\varphi_1} & E_{n\varphi_1} & F_{n\varphi_1}\\
\vdots & \vdots & \vdots & \vdots & \vdots & \vdots\\
\vdots & \vdots & \vdots & \vdots & \vdots & \vdots\\
A_{1\varphi_m} & B_{1\varphi_m} & C_{1\varphi_m} & D_{1\varphi_m} & E_{1\varphi_m} & F_{1\varphi_m}\\
\vdots & \vdots & \vdots & \vdots & \vdots & \vdots\\
A_{n\varphi_m} & B_{n\varphi_m} & C_{n\varphi_m} & D_{n\varphi_m} & E_{n\varphi_m} & F_{n\varphi_m}
\end{bmatrix}_{(nm\times 6)}
\begin{bmatrix}
\Delta\alpha/\alpha\\ \Delta\beta/\beta\\ \Delta\rho/\rho\\ \Delta\epsilon^{(V)}\\ \Delta\delta^{(V)}\\ \Delta\gamma
\end{bmatrix}_{(6\times 1)}
=
\begin{bmatrix}
R_{11}\\ \vdots\\ R_{n1}\\ \vdots\\ \vdots\\ R_{1m}\\ \vdots\\ R_{nm}
\end{bmatrix}_{(nm\times 1)} \tag{4.27}$$

where m is the number of azimuths, and n is the number of offset at each azimuth. Equation 4.27 in matrix form can be written as,

$$G_{nm\times 6}X_{6\times 1} = D_{nm\times 1}. \tag{4.28}$$

The unknown vector X can be estimated from a damped least-squares inversion,

$$X_{est} = (G^T G + \mu I)^{-1} G^T D, \tag{4.29}$$

where μ is the damping factor. Again, the estimates of the six-parameter vector X_{est} are obtained by using singular value decomposition (Appendix H).

4.6 The application of the AVAZ inversions

The proposed AVAZ inversions for fracture orientation and intensity were tested on the previously described physical model reflection data. The corrected reflection amplitudes from the top of the simulated fractured layer, from nine long-offset common midpoint (CMP) gathers acquired along azimuths of 0°, 14°, 27°, 37°, 45°, 53°, 63°, 76°, and 90°, were input to the AVAZ inversions.

At each azimuth for a given offset and depth of the fractured layer, the primary ray-path was traced to determine θ. Using a smooth isotropic background velocity model, a PP ray-tracing algorithm for horizontal isotropic layering was used to obtain θ, and then to calculate the coefficients A, B, C, D, E, and F (equation 4.26). Estimates of the six parameters ($\frac{\Delta\alpha}{\bar{\alpha}}, \frac{\Delta\beta}{\bar{\beta}}, \frac{\Delta\rho}{\bar{\rho}}, \Delta\epsilon^{(V)}, \Delta\delta^{(V)}, \Delta\gamma$) are then calculated by solving the linear system in equation 4.27. 1% of the maximum singular value of the matrix G is used as the damping factor.

In the analytical derivation of the plane-wave isotropic Aki and Richards (1980) approximation, and its anisotropic extension by Rüger (1997), "θ" is the incident angle. Shuey (1985) showed that using the average angle (average of the incident and transmission angles across the boundary) for "θ" results in a better approximation, verified this by numerical examples. Since the Shuey (1985) work , the average angle has been regularly used in AVO approximations. Hence, the average angle is used for θ in this thesis.

When testing any AVO inversion technique, in particular AVAZ inversion, the influence of the accuracy of the background velocity model has always been a question, particulary in a linear AVO inversion, where the coefficients are calculated from the background velocity. Therefore, the influence of the background velocity on AVAZ inversions should be examined.

The AVAZ inversion for fracture orientation seeks the azimuths of the maximum and minimum of the gradient, which defines the two eigenvectors (equation 4.17). Then, the rotation that matches the acquisition coordinate system to the eigenvectors provides the fracture orientation. Hence, to obtain an accurate estimate of the fracture orientation, it is important not to include any erroneous azimuthal variation in the gradient. The concerns over false amplitude variation also apply in the AVAZ inversion for the six parameters. For the physical model data used in this thesis, the very near offset anomaly, previously discussed in section 3.5.1, appears as an azimuthal variant and can be considered to be a false amplitude variation. Therefore, its effect should be considered before incorporating the near-offset data in any AVAZ inversion.

It is essential to both AVAZ inversions to include large incident angle data with a clear azimuthal variation. As Rüger's plane-wave approximation is not valid near the critical angle, and since for the plexiglas-phenolic reflector, the azimuthal amplitude variations appear only at large incident angles, then the question of how large the maximum incident angle data should be in the inversions needs to be considered. Observing azimuthal variations only at large incident angles might be valid for many datasets in the weak anisotropy category, and is not unique to the material used in this thesis.

For the AVAZ inversions discussed here, the effect of the following three factors on the inversion results have been investigated:

- the very near offset anomaly in the data,
- accuracy of the background velocity,
- maximum incorporated incident angle of the input data.

The accuracy of the AVAZ inversions with some possible scenarios highlighting these three factors is examined next.

4.7 Estimated orientation of the simulated fractured layer

While acquiring data from the physical model above, the symmetry of the simulated fractured medium was known, and the acquisition coordinates were aligned with the simulated fracture system. Next, the acquisition coordinate system was rotated to arbitrary directions, and the proposed AVAZ inversion was used to estimate the fracture orientation. In the inversion process, wide-angle data up to 46°, and a highly smoothed background velocity (Figure 4.3), were used. Table 4.1 shows the estimated fracture orientations. Having a simulated fractured medium with known symmetry directions, the AVAZ inversion estimates indicate the capability of the method to successfully estimate the fracture orientation.

Table 4.1: Estimated fracture orientation from the AVAZ inversion.

True φ_0	0°	10°	20°	40°	50°	60°	80°
Estimated φ_0	0.8°	10.8°	20.8°	40.8°	50.8°	60.8°	80.8°
	90.8°	100.8°	110.8°	130.8°	140.8°	150.8°	170.8°

As the method essentially calculates the direction of the eigenvectors of the gradient ellipse, no matter the orientation of the acquisition coordinate system with respect to the fracture system, the error of the estimated orientation depends on the input data only. Hence, for all rotations the constant error of 0.8° was obtained. The method was successful in predicting the fracture orientation; however, there is an ambiguity in the estimation as the method predicts both the fracture orientation and the direction normal to it (symmetry axis).

4.7.1 Influence of the near offset data

The effect of the very near-offset anomaly which appears at incident angles less than 10°, on the AVAZ inversion result, have been investigated. As there is almost no azimuthal variation for incident angles up to 37°, the influence of the small incident angle data on the AVAZ inversion results has also been investigated.

For the maximum incorporated incident angle of 46°, and using a highly smoothed background velocity, Table 4.2 shows the effect of small-incident-angle data on the estimated orientation. Table 4.2 suggests the following points:

- The very near offset anomaly has almost no effect on the orientation estimates from AVAZ inversion.
- Omitting data for angles less than 30° has almost no effect on the inversion results, as there is hardly any azimuthal variation observable up to this point. However, omitting more data, up to 37° for instance, appears to add small errors to the estimated orientation.

The result of this test for the AVAZ inversion for the orientation, suggests using whole dataset with no omissions at the near offsets.

4.7.2 Influence of the background velocity model

The influence of the background velocity on the fracture orientation estimate from the AVAZ inversion has also been investigated. The true velocity model is being smoothed using a polynomial fit for various order of the polynomials. Figure 4.3 shows four choices

Table 4.2: The effect of the small-incident-angle data on the estimated orientation.

data used	error of φ_0
$0 \leq \theta \leq 46$	$0.81°$
$3 \leq \theta \leq 46$	$0.82°$
$6 \leq \theta \leq 46$	$0.96°$
$9 \leq \theta \leq 46$	$1.24°$
$12 \leq \theta \leq 46$	$0.91°$
$15 \leq \theta \leq 46$	$0.65°$
$20 \leq \theta \leq 46$	$0.01°$
$30 \leq \theta \leq 46$	$-1.3°$
$37 \leq \theta \leq 46$	$-6.2°$

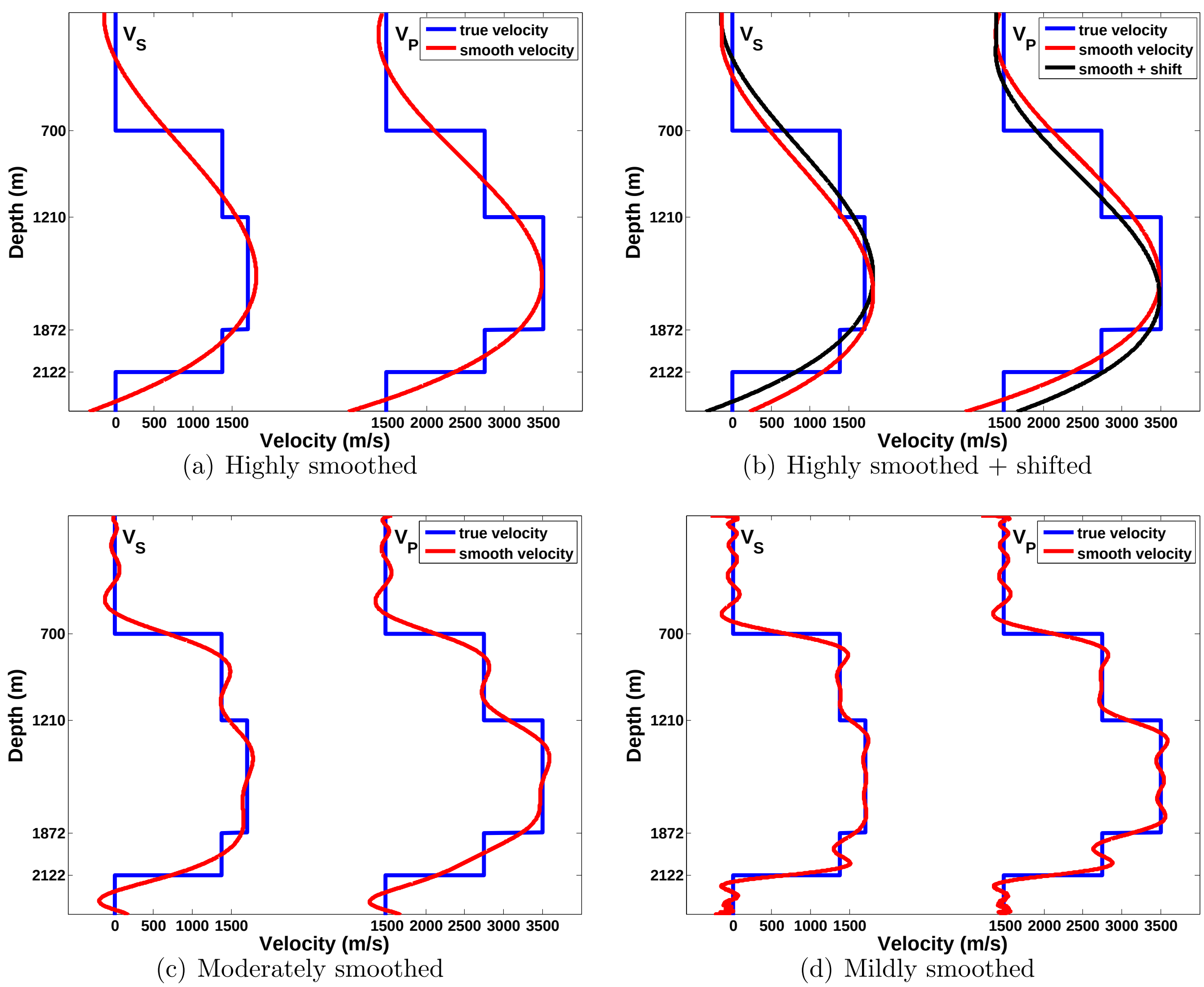

(a) Highly smoothed (b) Highly smoothed + shifted (c) Moderately smoothed (d) Mildly smoothed

Figure 4.3: Four differently smoothed background velocity models.

for the background velocity model; the choice (b) is the highly smoothed velocity model, shifted down by 100m. Table 4.3 shows the accuracy of the estimated orientation for these background velocities, when all data up to a maximum incident angle of 46° are used. Table 4.3 suggests the following points:

- The inversion for orientation performs very stably with different smoothed background velocities. Smoothing the background velocity has almost no effect on the estimated orientation .
- The highly smoothed velocity model, although it hides many details of the model, is the best choice. This is a realistic choice, similar to a real data situation where details might not be available.

Table 4.3: The effect of the background velocity model on the estimated orientation.

background velocity	error of φ_0
true velocity	0.83°
mildly smoothed velocity	0.83°
moderately smoothed velocity	0.83°
highly smoothed velocity	0.81°
highly smoothed + shifted velocity	0.81°

4.7.3 Influence of the maximum incorporated incident angle

The effect of the maximum incorporated incident angle on the orientation estimate from the AVAZ inversion has also been investigated. Table 4.4 shows the orientation estimate error when all available small-incident-angle data and the highly smoothed background velocity are used. Table 4.4 indicates the following points:

- Incorporating only small-incident-angle data (less than 36°), where the azimuthal amplitude variations are negligible, generates orientation estimates with large errors.

- Large incident angle data, where a clear azimuthal variation is observable, are required for an accurate estimate of the fracture orientation.
- Very large incident angle data, close to the critical angle, should be avoided. However, they still produce less error than using small-incident-angle data only.

Table 4.4: The effect of the maximum incident angle on the estimated orientation.

max incident angle	error of φ_0
36°	21°
38°	18°
40°	18°
42°	13°
44°	6°
45°	4°
46°	0.8°
47°	−1.9°
48°	−4.6°
50°	−7.37°

4.8 Estimated anisotropy parameters of the simulated fractured medium

Once the fracture orientation for our simulated fractured medium is known, the proposed simultaneous six-parameter AVAZ inversion, for $(\Delta\alpha/\alpha, \Delta\beta/\beta, \Delta\rho/\rho, \epsilon^{(V)}, \delta^{(V)}, \gamma)$, was applied to the physical model data. The main goal is to obtain accurate estimates of the three anisotropy parameters $(\epsilon^{(V)}, \delta^{(V)}, \gamma)$, where the γ-parameter is directly related to fracture intensity. The estimates of the six parameters from the AVAZ inversion of all azimuth data, using the incident angle data of $(9^\circ \leq \theta \leq 46^\circ)$ and the highly smoothed background velocity model, are shown in Figure 4.4. The errors have been obtained by comparing the results to the ones previously obtained for the simulated fractured layer by traveltime inversion in Chapter 2. The AVAZ inversion was successful in obtaining favorable results for all six parameters with a maximum error of 20% for $\epsilon^{(V)}$.

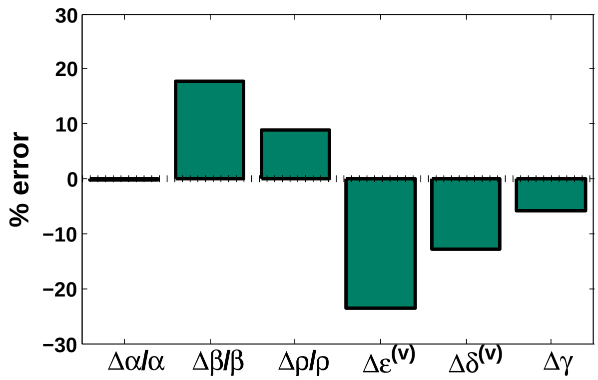

Figure 4.4: AVAZ inversion for the six parameters, using azimuth data with incident angles from 9° to 46°, and the highly smoothed background velocity.

4.8.1 Influence of the near offset data

The sensitivity of the six-parameter AVAZ inversion to the mentioned three different factors is investigated next, in a manner similar to that for the AVAZ inversion for orientation. The effect of the very near-offset anomaly, which varies with azimuth, has been investigated. For the maximum incorporated incident angle of 46°, and using the highly smoothed background velocity, Figure 4.5 shows the influence of small incident angle data on the estimates of the six parameters. Figure 4.5 indicates the following points:

- Unlike in the AVAZ inversion for orientation, the very near-offset anomaly imposes erroneous azimuthal effects and changes the estimates noticeably. This applies especially to the first three terms.
- Eliminating incident angles smaller than 9° results in better estimates. This differs from the AVAZ inversion for orientation where all incident angle data could be included.
- The small incident angle data have a rather large influence on the estimates of the first three (isotropy) terms, and a small effect on the estimates of the last three (anisotropy) terms.

- It is better to include the incident angles down to 9° rather than eliminating these azimuthally invariant data; inversion of data from incident angles larger than 15° produces larger error especially for the isotropic terms. This can be predicted from theory (equation 4.3); the normal incident angle data give the estimate of $\Delta\alpha/\alpha + \Delta\rho/\rho$.

4.8.2 Influence of the background velocity model

Figure 4.6 demonstrates the influence of the background velocity model on the six-parameter AVAZ inversion, when the incident angle data between 9° and 46° are used. It indicates the following points:

- The background velocity has a stronger effect on the estimates of the six parameters, compared to the AVAZ inversion for orientation. Nevertheless, the background velocity does not effect the inversion results strongly.
- If a representative background velocity is chosen, the six-parameter AVAZ inversion is capable of producing good results.

It is unexpected that the six-parameter AVAZ does not produce better estimates using the true velocity model. This might reflect the fact that Rüger's equation is approximate and not exact. The true velocity model here is a large-contrast example. Therefore, it is expected that Rüger's equation also has rather large errors for this large-contrast example, similar to the Aki and Richards (1980) approximation as reported in (Innanen, 2012). Another thought might be that the difficulties in the ray-tracing algorithm for large-contrast velocity models causes the results to be less perfect for the true velocity model.

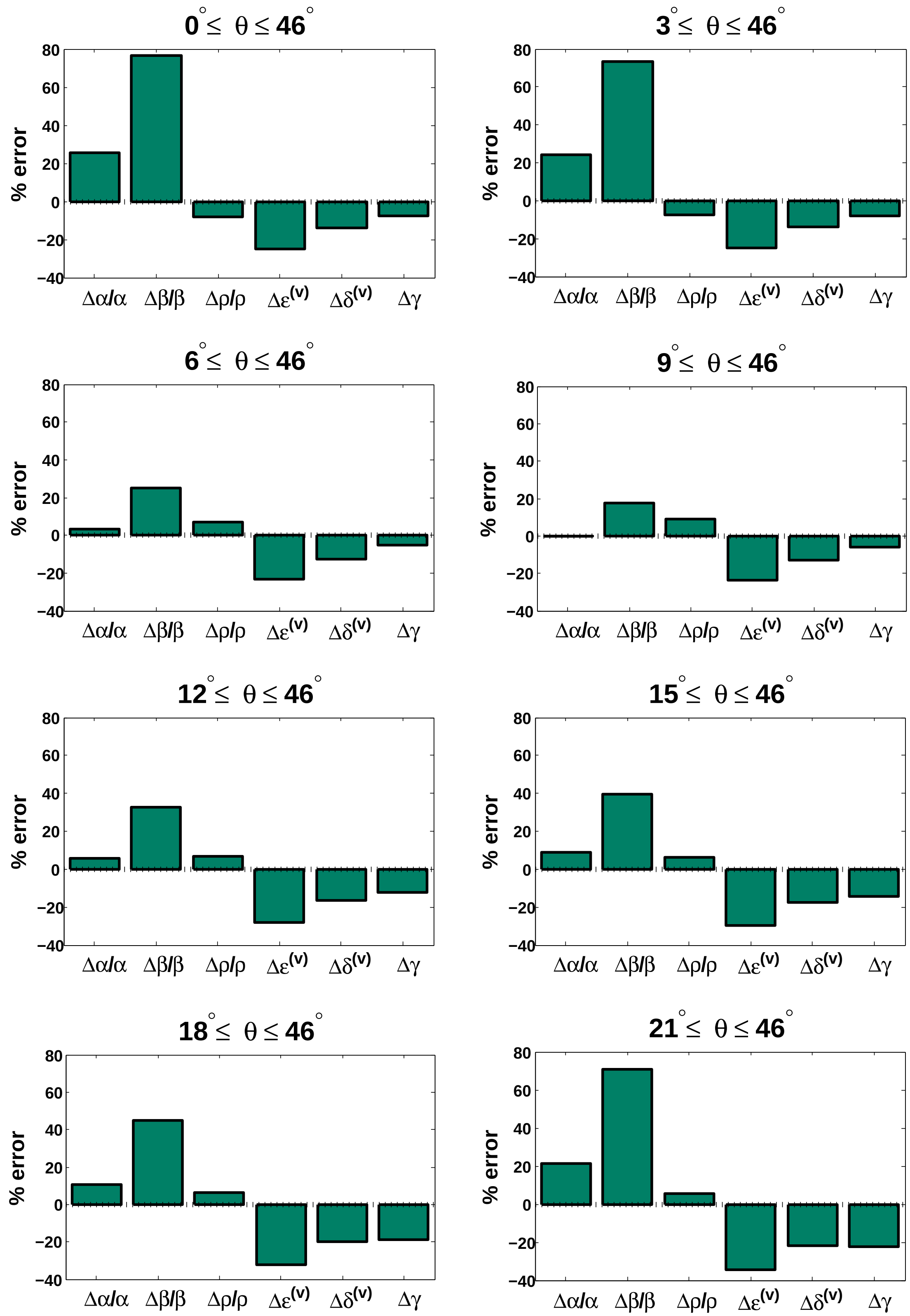

Figure 4.5: The effect of small-incident angle data on the six-parameter AVAZ inversion.

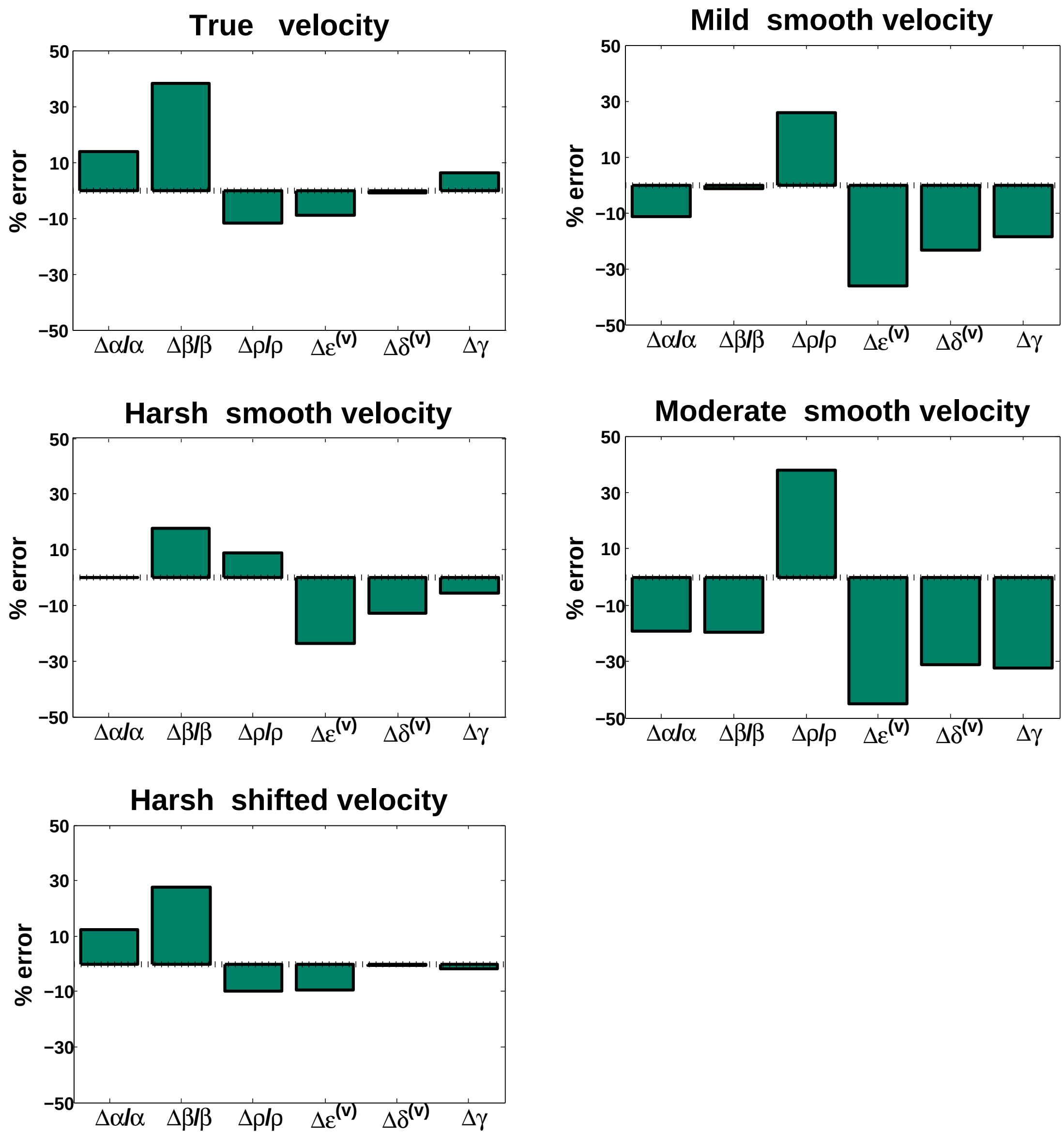

Figure 4.6: The six-parameter AVAZ inversion results for different background velocities.

4.8.3 Influence of the maximum incorporated incident angle

Figure 4.7 shows the six-parameter inversion estimate errors for different maximum incorporated incident angles, when the highly smoothed background velocity and a minimum incident angle of 9° are used. Figure 4.7 indicates the following points:

- For the proper choice of the maximum incorporated incident angle (between 44° and 48°), the linear AVAZ inversion results in reasonable estimates for all six parameters.
- The six-parameter AVAZ inversion using incident angles of less than 39° produces good estimates for the isotropy terms. This indicates a higher influence of the small-incident-angle data on the estimates of the isotropy terms. The small-angle data do not produce good estimates for the three anisotropy parameters, since the data do not exhibit any noticeable azimuthal amplitude variations at this point. Note that estimates from input data between 9° and 37° produce large errors for the isotropy terms due to the a small amplitude anomaly between 35° and 37° which is clearly observable in Figure 3.20b-d.
- Incorporating large incident angles (e.g., 45°) within $5^\circ - 8^\circ$ of the critical angle can result in reasonable estimates of all six parameters.
- Incorporating very large incident angles, closer to the critical angle, does not result in better estimates of the anisotropy terms. The overall error for all six parameters are larger when incorporating incident angles close to the critical angle, since Rüger's linear equation is not valid in this region.

Deciding on the proper choice of the maximum incorporated angle, especially as a recommendation for an application to field data, the model resolution matrix (Appendix H) of the coefficient matrix G, for various maximum incident angles, has been examined. The model resolution matrix defines how well the estimated values resembles the true solution. In the case of a perfect solution, the resolution matrix should be a 6×6 iden-

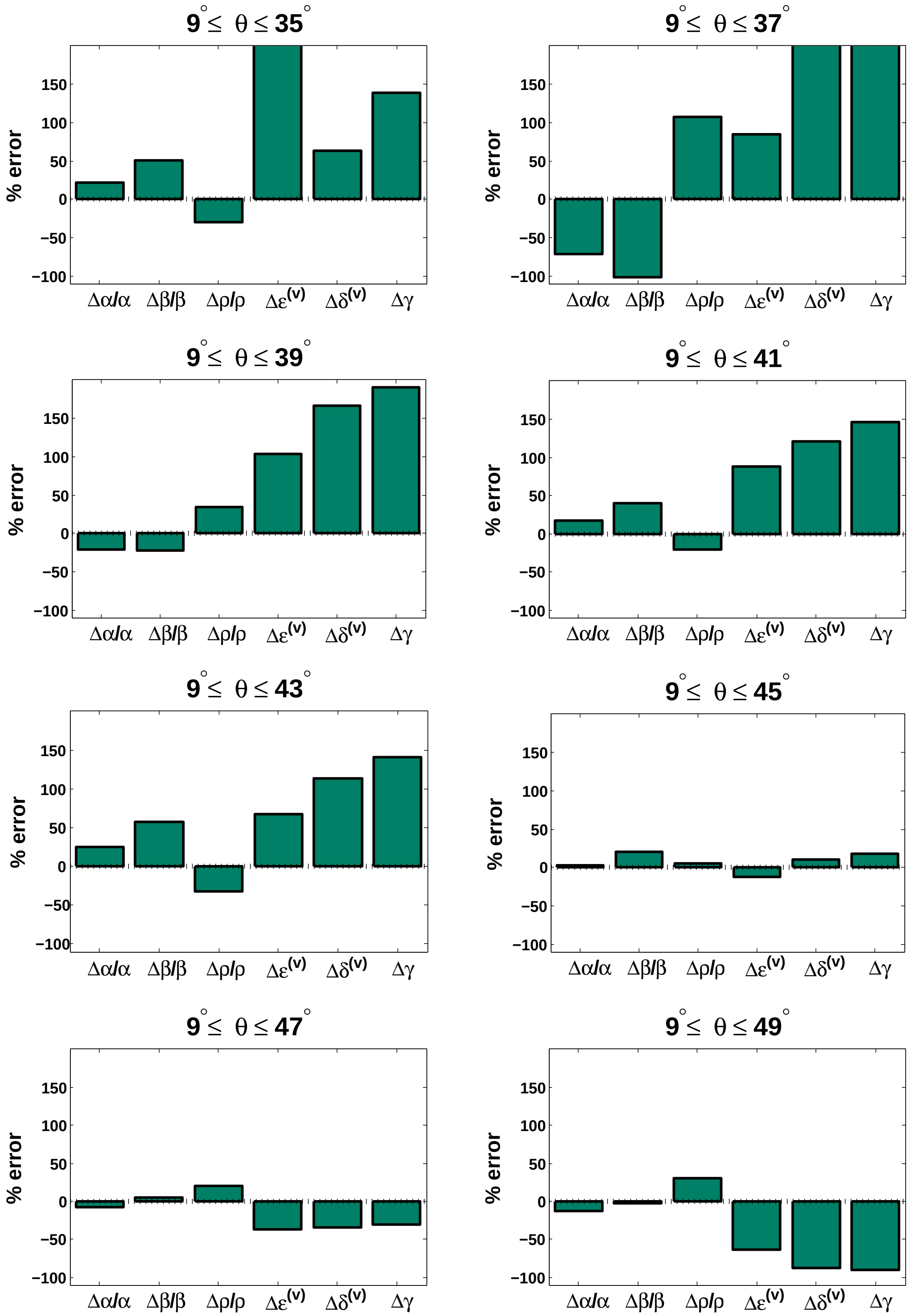

Figure 4.7: Six-parameter AVAZ inversion for various maximum incorporated incident angles. The estimates are compared to the values previously estimated from traveltime inversion.

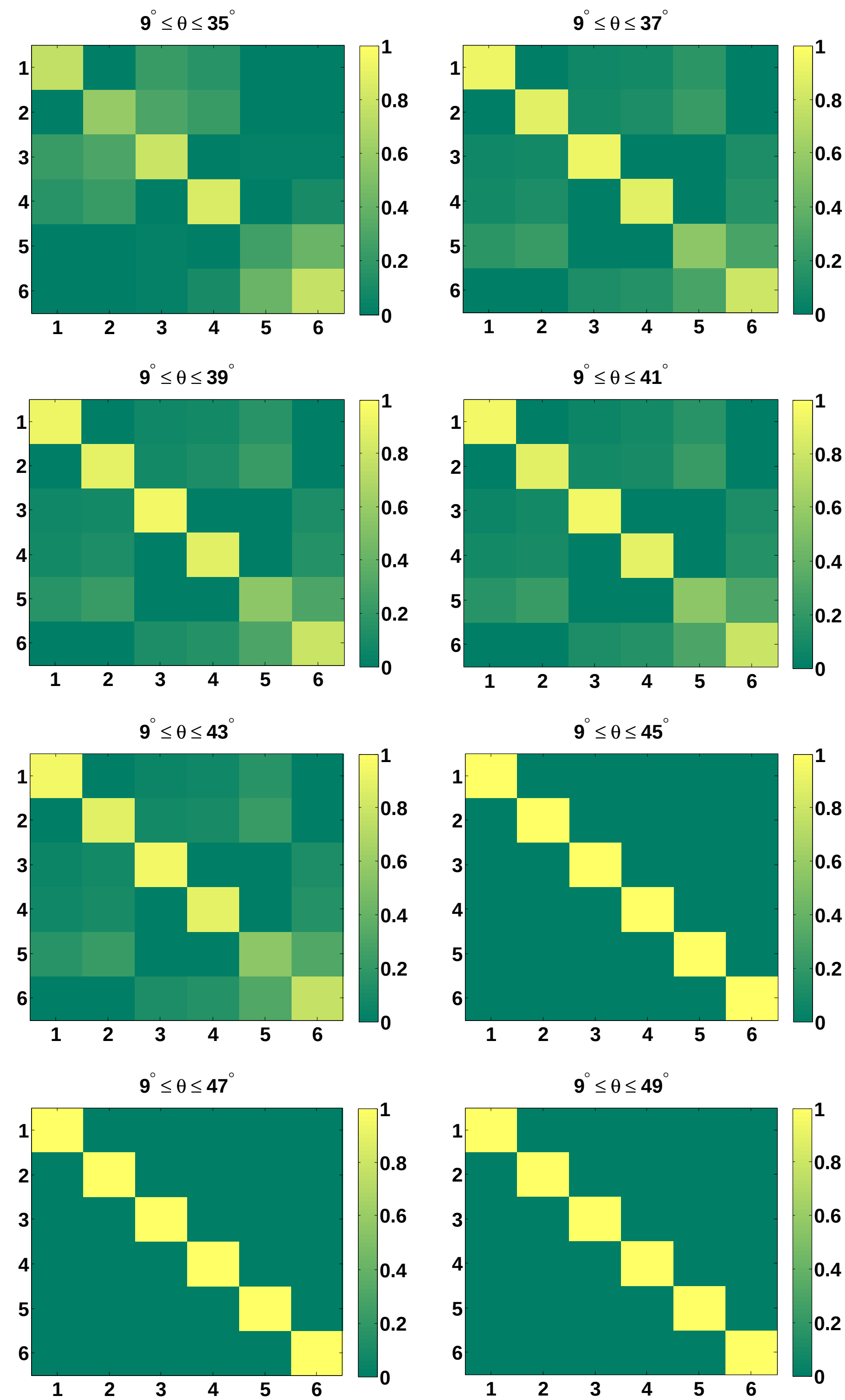

Figure 4.8: The model resolution matrix of the six-parameter AVAZ inversion for various maximum incorporated incident angles.

tity matrix, which means each parameter is estimated independently from the others. Figure 4.8 shows that the model resolution matrix, for the proper choice of the maximum incident angle and larger angles, is the perfect identity matrix. For the smaller maximum incident angles, the non-unit diagonal elements of the model resolution matrix imply that the estimates are linear combinations of the true values. By gradually increasing the maximum incident angle of the input data for the six-parameter AVAZ inversion, and searching for an identity model resolution matrix, the proper maximum incident angle can be detected once the identity model resolution matrix is obtained.

4.9 Limited azimuth data in the six-parameter AVAZ inversion

Theoretically, using input data from even one single azimuth should be able to produce estimates of the six parameters. However, the AVAZ inversion, with several input azimuth data, is expected to give superior results compared to an amplitude inversion using single azimuth input data, because of the statistical leverage. Least-squares fitting of more input data produces a better fitted curve than using only a few input data points. Figure 4.9 shows the six-parameter AVAZ inversion with the single azimuth input data. Comparison of Figure 4.4 to Figure 4.9 shows that, by using all azimuth data, the AVAZ method gives markedly superior estimates of all six parameters.

The superior behavior of the six-parameter AVAZ inversion, when using all azimuth data, can also be observed by examining the model resolution matrix. The model resolution matrixes of the six-parameter AVAZ inversion, by using all the azimuth data and single azimuth data as input, are given in Figure 4.10. The six-parameter AVAZ inversion is applied using the highly smooth background velocity, and incident angles between 9° and 46°, for all cases. The singular values of the six-parameter AVAZ inversion, for mentioned input data, are listed in Table 4.5. The six-parameter AVAZ inversion, using the single azimuth input data, is unstable resulting in three zero singular values.

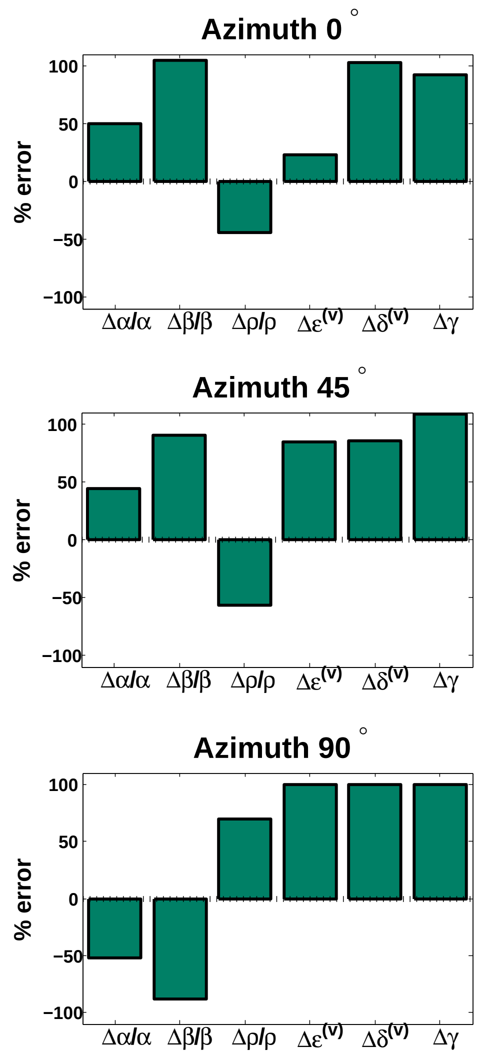

Figure 4.9: The six-parameter AVAZ inversion of single azimuth input data.

To further investigate on how much azimuth data are actually needed in the AVAZ inversion, the following two questions are answered:

- Are all azimuth data required for an accurate estimation of all six parameters?
- Do certain azimuths have more influence on the estimates of some of the six parameters?

To answer these two questions, azimuth data are divided into three regions:

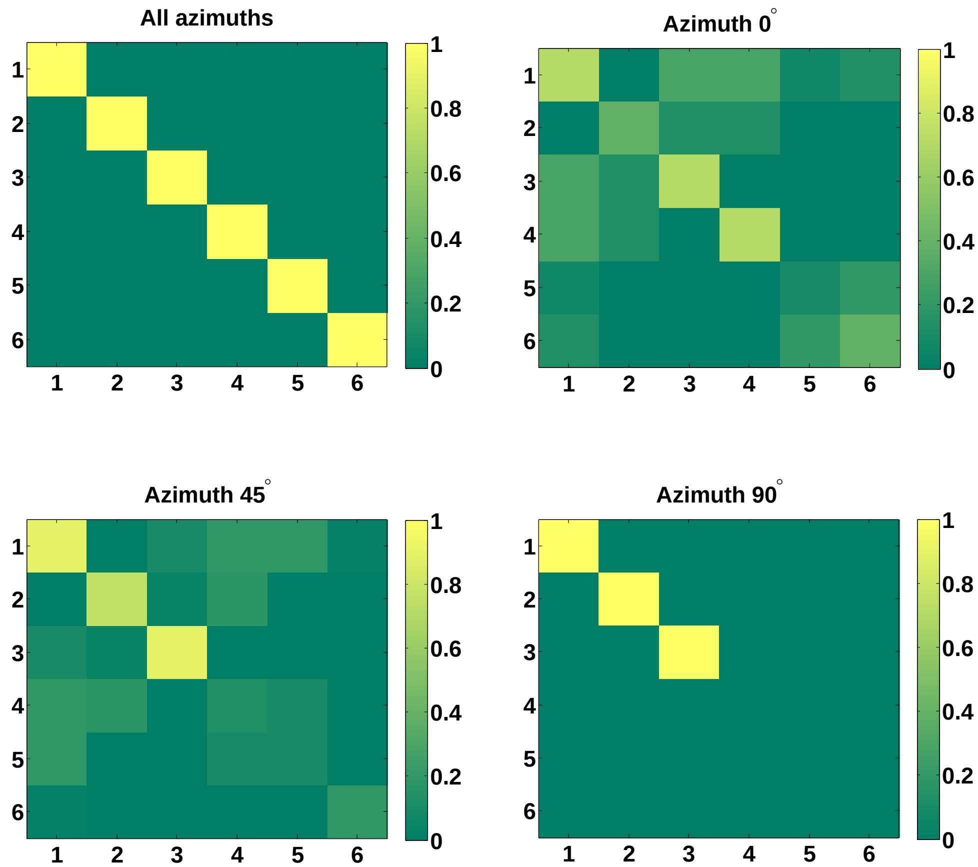

Figure 4.10: The model resolution matrix from the six-parameter AVAZ inversion using different azimuth input data.

Table 4.5: The singular values of the six-parameter AVAZ inversion with different input data.

	s_1	s_2	s_3	s_4	s_5	s_6
all azimuths	27.4	6.0	3.3	0.6	0.4	0.1
azimuth 0°	10.1	2.4	0.3	0.0	0.0	0.0
azimuth 45°	8.1	1.7	0.1	0.0	0.0	0.0
azimuth 90°	9.5	1.9	0.1	0.0	0.0	0.0

- Near sector, which includes azimuths of $0°, 14°$, and $27°$.
- Mid sector, which includes azimuths of $37°, 45°$, and $53°$.
- Far sector, which includes azimuths of $63°, 76°$, and $90°$.

Figure 4.11 shows the six-parameter AVAZ inversion of each sector, using the highly smooth background velocity and incident angles between $9°$ and $46°$. It shows the following points:

- The far sector has more influence on the isotropy terms' estimates. This is expected as the $90°$ azimuth is the direction of the isotropic plane of the simulated fractured layer.
- The near sector produces smaller errors for the anisotropy estimates, but is still inferior to the case when all azimuths are input in the inversion. This indicates the sensitivity of the AVAZ inversion to estimate anisotropy parameters. A widened range of azimuth data provides a more stable inversion.
- The mid sector produces intermediate results in terms of accuracy compared to the near and far sectors.

Figure 4.12 shows the six-parameter AVAZ inversion results using three sets of azimuth data only (one from each sector), using the highly smoothed background velocity and incident angles between $9°$ and $46°$. For a majority of azimuth choices, the AVAZ inversion of the reduced dataset produces results comparable to the case of using all azimuth data. Figure 4.13 shows model resolution matrices for the AVAZ inversion of limited azimuth data; for a majority of the examples, a close approximation to the identity model resolution matrix is obtained. Apparently, depending on the quality of the data used, some choices of the limited input data are sufficient to produce good estimates. However, it is not certain that all choices of limited azimuth data are capable of producing good estimates. It seems to be safest to use all azimuth data for reliable inversion results.

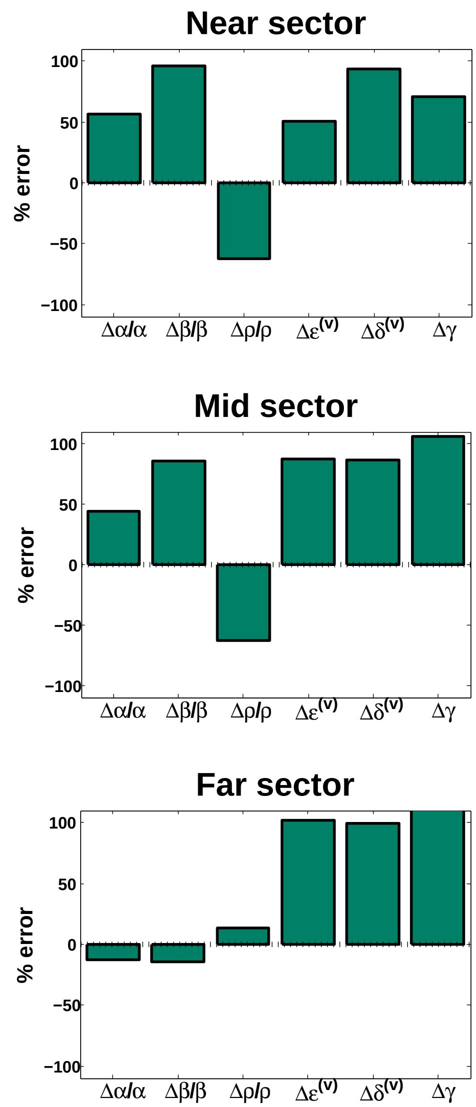

Figure 4.11: Accuracy of six-parameter AVAZ inversion using the near, mid, and far sector azimuth data.

4.10 Limited azimuth data in AVAZ inversion for fracture orientation

In the AVAZ inversion for orientation, some investigations were undertaken to determine whether all azimuth data are required for an accurate orientation. Using input data from a single azimuth, or from one sector only, and expecting to obtain the accurate estimate

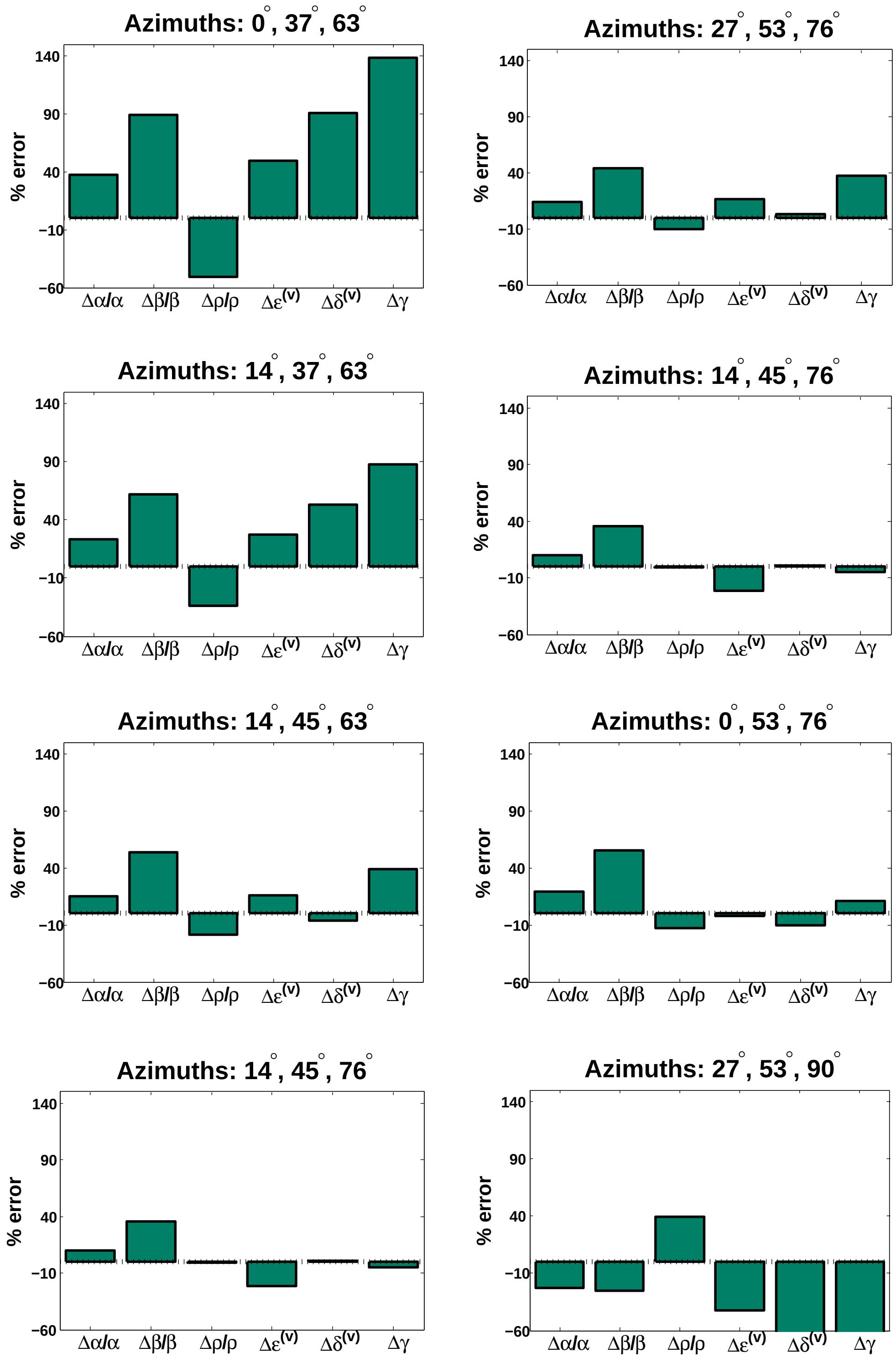

Figure 4.12: The six-parameter AVAZ inversion using the three azimuth data only.

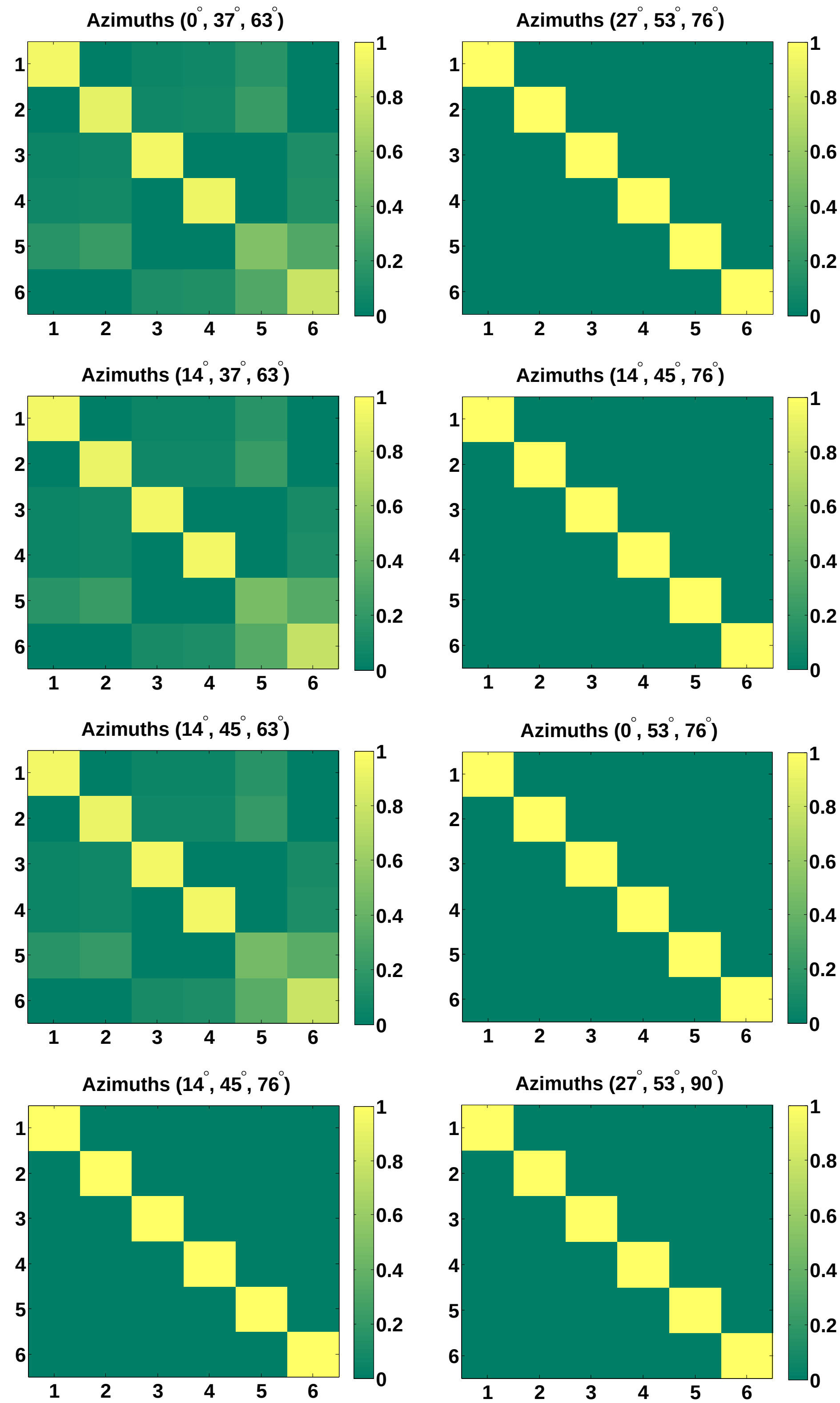

Figure 4.13: The model resolution matrix for the six-parameter AVAZ inversion using three azimuth data only.

for the orientation might not be rational. As previously mentioned, the AVAZ inversion for orientation essentially fits an ellipse to the AVO gradient. Using input data from one sector only, the AVAZ inversion estimates the extreme values of the gradient within that sector and is unable to predict the global minimum and maximum directions. Examining the influence of the input limited azimuth data on the AVAZ inversion for fracture orientation, at least three azimuth lines, one from each sector, should be provided.

Table 4.6 shows the orientation estimate errors for an AVAZ inversion using three sets of azimuth data only. The highly smoothed background velocity, and data with an incident angle of less than 46°, were used in this test. The inversion of limited azimuth data estimates the orientation to within 6°, except for one particular set $(14°, 45°, 63°)$ which has a high error of $-16°$. The inversion of this particular set of data was repeated using data with the small-incident-angle data eliminated, and it is found that the error is not an effect of the near-offset anomaly. The repetitions were based on data with incident angles of $9° \leq \theta \leq 46°$, $20° \leq \theta \leq 46°$, and $25° \leq \theta \leq 46°$. The orientation estimates had errors of $-15°$, $-14.3°$, and $-14°$, respectively. The poor estimate of the orientation, for this particular set of data, is most probably due to the presence of noise in the input data. It can be concluded that it is safest to use all azimuth data for a reliable orientation estimate, similar to the case of the six-parameter AVAZ inversion.

For the limited azimuth data, the AVAZ inversion for orientation results, (Table 4.6) compared to the six-parameter AVAZ inversion (Figure 4.12) results do not show a one-to-one correlation. Some choice of azimuths produced small errors for the six-parameter estimates but not a small error for the orientation estimate. However, the AVAZ inversion for orientation (Table 4.6) results do show a clear a one-to-one correlation to the model resolution matrix results (Figure 4.13. This most probably indicates that the six-parameter estimates from the traveltime inversion of Chapter 2 are not perfect.

Table 4.6: The AVAZ inversion for orientation using data for three selected azimuths only.

limited azimuth data	error of φ_0
azimuths $(0°, 37°, 63°)$	$6.4°$
azimuths $(0°, 45°, 90°)$	$-0.7°$
azimuths $(0°, 53°, 76°)$	$-0.3°$
azimuths $(27°, 53°, 76°)$	$4.0°$
azimuths $(14°, 37°, 63°)$	$3.7°$
azimuths $(14°, 45°, 63°)$	$-16.4°$
azimuths $(14°, 45°, 76°)$	$-2.8°$
azimuths $(27°, 53°, 90°)$	$-1.0°$

4.11 Summary

This chapter presented the pre-stack linear amplitude inversion procedures to extract the anisotropy parameters $(\epsilon^{(V)}, \delta^{(V)}, \gamma)$, and fracture orientation from the azimuthal variations in the PP reflection amplitudes. Since the shear-wave splitting factor, γ, is directly related to fracture intensity, the presented analysis shows that it is possible to relate the difference in P-wave azimuthal AVO variations directly to the fracture intensity of the simulated fracture layer.

The presented AVAZ inversion is based on the reflection coefficient approximations by Rüger (1997). The accurate AVAZ inversion estimates demonstrate that Rüger's equation is suitable for quantitative amplitude analysis of anisotropic targets, and can be employed in numerical inversion algorithms.

The analysis found that the maximum incorporated incident angle is the most important factor controlling the accuracy of the proposed linear AVAZ inversions. Applying the linear AVAZ inversions, with various maximum incorporated incident angles, demonstrated that the accurate inversion for the anisotropy parameters and fracture orientation requires wide-angle data. However, incorporating very large offset data close to the critical angle should be avoided, since linear plane-wave Rüger's approximation is not valid close to the critical angle. This result is based on comparing the estimated parameters to values previously obtained by traveltime inversion (Chapter 2). The investigation on the model resolution matrix of the AVAZ inversions, which defines how well the estimated values resemble the true solution, suggests that the optimal maximum incorporated incident angle is of the lower end of the range of angles which resulted in a nearly identity resolution matrix. The model resolution matrix analysis can be used independently without knowing the true values in advance. This indicates that the method outlined in this study could be easily implemented for seismic field data.

A background velocity model is required to calculate the coefficient matrix of the AVAZ inversions. In general, the effect of the background velocity model is a major concern for reliable estimates from a linear AVO inversion. The present analysis shows that a detailed background velocity model is not needed to obtain accurate estimations. This is good news for the application of the proposed AVAZ inversions on seismic field data for which a detailed velocity model is not usually available. The smoothed background velocity had almost no effect on the orientation estimate from the AVAZ inversion. The smoothed background velocity also did not largely effect the estimates of the six parameters. The highly smoothed background velocity produced even more accurate estimates for the six parameters. This is consistent with the results of the isotropic linear AVO inversion for P-impedance, S-impedance, and density (Figure 3.54 of Mahmoudian (2006)), in which the AVO inversion is less sensitive to background velocity errors. The sensitivity test shown here assumes horizontal layering, but the validation of the AVAZ inversions is not restricted to horizontal layering.

Inquiring as to the need of a full coverage of 3D azimuth data for reliable linear AVAZ inversions, the AVAZ inversions were applied to limited azimuth data. Estimates based on AVAZ inversions of limited azimuth data might be as good as estimates using all azimuth data, as long as data from all azimuth sectors are used. This statement certainly depends on the quality of the data used, as some choice of azimuths produced large errors for the estimates, and a corresponding non-identity model resolution matrix. It seems that, however, for accurate estimates of anisotropy parameters and the fracture orientation, using input data from all azimuth sectors is the safest choice. Examples given show that the far azimuth sector data have more influence on the isotropy terms' estimates.

The AVAZ inversion determines the fracture orientation with an inherent ambiguity, since it predicts both the directions of the isotropic plane and the symmetry axis of an HTI medium. For unique determination of the fracture orientation some other information is required, such as azimuthal NMO or shear-wave splitting. These effects are qualitatively different from azimuthal AVO and can be combined effectively to invert for fracture orientation.

Chapter 5

Summary, future directions, and conclusions

5.1 Summary

As outlined in the Introduction, the main goal of this thesis was to determine whether information regarding the anisotropy and directions of the symmetry planes of a fractured medium can be extracted from an amplitude analysis. Physical seismic modeling was used as the main tool in this investigation. Physical model seismic data have often been used for traveltime analysis, yet incorporating them in an amplitude analysis was limited due, in part, to the large size, highly-directional physical model transducers employed as sources and receivers. Using numerical simulations, the effect of large size transducers in measurements of the group and phase velocities, and on the amplitudes of physical model reflection data were investigated. By the edge-to-edge correction, the qP-velocity measurements are found to be less sensitive to transducer size. Phase velocity measurements using the (τ, p) transform method are only possible if small point-like transducers are available. For physical model reflection data, the highly-directional effect of transducers on reflection amplitudes was mitigated using a directivity correction.

In **Chapter 2** the construction and initial characterization of a simulated fractured medium is discussed. A straightforward method to determine the elastic stiffness coefficients of the orthorhombic phenolic model from group velocity measurements is detailed. The estimated stiffness coefficients are then shown to predict phase and group velocities consistent with the measured velocities.

In **Chapter 3** a careful acquisition of multi-offset, multi-azimuth, physical model reflection data over the simulated fractured layer are examined. In order to use the reflection amplitudes for an amplitude analysis, a deterministic amplitude correction procedure was applied to reflection amplitudes from two liquid-solid and solid-solid interfaces. The corrected amplitudes agreed with the predicated amplitudes from the Zoeppritz equation, indicating that the correction procedure properly reduces the reflection amplitudes to reflection coefficients required by an amplitude analysis.

In **Chapter 4** the AVAZ inversions to extract the anisotropy parameters and fracture orientation, based on the reflection coefficient approximations by Rüger (1997), is detailed. The sensitivity analysis indicates the necessity of using large offset data for a six-parameter AVAZ inversion. The estimated fracture orientation from AVAZ inversion has an inherent ambiguity, as it predicts both the fracture orientation and the direction normal to it.

5.2 Future directions

5.2.1 Further analysis on the 3D physical model data

Reflection amplitudes from only two interfaces, water-plexiglas1 and plexiglas1-phenolic were investigated in this thesis. Since the construction of and acquisition of data from the physical model took much longer than was anticipated, I was unable to do any further investigations on this 3D dataset. Testing all aspects of acquisition and equipments, more than 700 seismic gathers were acquired, while only a couple of them were actually required in the analysis of this thesis. Now that these 3D physical model reflection data is ready, and partially processed, some immediate analyses can be suggested:

- AVAZ analysis on the reflection amplitudes from the bottom of the simulated fractured layer (phenolic-plexiglas2 interface) to estimate the anisotropy parameters of the simulated fractured medium, similar to the AVAZ analysis applied to the amplitudes from the top of the fractured layer. A joint azimuthal amplitude analysis of both reflectors (plexiglas1-phenolic and phenolic-plexiglas2 interfaces) is also recommended.

- Azimuthal velocity variation analysis (traveltime analysis) of the NMO-velocity of the simulated fractured layer. This VVAZ analysis can be used to estimate the anisotropy parameters of the simulated fractured medium and may that be compared to the values estimated in this thesis. This might help in developing the existing VVAZ analysis applied by Tsvankin (1997).
- NMO and AVO data, which are qualitatively different, can be combined effectively and inverted for anisotropy parameters.
- An independent analysis also can be provided by converted wave data. The PS reflection from the plexiglas1-phenolic interface was clear and can be used. These converted wave amplitudes can also be used in a joint inversion with the PP amplitudes to invert for the elastic properties of the simulated fractured medium. Both NMO and amplitudes of converted waves contain viable information about the anisotropy. This physical model dataset can be used to appreciate the potential of converted-wave analysis in azimuthally anisotropic media.
- The deterministic amplitude correction procedure used in thesis requires the knowledge of the true velocity model of the overburden. For real data, the exact velocity is unknown, and usually some statistical amplitude corrections are employed. This dataset can provide the opportunity to evaluate the accuracy of some practical amplitude correction procedures, which is one possible area of interest in any AVO analysis.

5.2.2 New physical model experiments

As a result of the presented physical model data acquisition, and investigations on the effect of large size transducers, I believe that solid knowledge of properly collecting 3D physical model data from anisotropic models, and a procedure to preserve azimuthally varying amplitude signatures, have been gained in CREWES. Consequently, some future experiments on the presently available models at the CREWES physical modeling lab can be suggested:

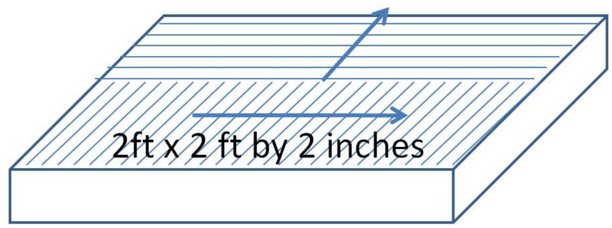

Figure 5.1: A model available in CREWES with two slabs of phenolic material, with perpendicular symmetry axes directions.

- Many exploration targets show several independent fracturing geometries. A medium with two sets of vertical fractures with different orientations is a good start to examine such targets. 3D physical model seismic data over the presently available model (Figure 5.1) at the CREWES physical modeling lab can provide significant insight for investigating such targets. This model has two slabs of phenolic material fused together, with perpendicular fracture orientations. Additionally, the amplitude analysis of 3D physical model data over a model with several sets of fractures with different orientations (Figure 5.2), can provide many insights into the exploration of fractured targets.
- A physical model with two consecutive anisotropic layers with two different fracture orientations, perhaps one with a tilted symmetry axis, sets a very good example toward a more realistic model.

5.2.3 Fracture orientation from amplitude analysis

The AVAZ inversion for fracture orientation has a 90° ambiguity. It predicts both the isotropic plane and the symmetry axis, the fast and slow directions, of the HTI medium.

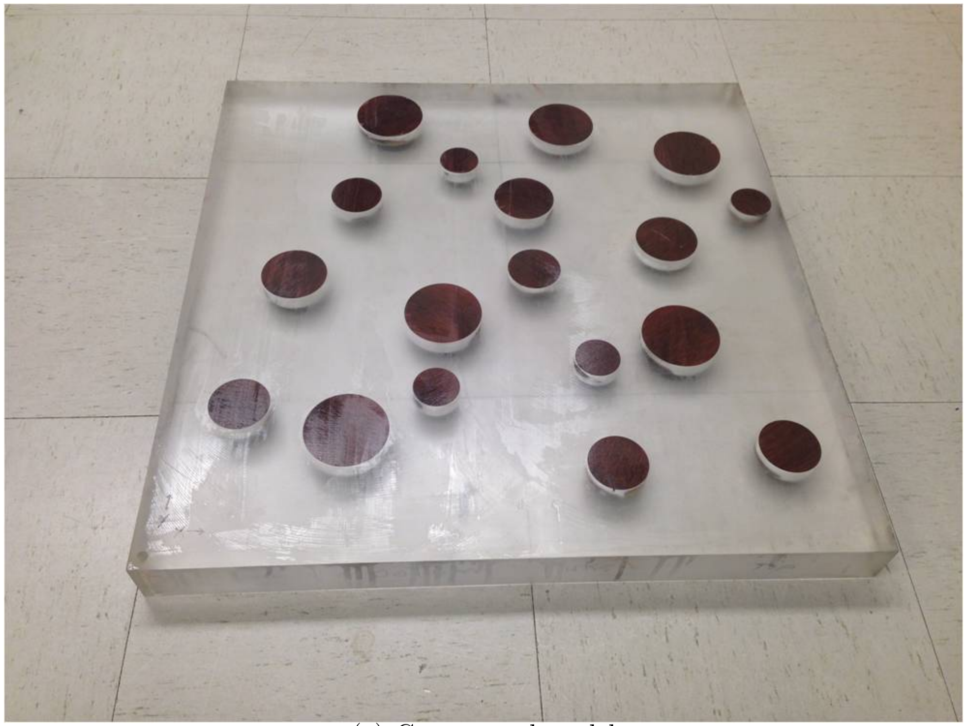

(a) Constructed model

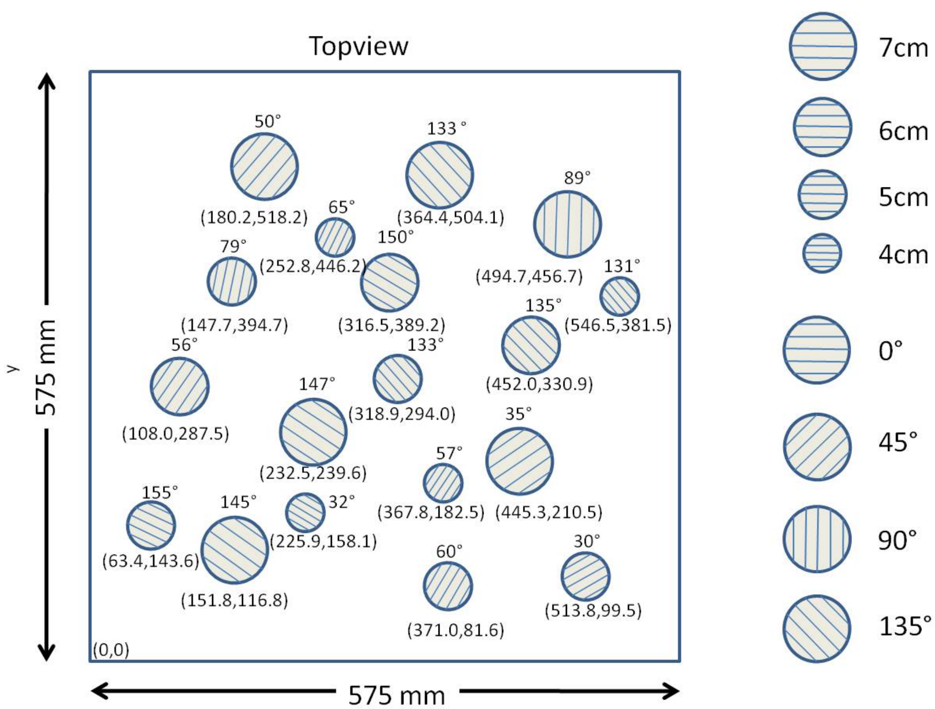

(b) Sketch model

Figure 5.2: An available model, already constructed, in CREWES with several patches of phenolic material, with symmetry axes of different directions, embedded in a plexiglas layer.

The current practise might not add any extra information to the fracture detection techniques. The smallest and largest values of the AVO gradient, for any AVO class (Figure 5.3), could give the same information even without the trouble of applying an AVAZ inversion. In the future, more investigation on the capability of an AVO analysis to extract the correct fracture orientation is needed.

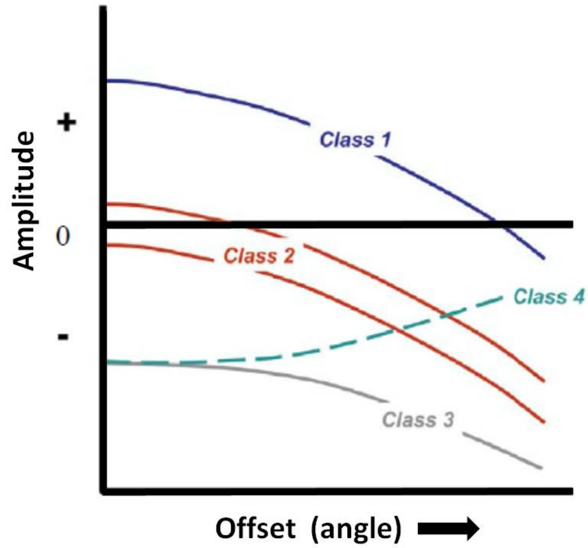

Figure 5.3: AVO classification (Castagna and Backus, 1993).

5.2.4 Orthorhombic PP reflection coefficients

Throughout this thesis, the simulated fractured layer was treated as an HTI medium. However, the phenolic model, although it is close to an HTI medium, is in fact orthorhombic. Orthorhombic symmetry is a more realistic model to describe a fractured medium. Vertical fractures in a VTI background medium, or a medium with two sets of fractures, or a medium with multiple sets of fractures, can be effectively modeled as an orthorhombic model. Some theoretical reviews on orthorhombic PP reflection coefficient approximation are presented below. This could potentially be used to extract the orthorhombic stiffness coefficients (anisotropy parameters) of the simulated fractured medium.

Table 5.1: Orthorhombic anisotropic parameters (Tsvankin, 1997). Note only seven of them are independent.

Thomsen parameter	ϵ	γ	δ
(x_2, x_3) plane	$\epsilon^{(1)} = \frac{A_{22}-A_{33}}{2A_{33}}$	$\gamma^{(1)} = \frac{A_{66}-A_{55}}{2A_{55}}$	$\delta^{(1)} = \frac{A_{23}+2A_{44}-A_{33}}{A_{33}}$
(x_1, x_3) plane	$\epsilon^{(2)} = \frac{A_{11}-A_{33}}{2A_{33}}$	$\gamma^{(2)} = \frac{A_{66}-A_{44}}{2A_{44}}$	$\delta^{(2)} = \frac{A_{13}+2A_{55}-A_{33}}{A_{33}}$
(x_1, x_2) plane	$\epsilon^{(3)} = \frac{A_{22}-A_{11}}{2A_{11}}$	$\gamma^{(3)} = \frac{A_{44}-A_{55}}{2A_{55}}$	$\delta^{(3)} = \frac{A_{12}+2A_{66}-A_{33}}{A_{33}}$

Vavryčuk and Pšenčik (1998) have derived PP reflection coefficients for weak contrast interfaces separating two weakly but arbitrary anisotropic media using a set of anisotropy parameters different than Rüger (1997) (their anisotropy parameters are linear approximations of the ones used by Rüger). The orthorhombic PP reflection coefficient given by Vavryčuk and Pšenčik (1998) for general weak anisotropy media (their equation 40) can be written as

$$
\begin{aligned}
R_{PP}(\theta,\varphi) &= \left(\frac{1}{2\cos^2\theta}\right)\frac{\Delta\alpha}{\bar{\alpha}} + \left(\frac{4\beta^2}{\alpha^2}\sin^2\theta\right)\frac{\Delta\beta}{\bar{\beta}} + \left(\frac{1}{2} - \frac{2\beta^2}{\alpha^2}\sin^2\theta\right)\frac{\Delta\rho}{\bar{\rho}} \\
&+ \frac{1}{2}\left[\Delta(\frac{A_{13}+2A_{55}-A_{33}}{A_{33}})\cos^2\varphi\right. \\
&+ \left.\left(\Delta(\frac{A_{23}+2A_{44}-A_{33}}{A_{33}}) - 8\Delta(\frac{A_{44}-A_{55}}{2A_{33}})\right)\sin^2\varphi\right]\sin^2\theta \\
&+ \frac{1}{2}\left[\Delta\left(\frac{A_{11}-A_{33}}{2A_{33}}\right)\cos^4\varphi + \Delta\left(\frac{A_{22}-A_{33}}{2A_{33}}\right)\sin^4\varphi\right. \\
&+ \left.\Delta\left(\frac{A_{12}+2A_{66}-A_{33}}{A_{33}}\right)\cos^2\varphi\sin^2\varphi\right]\sin^2\theta\tan^2\theta, \qquad (5.1)
\end{aligned}
$$

where φ is the azimuth angle with the x_1-axis, θ is the incident angle, $\alpha^2 = A_{33}$, and $\beta^2 = A_{55}$. The Thomsen-style anisotropy parameters are not explicitly used in equation 5.1; their anisotropy parameters are combinations of the A_{ij}'s but can be equivalently renamed to the Thomsen-style anisotropy parameters. I renamed their parameters to the orthorhombic anisotropy parameters introduced by Tsvankin (1997). Translating to the Thomsen-style anisotropy parameters using Table 5.1, the orthorhombic PP reflection coefficient becomes

$$
\begin{aligned}
R_{PP}(\theta,\varphi) &= \left(\frac{1}{2\cos^2\theta}\right)\frac{\Delta\alpha}{\bar{\alpha}} \\
&- \left(\frac{4\beta^2}{\alpha^2}\sin^2\theta\right)\frac{\Delta\beta}{\bar{\beta}} \\
&+ \left(\frac{1}{2}-\frac{2\beta^2}{\alpha^2}\sin^2\theta\right)\frac{\Delta\rho}{\bar{\rho}} \\
&+ \left(\frac{1}{2}\cos^2\varphi\sin^2\theta\right)\ \Delta\delta^{(2)} \\
&+ \left(\frac{1}{2}\sin^2\varphi\sin^2\theta\right)\ \Delta\delta^{(1)} \\
&- \left(\frac{4\beta^2}{\alpha^2}\sin^2\varphi\ \sin^2\theta\right)\Delta\gamma \\
&+ \left(\frac{1}{2}\cos^4\varphi\sin^2\theta\ \tan^2\theta\right)\Delta\varepsilon^{(2)} \\
&+ \left(\frac{1}{2}\sin^4\varphi\sin^2\theta\ \tan^2\theta\right)\Delta\varepsilon^{(1)} \\
&+ \left(\frac{1}{2}\cos^2\varphi\sin^2\varphi\sin^2\theta\ \tan^2\theta\right)\Delta\delta^{(3)}. \qquad (5.2)
\end{aligned}
$$

For an HTI medium in a coordinate-system where its symmetry axis coincides with the x_1-axis, $\varepsilon^{(1)} = \delta^{(1)} = 0$, and $\delta^{(3)} = \delta^{(2)}$. Hence, Vavryčuk's orthorhombic PP reflection coefficient (equation 5.2) for a boundary of two HTI media becomes:

$$
\begin{aligned}
R_{PP}^{HTI}(\theta,\varphi) &= \left(\frac{1}{2\cos^2\theta}\right)\frac{\Delta\alpha}{\bar{\alpha}} - \left(\frac{4\beta^2}{\alpha^2}\sin^2\theta\right)\frac{\Delta\beta}{\bar{\beta}} + \left(\frac{1}{2}-\frac{2\beta^2}{\alpha^2}\sin^2\theta\right)\frac{\Delta\rho}{\bar{\rho}} \\
&+ \frac{1}{2}\cos^2\varphi\sin^2\theta\left(1+\sin^2\theta\ \tan^2\theta\right)\ \Delta\delta^{(2)} \\
&- \left(\frac{4\beta^2}{\alpha^2}\sin^2\varphi\ \sin^2\theta\right)\Delta\gamma^{(3)} + \left(\frac{1}{2}\cos^4\varphi\sin^2\theta\ \tan^2\theta\right)\Delta\varepsilon^{(2)}. \qquad (5.3)
\end{aligned}
$$

This expression for the PP reflection coefficient is analytically similar to Rüger's PP reflection coefficient (equation 4.1) for a boundary of two HTI media. The following considerations of equation 5.3 (Vavryčk) and equation 4.1 (Rüger) reveal that these two equations are analytically very similar.

- The Vavryčk anisotropy parameter $\epsilon^{(2)}$ is exactly the same as $\epsilon^{(V)}$ used by Rüger.

- The Vavryčk anisotropy parameter $\delta^{(2)}$, good for weak anisotropy, is the linear approximation to the $\delta^{(V)}$ used by Rüger.
- The Vavryčk anisotropy parameter $\gamma^{(3)}$ is exactly the same as γ used by Rüger.
- The Vavryčk shear-wave velocity $\beta^2 = A_{55}$ corresponds to the vertically propagating S_V-wave in the (x_1, x_3) plane. The Rüger shear-wave velocity $\beta^2 = A_{44}$ corresponds to the vertically propagating S_H-wave in the (x_1, x_3) plane.
- The Vavryčk β is equal to $\beta_{Ruger}(1 - \gamma)$ for weak anisotropy.

By calculating and plotting numerical values, it can be shown that Vavryčk's and Rüger's expressions for the PP reflection coefficient for a boundary separating two HTI media are almost equivalent. The specific example uses the elastic properties of the plexiglas and phenolic material. Figure 5.4 shows the PP reflection coefficient for three azimuths (0°, 45°, 90°).

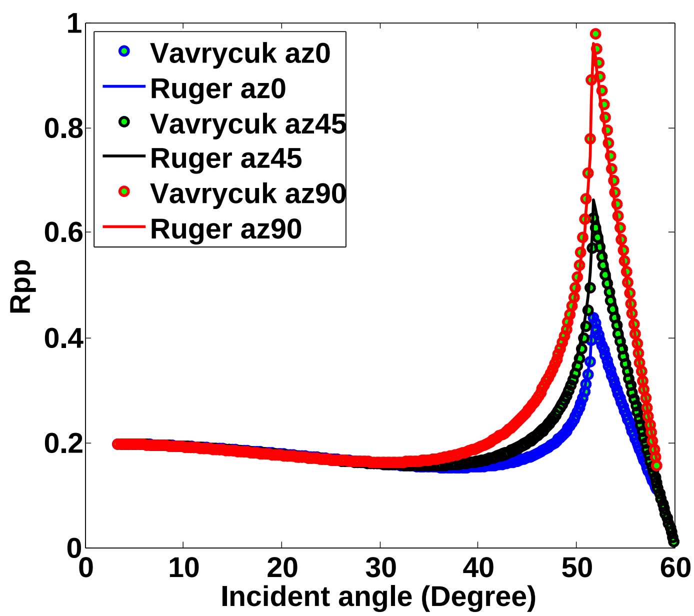

Figure 5.4: Comparison of the results from Rüger's and Vavryčuk's equation for the plexiglas-phenolic interface.

5.2.5 Derivation of anisotropic reflection coefficients from scatting theory

Numerical examples, and many case studies, have shown that Rüger's plane-wave approximation for the PP reflection coefficient are close to the exact reflection response for situations in which the underlying assumptions about the reflecting boundary are satisfied. However, Rüger's is not suitable for analysis of parameters at interfaces with strong anisotropy and large contrasts in the elastic parameters. It is also not valid for the boundary of two HTI layers with differently oriented symmetry axis. For AVO class I, the predicated critical angle versus azimuth, by Rüger's equation, stays the same, in contrast to what has been shown with the physical model reflection data in this thesis in which the critical angle decreases toward the fast direction. Therefore, it is important to establish a physical foundation for better anisotropic reflection coefficient approximations. I believe, the method to derive reflection coefficients by Innanen (2012), using scattering theory, can be extended to develop more accurate anisotropic reflection coefficients.

5.3 Conclusions

Estimates of the elastic parameters have been obtained via the determination of orthorhombic stiffness coefficients using easy-to-measure less-sensitive-to-transducer-size group velocities. The advantage of the proposed method over the conventionally used phase velocities, which are sensitive to transducers size, is shown. The relations between phase velocities and stiffness coefficients are exact, but inaccurate phase velocity measurements from large transducers will introduce larger errors to the estimates than directly using group velocities and approximate expressions relating them to the group velocities.

Using deterministic amplitude corrections, the suitability of 3D physical model reflection data for a quantitative amplitude analysis have been confirmed, by showing that reflection coefficients derived theoretically are in a good agreement.

Incorporating wide-angle data is essential for accurate estimates for anisotropy parameters of a fractured medium. The most important one, the shear-wave splitting parameter, can be estimated from azimuthal amplitude variations. The six-parameter AVAZ inversion estimates demonstrate that Rüger's equation is suitable for quantitative amplitude analysis of anisotropic targets, and can be employed for numerical inversion algorithms.

The estimated fracture orientation from AVAZ inversion has an inherent ambiguity, as it predicts both the fracture orientation and the direction normal to it. For an AVO class I situation, the information about the critical angle can provide the accurate fracture orientation direction.

Appendix A

Anellipsoidal deviation terms

This appendix provides the basis on how the E_{ij} terms in theory section can be interpreted as deviation, from elliptical anisotropy terms. Lets start with the definition of a velocity surface, plotting the phase/group velocity of a given mode (qP-, qS-waves) as the radius-vector in all directions. The group velocity surface, therefore, is the wavefront at unit time. An orthorhombic medium has ellipsoidal anisotropy, if the wavefront, and hence the group velocity surface, is an ellipsoid, then, the formula for group velocity surface is that of an ellipsoid. The qP ellipsoidal group velocity surface, then, has the exact form

$$\frac{1}{V^2(\vec{N})} = \frac{N_1^2}{A_{11}} + \frac{N_2^2}{A_{22}} + \frac{N_3^2}{A_{33}}, \tag{A.1}$$

and the corresponding phase velocity has the form (Musgrave (1970), equations 8.2.1 and 8.2.2b page 96)

$$v^2(\vec{n}) = A_{11}n_1^2 + A_{22}n_2^2 + A_{33}n_3^2, \tag{A.2}$$

where $\vec{n} = (n_1, n_2, n_3) = (sin\theta cos\phi, sin\theta sin\phi, cos\theta)$ is the unit vector normal to the wavefront, with θ and ϕ having similar definitions as Θ and Φ.

For a general weakly anisotropic medium, the first-order linearized approximation for qP phase velocity is $\rho v^2(\vec{n}) \simeq c_{ijkl}n_in_jn_kn_l$, (Backus, 1965). Defining the density-normalized stiffness tensor as $a_{ijkl} = c_{ijkl}/\rho$, it reads

$$v^2(\vec{n}) \simeq a_{ijkl}n_in_jn_kn_l. \tag{A.3}$$

Using Voigt notation for indexes ($11 \to 1, 22 \to 2, 33 \to 3, 23 \to 4, 13 \to 5, 12 \to 6$), the density-normalized stiffness coefficients A_{ij} will be obtained as $a_{ijkl} = A_{mn}$. Expanding equation A.3 for orthorhombic symmetry one obtains

$$\begin{aligned} v^2(\vec{n}) \simeq\ & A_{11}n_1^4 + A_{22}n_2^4 + A_{33}n_3^4 + 2(A_{12} + 2A_{66})n_1^2n_2^2 + \\ & 2(A_{13} + 2A_{55})n_1^2n_3^2 + 2(A_{23} + 2A_{44})n_2^2n_3^2. \end{aligned} \tag{A.4}$$

Equation A.4 can be modified to read (Daley and Krebes, 2006),

$$\begin{aligned} v^2(\vec{n}) \simeq\ & A_{11}n_1^2 + A_{22}n_2^2 + A_{33}n_3^2 + \\ & E_{23}n_2^2n_3^2 + E_{13}n_1^2n_3^2 + E_{12}n_1^2n_2^2. \end{aligned} \tag{A.5}$$

where the quantities E_{ij} were perviously defined. Equation A.5 is an expression for orthorhombic phase velocity in an approximate form. Comparing it with the ellipsoidal phase velocity (equation A.2), we interpret the E_{ij} as anellipsoidal deviation terms. Helbig (1983) states, that in the study of transverse isotropy by Rudzki (1911), the wavefront for the compressional wave in the (x_1, x_3) plane is ellipsoidal if and only if $(A_{11} - A_{55})(A_{33} - A_{55}) - (A_{13} + A_{55})^2 = 0$. The E_{13} deviation term in equation 2.6 is a linearized approximation of this deviation term used by Rudzki (1911).

Appendix B

Numerical tests of the group velocity expression

The approximate qP group velocity, equation 2.5 is generally in good agreement with the exact calculations, even for highly anisotropic media. For weakly anellipsoidal anisotropic media which group velocity singularity does not appear, the group velocity approximation was bench marked against the exact solution and found to be very accurate (Daley and Krebes, 2006). In addition, it was compared to the approximation presented in Pšenčík and Farra (2005). The results were equivalent; about $0.2\% - 0.3\%$ deviation from exact traveltime calculations for weakly anisotropic media and 2% for a highly anisotropic (olivine) medium. Song and Every (2000) numerically validated equation 2.5, and showed that this formula can accurately account for the non-ellipticity of the qP group velocity surface in the absence of cusps.

Here the validity of the proposed inversion for off-diagonal terms are tested for two numerical examples. Using transmission traveltimes along various directions, generated from an anisotropic ray-tracing code, I calculated the group velocities (similar to the way presented next, just assuming point sources and receivers). The first example, I use the A_{ij} of Greenhorn shale (Sayers and Ebrom, 1997), classified as weakly transversely isotropic. The stiffness coefficients for this model are $A_{11} = A_{22} = 19.19$, $A_{33} = 15.65$, $A_{13} = A_{23} = 7.06$, $A_{12} = 7.79$, $A_{44} = A_{55} = 4.11$, and $A_{66} = 5.7$ where all the A_{ij} have the units of $(\mathrm{km/s})^2$. The estimated value of A_{13} is to within 1.2% accurate. The second example is olivine, an orthorhombic medium with strong anisotropy. Its density-normalized stiffness coefficients are $A_{11} = 9.779$, $A_{33} = 7.103$, $A_{13} = 2.163$, $A_{44} = 2.358$, and $A_{66} = 5.7$. Olivine's qP group velocity surface, in the (x_1, x_3) symmetry plane, is highly anisotropic. In this case, the proposed inversion for A_{13} resulted in a 2.3% error.

For the above weak and strong anisotropic examples, the proposed inversion for off-diagonal A_{ij}s are highly accurate. Of course, this accuracy is highly dependent on the accuracy of the independently estimated diagonal A_{ii}, which in this case were assumed known without error.

Appendix C

Exact orthorhombic phase velocity expressions

Tsvankin (1997) presented the exact orthorhombic phase velocity expressions for the symmetry planes. For propagation in the (x_1, x_3) symmetry plane, the exact qS$_H$ phase velocity is

$$v_{S_H}(\theta)^2 = A_{66}\sin^2\theta + A_{44}\cos^2\theta, \tag{C.1}$$

where θ is the phase angle with the x_3-axis. The exact phase velocity of the qP and qS$_V$ modes are

$$\begin{aligned} 2v^2(\theta) &= (A_{11}+A_{55})\sin^2\theta + (A_{33}+A_{55})\cos^2\theta \qquad \text{(C.2)} \\ &\pm \sqrt{\left[(A_{11}-A_{55})\sin^2\theta - (A_{33}-A_{55})\cos^2\theta\right]^2 + 4(A_{13}+A_{55})^2\sin^2\theta\cos^2\theta}, \end{aligned}$$

where the plus and minus signs correspond to the qP and qS$_V$ modes of propagation, respectively. For the propagation in other symmetry planes, the appropriate indexes are used.

For the orthorhombic symmetry planes, the group velocity and group angle, of three wave modes, are related to the phase velocity by (Berryman, 1979)

$$V_G = v(\theta)\sqrt{1+\left(\frac{1}{v(\theta)}\frac{dv(\theta)}{d\theta}\right)}, \tag{C.3}$$

$$\tan\psi = \frac{\tan\theta + \frac{1}{v(\theta)}\frac{dv(\theta)}{d\theta}}{1-\frac{\tan\theta}{v(\theta)}\frac{dv(\theta)}{d\theta}}, \tag{C.4}$$

where V_G is the magnitude of the group angle, ψ is the group angle, v is phase velocity, and θ is the phase angle.

Appendix D

Initial source-receiver offset determination

In this appendix, two practical ways to estimate the first source-receiver offset for a physical model data are presented.

D.0.1 Initial offset: manual positioning

Consider a Cartesian coordinate system for collecting a seismic gather along the x-axis. Establish an origin on your solid model. Have your both transducers touching the first solid layer. Require that both source and receiver transducer are in contact with the first solid layer. Manually move source transducer to the marked origin and reset the positioning system for the source-arm to have this point as the origin. Use the automatic positioning system to move the x-coordinate of the source transducer back -10mm. Manually move the receiver transducer to the marked reference point, and again reset the positioning system for the receiver-arm to this point. Now, nominally both source and receiver transducers have the same origin which might not be very accurate as it is set visually. Using the automatic positioning system, move the z-coordinates on both source and receiver transducers to a certain depth in water. The first-arrival traveltime (the direct arrival though the water between the transducers) should give a value of 6.73μs (0.01 (m)/1485 (m/s) = 6.73μs) as the transducers are 10mm apart. Use the automatic positioning system to move receiver transducer slightly until the first-arrival traveltime of 6.73μs is achieved. The location of the receiver transducer gives a 6.73μs traveltime is the origin. Reset the x-coordinate of your receiver transducer again to this present location. This sets the first source-receiver offset to the value of 10mm accurately within the precision of the positioning system. An approach to estimate the first source-receiver directly from reflection data is given next.

D.0.2 Initial offset: estimate from common-shot gather data

In a shot gather, consider the first-arrival traveltimes, a linear event propagating with the first-layer P-wave velocity, as

$$ax + b = t, \tag{D.1}$$

where t are the first-arrival traveltimes, and x is the receiver location. The constant a can be interpreted as the slowness of the first-layer, and $-b/a$ is the first source-receiver offset. The constants a and b can be obtained from the least-square fitting of the first-arrival traveltimes. Using equation D.1, the (x, t) picks of the first-arrival event can be used in a linear system of equations,

$$\begin{pmatrix} x_1 & 1 \\ \vdots & \\ x_n & 1 \end{pmatrix} \begin{pmatrix} a \\ b \end{pmatrix} = \begin{pmatrix} t_1 \\ \vdots \\ t_n \end{pmatrix} \tag{D.2}$$

where n is the number of the picks. A least-squares solution of system of equations D.2 gives an estimate of the slowness of the first layer as well as the first source-receiver offset. If the (x, t) data are from a water layer, the slowness value should be equal to $(1485\text{m/s})^{-1}$

Appendix E

Single-leg ghost event

The traveltime of a single-leg ghost event generated due to the presence of a free-surface is examined in this appendix. I show that a single-leg ghost has the same reflection traveltime as that of a wave generated and recorded at the water contact with the transducers.

Assume a virtual wave propagation in which the wave is generated and recorded at water contact with the source and receiver transducers (see Figure E.1a). The traveltime of this event is

$$tt = \frac{2\sqrt{\frac{x^2}{4} + d^2}}{V_w}, \tag{E.1}$$

where x is the source-receiver offset, V_w is the P-velocity of water, and d is the reflector depth. With a source-receiver offset $x/2 = d\tan\theta$, where θ is the incident angle at the CMP between the source and receiver, equation E.1 becomes

$$\begin{aligned} tt &= \frac{2\sqrt{d^2\tan^2\theta + d^2}}{V_w}, \\ tt &= \frac{2d}{V_w\cos\theta}. \end{aligned} \tag{E.2}$$

Now assume a single-leg ghost at the receiver, see Figure E.1b. With the notation used in Figure E.1b, $x/2 = x_1 + x_2$, $x_1 = d_1\tan\theta_a$, $x_2 = d_2\tan\theta_a$ and $d = d_1 + d_2$. Designate the traveltime related to this single-leg ghost as t_a,

$$\begin{aligned} t_a &= \frac{2\sqrt{x_1^2 + d_1^2}}{V_w} + \frac{2\sqrt{x_2^2 + d_2^2}}{V_w}, \\ t_a &= \frac{2d_1}{V_w\cos\theta} + \frac{2d_2}{V_w\cos\theta}, \\ t_a &= \frac{2(d_1 + d_2)}{V_w\cos\theta}, \\ t_a &= \frac{2d}{V_w\cos\theta}, \end{aligned} \tag{E.3}$$

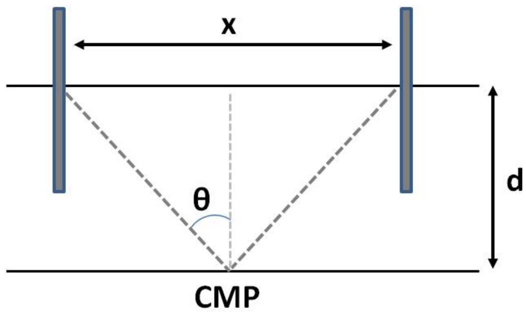

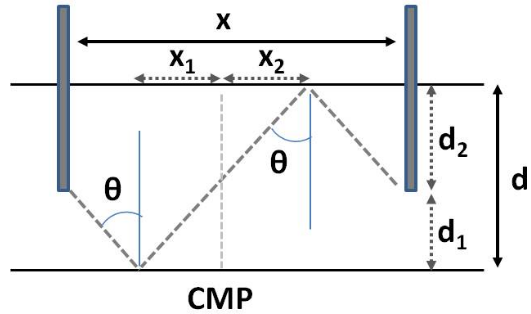

Figure E.1: (a) Raypath of the virtual wave propagation in which the wave is generated and recorded at water contact. (b) Raypath of a single-leg ghost.

Then comparing t_a with equation E.2 it may be seen that $tt = t_a$. This means the traveltime of the single-leg ghost event is equal to the traveltime of a wave generated and recorded at the water contact with the transducers. Therefore, the single-leg ghost event has a constant traveltime independent of the source and receiver transducers' tip depth within the water, provide both reach the same depth.

Appendix F

AVO corrections for subsurface factors

This appendix details about the AVO corrections for the subsurface effects applied to the reflection amplitudes from water-plexiglas and plexiglas-phenolic interfaces, as well as some simple instructions for the corrections of field datasets.

F.0.3 Geometrical spreading

As seismic energy propagates away from a source, the total energy of the wavefront surface remains the same. As the wavefront becomes larger the energy per unit area becomes smaller, and consequently the amplitudes become weaker. This amplitude decay is a geometrical effect. For a single homogeneous layers consider a seismic ray with amplitude A_1, after traveling a raypath of length L its amplitude will be A_1/L, so the geometrical spreading factor is L. For multiple layers, in addition to the raypath length, the confined area in a ray tube after reflection or transmission from each layer should also be taken into account. For plane parallel homogeneous layers, the raypaths are composed of straight line segments. For a given offset and target depth, the geometrical spreading factor is given as (Červený and Ravindra, 1971)

$$D_g(x) = \frac{\cos\theta_s}{v_s}\sqrt{\left(\sum_{j=1}^{k}\frac{h_j v_j}{\cos\theta_j}\right)\left(\sum_{j=1}^{k}\frac{h_j v_j}{\cos^3\theta_j}\right)} \tag{F.1}$$

where h_j and v_j are the thickness and velocity of the layer containing to the j^{th} ray segment, and θ_j is the angle the j^{th} ray segment makes with the vertical axis. Knowing the velocity of water and plexiglas, this provides the exact geometrical spreading correction ($D_g(x)$ in equation 3.1) for horizontal layering which is applied to the physical model reflection amplitudes.

For field data, which lacks details about the overburden layers, exact velocities, such an exact geometrical spreading correction is often not possible. However, there are readily applied zero-offset and offset-dependent geometrical spreading corrections that can be applied to shot gather (or CMP gather) data before move-out is applied. The zero-offset geometrical spreading correction is (Newman, 1973; Resnik, 1993)

$$g_0(t) = V_{rms}^2(t_0)t, \tag{F.2}$$

where t is the two way traveltime and V_{rms} is an estimate of the root-mean-square (rms) velocity at the corresponding zero-offset time, t_0. A single velocity function is used for the entire gather, meaning it does not change at each offset. This provides a good approximate correction, but does not fully compensate for spreading effect at far offsets. An offset-dependent geometrical spreading correction given by Ursin (1990) is

$$g_1^2(t,x) = g_0^2(t) + \left[2\left(\frac{V_{rms}}{V_1}\right)^2 - 1\right]x^2 + \frac{1}{{t_0}^2}\left(\frac{1}{V_1^2} - \frac{1}{V_{rms}^2}\right)x^4, \tag{F.3}$$

where x is the source-receiver offset, and V_1 is the first layer velocity. Figure F.1 shows the water-plexiglas reflector amplitudes versus incident angle that have been corrected for geometrical spreading using corrections by raytracing, zero-offset, and offset-dependent geometrical spreading. The offset-dependent correction compensates nearly as well as the raytracing geometrical spreading correction (equation F.1).

F.0.4 Transmission loss

The Zoeppritz equations can provide the downgoing PP transmission coefficient, $T_{j,j+1}(\theta_j)$, and upgoing PP transmission coefficient, $T_{j+1,j}(\theta_{j+1})$, between layers j and $j+1$. The decrease in amplitude associated with transmission loss between layer j and $j+1$ is the product $T_{j,j+1}(\theta_j) \times T_{j+1,j}(\theta_{j+1})$. The transmission loss factor, $L(x)$ in equation 3.1, is the total loss for all interfaces along the entire raypath (e.g. Duren, 1991; Spratt et al.,

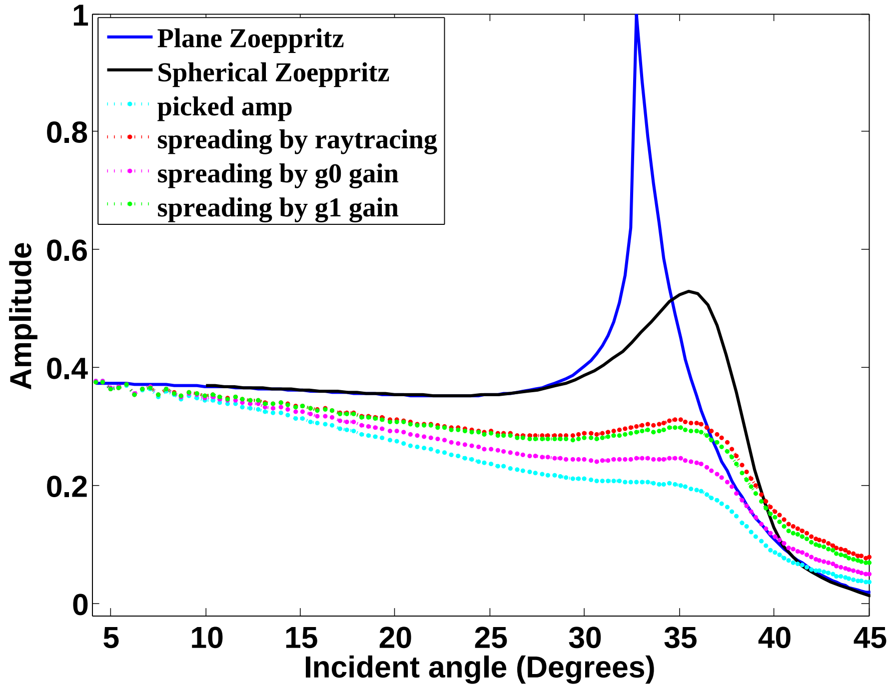

Figure F.1: Geometrical spreading corrections (raytracing, zero-offset, and offset-dependent) applied to the water-plexiglas reflection amplitudes. The amplitudes have been compared to Zoeppritz predicated reflection coefficients.

1993):

$$L(x) = \prod_{j=1}^{k-1} T_{j,j+1}(\theta_j) T_{j+1,j}(\theta_{j+1}). \tag{F.4}$$

For field data, a deterministic correction of transmission loss is problematic as the overburden can not be perfectly characterized. Transmission loss is the most significant problem encountered in AVO analysis (Gassaway, 1984). In practice the transmission loss is compensated for using statistical corrections.

F.0.5 Emergence angle

For vertical component data, the recordings should be converted to total motion for amplitude data to represent reflection coefficients. Knowing the emergence angle (θ_h) at the receiver location, the factor $\cos(\theta_h)$ (equation 3.1) provides the total motion and is called emergence angle correction in this thesis.

F.0.6 Scalar factor

After applying all subsurface and surface corrections, a constant scalar factor is required to normalized the amplitude magnitude to the range of $[-1, 1]$, the reflection coefficient range. This scalar factor is the S term in equation 3.1. The single scalar factor is applied to the entire seismic gather and is related mostly to the source strength and some possible power filters applied in processing.

For the reflection amplitudes from an individual reflector (e.g., amplitudes reflected from the water-plexiglas interface), the scalar factor can be determined by calibrating the near-offset amplitudes to the normal incident reflection coefficient from the Zoeppritz equations. At each incident angle, call the Zoeppritz reflection coefficient $A_Z(\theta)$, and the raw picked amplitudes $A(\theta)$. Then the scalar factor can be calculated as

$$S = \frac{A_Z(\theta \simeq 0)}{average A(\theta_1 : \theta_n)}, \tag{F.5}$$

where $A(\theta_1 : \theta_n)$ refers to the near-offset amplitudes (e.g., $\theta_n < 10°$). The examined amplitudes in Chapter 3, after each corrections, have been normalized using equation F.5.

Finding the scaler for a shot gather, consider the time window around your target event, the scalar factor can be obtained by minimizing $A(x_0, t) - SR(t)$ in a least-squares sense, where $A(x_0, t)$ are the near-offset amplitudes and $R(t)$ is the reflectivity model defined by well logs or a velocity model. Minimizing

$$b = \sum_{k=1}^{\max} (A_k - SR_k)^2, \tag{F.6}$$

means

$$\frac{\partial b}{\partial S} = \sum_k -2R_k (A_k - SR_k) = 0, \tag{F.7}$$

and the scalar becomes (Margrave, 2000):

$$S = \frac{\sum_k R_k A_k}{\sum_k R_k R_k}, \tag{F.8}$$

where $\sum_k R_k A_k$ is the zero-lag cross-correlation of $R(t)$ and $A(t)$, and $\sum_k R_k R_k$ is the zero-lag autocorrelation of $R(t)$.

Appendix G

Radial trace filtering the physical model data

The radial trace (RT) transform is a seismic data mapping algorithm, developed to attenuate coherent noise in seismic data. This appendix follows Henley (2003) in describing briefly the principles of the method, and its application in processing physical model reflection data.

G.1 The RT transfrom

The RT transform maps seismic amplitudes from coordinates of source-receiver offset and traveltime, $S(x, t)$, to coordinates of apparent velocity and traveltime, $\widehat{S}(v, T)$, with no change to amplitudes. Using a fan of common-origin linear trajectories in the (x, t) domain (a set of constant-apparent-velocity dips), the amplitude values from the (x, t) panel are mapped into a (v, t) panel (Figure G.1a). Each trace in the RT domain consists of amplitude values selected from the (x, t) domain along a linear trajectory of constant apparent velocity, v, where v becomes the trace identifier in the RT domain. Each radial trace has the same traveltime coordinate and sample increment as the original (x, t) data (Figure G.1a). Since the RT transform is a non-uniform mapping, interpolation is required to obtain samples in the RT domain which fall between two traces along a trajectory in the (x, t) domain. Every interpolation involves only one sample, at the same traveltime, from each of the two nearest traces. Depending upon the particular interpolation used, the RT transform can be inverted very accurately (similar to NMO, which is also a non-uniform mapping transform).

Linear events in the (x, t) domain which align with the trajectories of the RT trans-

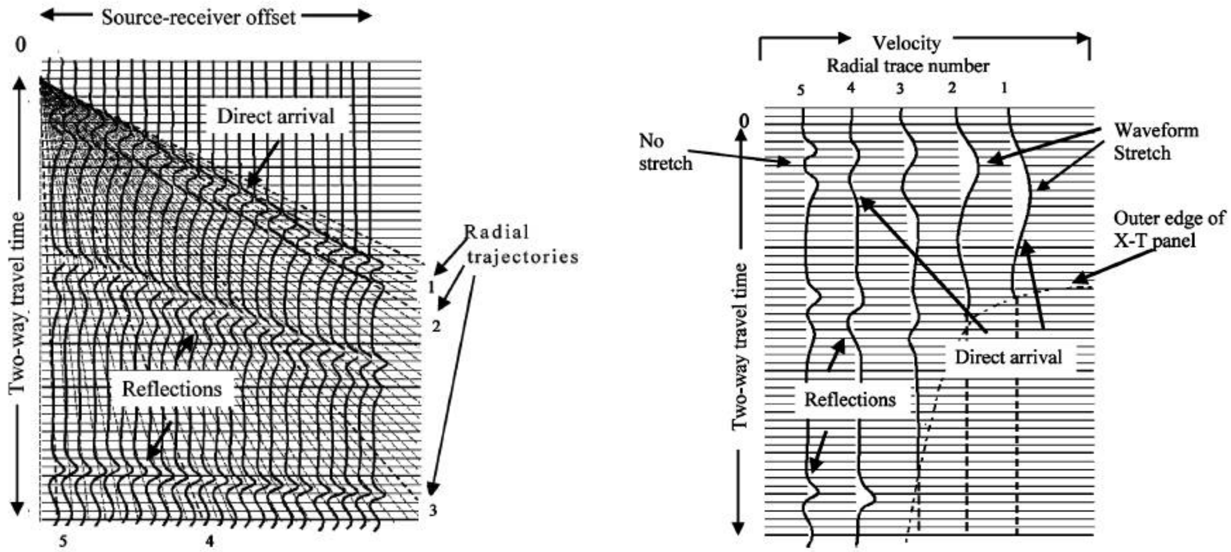

(a) (x, t) domain

(b) (x, t) domain

Figure G.1: Mapping of seismic traces from the (x, t) domain to the (R, T) domain. (a) Seismic gather with constant velocity trajectories. (b) Radial traces. Because the high--velocity trajectories encounter the linear events on the (x, t) panel very nearly parallel to their wavefronts, these linear events become low-frequency events on the corresponding radial traces (Henley, 2003).

form are rotated by the transform to low-frequency vertical events, thus providing the separation from reflection events required for successful attenuation. Because their RT domain bandwidth is usually well below the bandwidth of legitimate reflection events, linear noise events can be filtered in the RT domain either by applying a low-cut filter, which passes reflection energy while rejecting linear noise, or by applying a low-pass filter, which passes only the linear noise. The RT domain noise estimate can then be transformed back to the (x, t) domain and subtracted from the original (x, t) panel (preferred). By choosing the origin coordinates and apparent velocity range of the RT transform to best overlay targeted linear events on the (x, t) panel, noise estimation and attenuation are maximized. When not all linear events project to a common origin, several subsequent filter passes, using parameters which help the RT transform align with particular events, can be very effective.

G.2 Attenuating the linear events in the physical model data

For the physical model data, multiple RT filtering is applied to suppress all linear events intercepting the event of interest. First, the hyperbolic event of interest has flattened by normal-move-out (NMO) removal correction (Figure G.2). Consequently, the unwanted interferening events appear as a family of linear events with some residual slope crossing the event of interest (Figure G.2a); multiple RT filters are then applied, with each designed to subtract events with a particular slope. Figure G.2a shows the plexiglas-phenolic reflector (Chapter 3) flattened with all the interfering events clearly appear with intercepting slopes. Figure G.2b shows the plexiglas reflector after several passes of radial filtering. While interfering events have been attenuated adequately for the large offsets, the RT filtering was unable to attenuate the very small offset interfering event. At very small offsets, there is very little move-out discrimination between the event of interest and the interfering event. The interfering event has been nearly flattened as the event of interest itself. For the further offsets, distinguishable interfering events with different dips were removed easily.

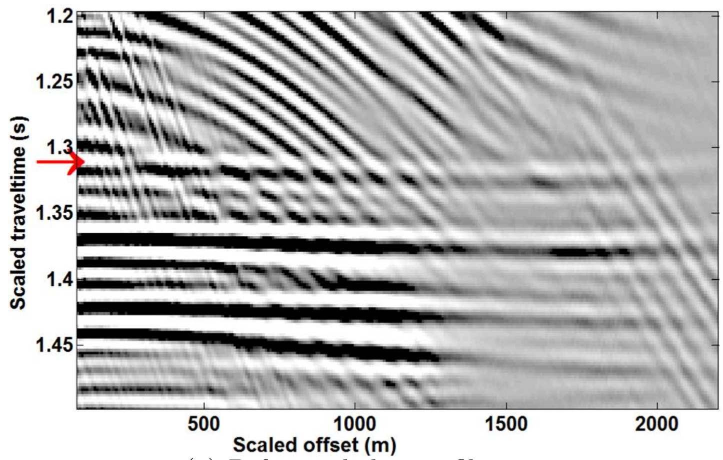

(a) Before radial trace filtering

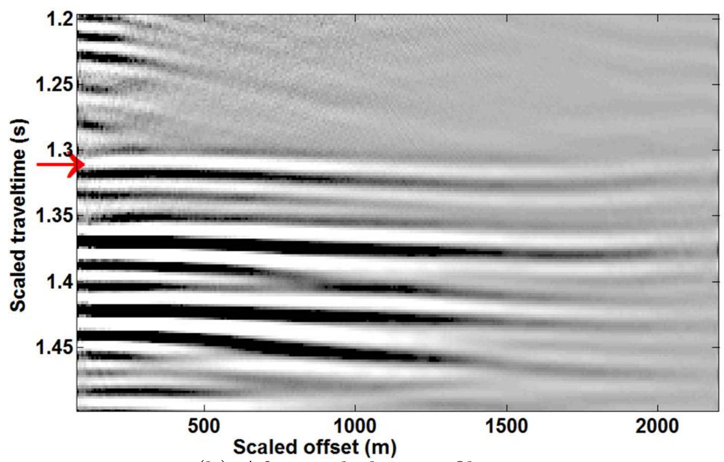

(b) After radial trace filtering

Figure G.2: Plexiglas-phenolic reflector along azimuth 0° (Chapter3), NMO removed. Note the interference events crossing the target event.

Appendix H

Singular value decomposition

Singular value decomposition, SVD, is a common and precise way of solving linear least-squares problems Sheriff (1991). Consider the matrix equation

$$G_{nm}m_{m1} = D_{n1}. \tag{H.1}$$

For the matrix G of order nm, a mapping from the model space $S(m)$ to the data space $S(D)$, there is always a matrix decomposition called the singular value decomposition (SVD) of matrix G. SVD allows the matrix G to be expressed as the product of the matrices (Lay, 1996),

$$G = U\Lambda V^T, \tag{H.2}$$

where U is the matrix of eigenvectors of GG^T that span the data space, and V is the matrix of eigenvectors of G^TG that span the model space. The singular values of the matrix G are the positive square roots of the eigenvalues of the matrix G^TG. Λ is a diagonal matrix with the singular values of the matrix G in the diagonal elements in a decreasing order. The SVD of matrix G can be written as (Menke, 1985)

$$G = U\Lambda V^T = U_p\Lambda_p V_p^T \tag{H.3}$$

where U_p and V_p consist of the first p columns of U and V, related to non-zero singular values.

The SVD of matrix G always exists due to the existence of the matrices U and V (Lay, 1996). Since the diagonal entries in matrix Λ_p are nonzero, the generalized inverse, also called the Lanczos inverse of matrix G, is defined as (Lay, 1996)

$$G_g^{-1} = V_p\Lambda^{-1}U_p^T = V_p\left[diag\left(\frac{1}{\sigma_p}\right)\right]U_p^T. \tag{H.4}$$

For the generalized inverse matrix, the following holds:

$$G_g^{-1}GG_g^{-1} = G_g^{-1}, \tag{H.5}$$

$$GG_g^{-1}G = G. \tag{H.6}$$

Applying the generalized matrix G_g^{-1} to both sides of equation H.1,

$$G_g^{-1}Gm = G_g^{-1}D. \tag{H.7}$$

From equation H.5, equation H.7 becomes $G_g^{-1}Gm = G_g^{-1}GG_g^{-1}D$. Then the estimated solution m_{est} becomes

$$m_{est} = G_g^{-1}D. \tag{H.8}$$

Substituting equation H.1 for D, equation H.8 transforms into (Menke, 1985)

$$m_{est} = G_g^{-1}Gm. \tag{H.9}$$

The matrix $G_g^{-1}G$ is called the model resolution matrix. The model resolution matrix defines how well the estimated solution, m_{est}, resolves the true solution, m. For a perfect resolution, the resolution matrix will be the identity matrix. The diagonal elements of a resolution matrix are good measures of the model resolution. The non-unit diagonal elements imply that the estimates are linear combinations of the true values.

Appendix I

Failed experiment setup

The 3D physical model reflection data presented in this thesis successfully comply with the elastic Zoeppritz theory. The date of this acquisition was 15 March 2013. The start of the journey to get this dataset goes back to April 2011, when a 3D common-shot-gather was acquired over a four-layered model consisting of: water, plexiglas, phenolic layer, and water (Figure I.1). The solid surfaces were not machined and were attached together by having a thin layer of vaseline between them. From this dataset, the raw reflection amplitudes from the plexiglas-phenolic interface (Figure I.2) showed some small- and long-wavelength variations. This was due to the fact that the reflection amplitudes were from various mid-points, and since the two solid interfaces were rough with slight undulations, the mid-points were not exactly the same. For horizontal layering, a common-shot-gather is equivalent to a CMP gather, but the unevenness of the solid layers obviate this assumption. After applying the amplitude corrections (I was not aware of the directivity effect of the transducers at that point), the corrected amplitudes still showed a larger drop than was anticipated.

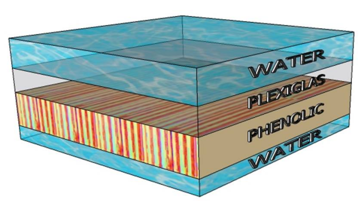

Figure I.1: First try, the four-layered earth model used in the acquisition.

To avoid the effect of unevenness of the solid surfaces on the recorded seismic data, a CMP gather over the four-layered model was collected at September 2011. In a CMP gather all reflections are related to a single subsurface point. Any overlapping of the pri-

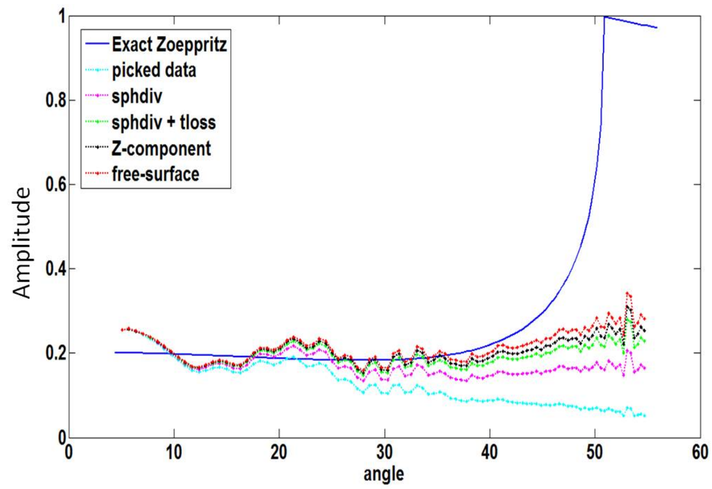

Figure I.2: The amplitudes from plexiglas-phenolic reflector from common-shot-gather dataset.

mary and ghost events were avoided this time. Again none of the reflection amplitudes from the two reflectors (water-plexiglas and plexiglas-phenolic) agreed with the theory. After realizing the directivity effect of the transducers and applying the directivity correction, the water-plexiglas reflection amplitudes were following the theory. This was only true for the water-plexiglas amplitudes picked from the primary event. The amplitudes picked from primary and ghost events showed different trends (Figure I.3). The directivity correction applied in Chapter 3 only works for the primary event, because the physical model transducers only behaves according to the theory presented in section 3.3.2 if the emitted waveforms travel downward into the medium. These transducers are damped so that they do not pass the energy upward. Since for a ghost event energy travels upward from the source and then is reflected at the free-surface, the mentioned directivity correction does not work. So for the plexiglas-phenolic reflector the only choice was to pick on the primary event. But the primary event from the plexiglas-phenolic interface was masked by the wave interferences from top reflectors. Ignoring these wave interferences, appearing as large jitters in the recorded amplitudes, the overall trend of the amplitudes versus the incident angle was lower than was predicted from the theory (Figure I.4). The only possible explanation left was that the plexiglas and phenolic layers were not welded together as was required by the Zoeppritz equations. Therefore, another dataset had to be collected after eliminating the non-welded contact boundary.

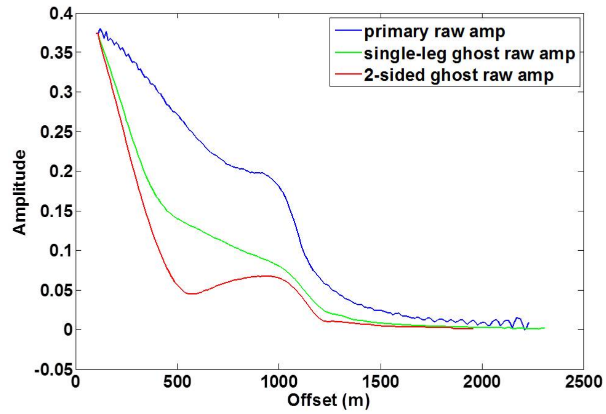

Figure I.3: The water-plexiglas reflection amplitudes, picked from primary, two-sided ghost and one-sided ghost events.

Two plexiglas blocks and the phenolic layer were sent to the workshop to be machined, to ensure flat, smooth interfaces, and to be glued together with epoxy. The model came back to the physical modeling lab, with the epoxy being thick (thickness of around 1mm) causing to appear as a separate reflector in the seismic data. Next, the solid layers were glued together with a thin layer of melted wax [1] under a high pressure to ensure welded contact boundaries. The result was the physical model data presented in Chapter 3, which successfully agreed with the elastic Zoeppritz theory. Now, in addition to this good 3D physical model reflection dataset, CREWES has an example of a perfect physical model reflection dataset of a non-welded interface.

[1]You probably don't want to know, it was Persian leg wax.

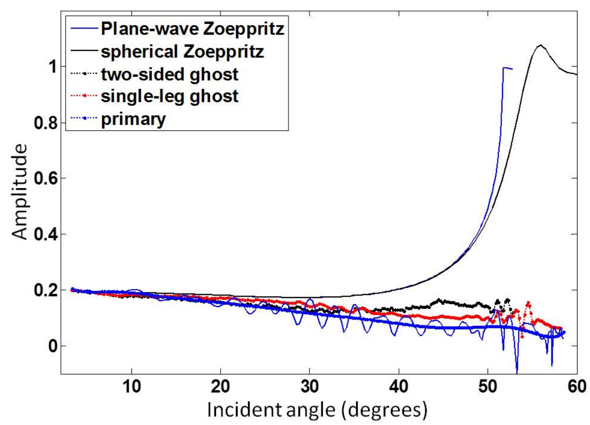

Figure I.4: The corrected plexiglas-phenolic reflection amplitudes, picked from primary, two-sided ghost and one-sided ghost events. The ghost events received a directivity correction based on the above reflector (water-plexiglas). A polynomial has been fitted to the primary event (in blue color), just to see the overall trend.

Bibliography

Aguilera, R., 2003, Geologic and Engineering Aspects of Naturally Fractured Reservoirs: Canadian Society of Exploration Geophysicists Recorder, 44–49.

Aki, K., and Richards, P. G., 1980, Quantitative Seismology: W. H. Freeman and Company, San Francisco.

Alhussain, M., Gurevich, B., and Urosevic, M., 2008, Experimental verification of spherical-wave effect on the AVO response and implications for three-term inversion: Geophysics, **73**, No. 2, C7–C12.

Backus, G. E., 1965, Possible forms of seismic anisotropy of the uppermost mantle under oceans: Journal of Geophysical Research, **70**, No. 14, 3429–3439.

Bale, R. A., 2006, Elastic Wave-equation Depth Migration of Seismic Data for Isotropic and Azimuthally Anisotropic Media: University of Calgary, PhD. Thesis.

Berryman, J. G., 1979, Long-wave elastic anisotropy in transversely isotropic media: Geophysics, **44**, No. 5, 896–917.

Bleistein, N., Cohen, J. K., and Stockwell, J. W. J., 2001, Mathematics of Multidimensional Seismic Imaging, Migration, and Inversion: Springer Science + Business Media, LLC.

Bouzidi, Y., and Schmitt, D. R., 2009, Measurement of the speed and attenuation of the Biot slow wave using a large ultrasonic transmitter: Journal of Geophysical Research, **114**, No. B08201.

Brown, R. J., Lawton, D. C., and Cheadle, S. P., 1991, Scaled physical modeling of anisotropic wave propagation: multioffset profiles over an orthorhombic medium: Geophysical Journal International, **107**, No. 3, 693–702.

Buddensiek, M. L., Krawczyk, C. C. M., Kukowski, N., and Oncken, O., 2009, Performance of piezoelectric transducers in terms of amplitude and waveform: Geophysics, **74**, No. 2, 33–45.

Castagna, J. P., and Backus, M. M., 1993, Offset-dependent reflectivity - theory and practice of AVO analysis: Society of Exploration Geophysicists, Tulsa, OK.

Chang, C., and Gardner, G. H. F., 1997, Effects of vertically aligned fractures on seismic reflections: A physical model study: Geophysics, **62**, No. 1, 245–252.

Cheadle, S. P., Brown, R. J., and Lawton, D. C., 1991, Orthorhombic anisotropy:a physical seismic modeling study: Geophysics, **56**, No. 10, 1603–1613.

Chen, M., and Hilterman, F., 2007, Data correction and anisotropy examination of a physical model with vertically aligned fractures: SEG Expanded Abstracts.

Crampin, S., 1981, A review of wave motion in anisotropic and cracked elastic media: Wave Motion, **3**, 343–391.

Daley, P. F., and Hron, F., 1977, Reflection and transmission coeffcients for transversely isotropic media: Bulletin of the Seismological Society of America, **67**, No. 3, 661–675.

Daley, P. F., and Krebes, E. S., 2006, Quasi- compressional group velocity approximation in a weakly anisotropic orthorhombic medium: Journal of Seismic Exploration, **14**, 319–334.

Daley, P. F., and Krebes, E. S., 2007, Quasi-compressinal group velocity approximation in a general 21-parameter weakly anisotropy medium: Journal of Seismic Exploration, **16**, 41–55.

Dellinger, J., and Vernik, L., 1994, Do traveltimes in pulse-transmission experiments yield anisotropic group or phase velocities?: Geophysics, **59**, No. 11, 1774–1779.

Downton, J. E., 2005, Seismic parameter estimation from avo inversion: University of Calgary, PhD. Thesis.

Duren, R. E., 1988, A theory for marine source arrays: Geophysics, **53**, No. 5, 650–658.

Duren, R. E., 1991, Seismic range equation: Geophysics, **56**, No. 7, 1015–1026.

Duren, R. E., 1992, Seismic range equation: Geophysics, **57**, No. 9, 1203–1208.

Ebrom, D. A., and McDonald, J. A., 1994, Seismic physical modeling: Geophysics Reprint Series: Society of Exploration Geophysicists, Tulsa, OK.

Enkanem, A. M., Wei, J., Wang, S., Di, B., Li, X., and Chapman, M., 2009, Fracture detection using 2D wave seismic data: A seismic physical modeling study: SEG Expanded Abstracts.

Every, A. G., and Sachse, W., 1992, Sensitivity of inversion algorithms for recovering elastic constants of anisotropic solids from longitudinal wavespeed data: Ultrasonics, **30**, No. 1, 43–48.

Gassaway, G. S., 1984, Effects of shallow reflectors on amplitude versus offset (seismic lithology) analysis: SEG Expanded Abstracts, 665–669.

Gray, F., Roberts, G., and Head, K., 2002, Recent advances in determination of fracture strike and crack density from P-wave seismic data: The Leading Edge, **21**, No. 3, 280–285.

Grechka, V., Theophanis, S., and Tsvankin, I., 1999, Joint inversion of P- and PS- waves in orthorhombic media: Theory and a physical modeling study: Geophysics, **64**, No. 1, 146–161.

Grechka, V., and Tsvankin, I., 1998, 3-D description of normal moveout in anisotropic inhomogeneous media: Geophysics, **63**, No. 3, 1079–1092.

Haase, A. B., and Ursenbach, C. P., 2007, Spherical-wave computational AVO modeling in elastic and anelastic isotropic two-layer medias: EAGE Expanded Abstracts.

Helbig, K., 1983, Elliptical anisotropy-its significance and meaning: Geophysics, **48**, No. 7, 825–832.

Henley, D. C., 2003, Coherent noise attenuation in the radial trace domain: Geophysics, **68**, No. 4, 1408–1416.

Hsu, C., and Schoenberg, M., 1993, Elastic waves through a simulated fractured medium: Geophysics, **58**, No. 7, 964–977.

Hunt, L., Reynolds, S., Brown, T., Hadley, S., Downton, J., and Chopra, S., 2010, Quantitative estimate of fracture density variations in the Nordegg with azimuthal AVO and curvature: A case study: The Leading Edge, **29**, No. 9, 1122–1137.

Innanen, K. A., 2012, AVO theory for large contrast elastic and anelastic targets in pre-critical regimes: SEG Expanded Abstracts.

Jenner, E., 2002, Azimuthal AVO: methodology and data example: The Leading Edge, **21**, No. 8, 782–786.

Jin, S., Cambois, G., and Vuillermoz, C., 2000, Shear-wave velocity and density estimation from PS-wave AVO analysis: Application to an OBS dataset from the North Sea: Geophysics, **65**, 1446–1454.

Karayaka, M., and Kurath, P., 1994, Deformation and failure behavior of woven composite laminates: Journal of Engineering Materials and Technology, **116**, 222–232.

Kebaili, A., and Schmitt, D. R., 1997, Ultrasonic anisotropic phase velocity determination with radon transformation: Journal of the Acoustical Society of America, **101**, 3278–3286.

Kim, K. Y., Sribar, R., and Sachse, W., 1995, Analytical and optimization procedures for determination of all elastic constants of anisotropic solids from group velocity data measured in symmetry planes: Journal of Applied Physics, **77**, No. 11, 5589–5600.

Krautkrämer, J., and Krautkrämer, H., 1975, Werkstoffprüfung mit Ultrascall: Springer Verlag, Berlin.

Kundu, T., 2003, Ultrasonic Nondestructive evaluation: engineering and biological material characterization: CRC Press.

Lax, P. D., 1997, Linear algebra and its applications: Pure and Applied Mathematics: A Wiley interscience Series of Texts and Monographs and Tracts.

Lay, D. C., 1996, Linear algebra and its applications: Addison-Wesley.

Lortzer, G. J. M., and Berkhout, A. J., 1993, Linearized AVO inversion of multicomponent seismic data in Castagna, J.P., and Backus, M.M., Offset-dependent reflectivity theory and practice of AVO analysis: Society of Exploration Geophysicists, 303–313.

Luo, M., and Evan, B. J., 2004, An amplitude-based multiazimuth approch to mapping frcatures using P-wave seimsic data: Geophysics, **69**, No. 3, 690–698.

Lynn, H. B., 2004a, The winds of change: Anisotropic rocks—their preferred direction of fluid flow and their associated seismic signatures - Part 1: The Leading Edge, **23**, No. 7, 1156–1162.

Lynn, H. B., 2004b, The winds of change: Anisotropic rocks—their preferred direction of fluid flow and their associated seismic signatures - Part 2: The Leading Edge, **23**, No. 7, 1258–1268.

Mah, M., and Schmitt, D. R., 2001a, Experimental determination of the elastic coefficients of an orthorhombic material: Geophysics, **66**, No. 4, 1217–1225.

Mah, M., and Schmitt, D. R., 2001b, Near point-source longitudinal and transverse mode ultrasonic arrays for material characterization: IEEE transactions on ultrasonics, ferroelectrics, and frequency control, **48**, No. 3, 691–698.

Mahmoudian, F., 2006, Linear AVO inversion of multi-component surafce seismic and VSP data: University of Calgary, M.Sc. Thesis.

Margrave, G. F., 2000, Methods of seismic data processing: University of Calgary Course Notes.

Margrave, G. F., Stewart, R. R., and Larsen, J. A., 2001, Joint PP and PS seismic inversion: The Leading Edge, **20**, No. 9, 1048–1052.

McSkimin, H. J., 1967, Physical acoustic, vol. I, Part A: Academic NewYork.

Menke, W., 1985, Geophysical Data Analysis: Discrete Inversion Theory: Academic Press.

Musgrave, M. J. P., 1970, Crystal Acoustics: Holden-Day, San Francisco.

Nelson, R. A., 1985, Geologic analysis of naturally fractured reservoirs, Second edition: Golf Publishing Company, Book Division.

Newman, P., 1973, Divergence effects in a layered earth: Geophysics, **38**, No. 3, 481–488.

Nye, I. F., 1957, Physical properties of crystals: Oxford Press.

Okoye, P. N., Zhao, P., and Uren, N. F., 1996, Inversion technique for recovering the elastic constants of traversly isotropic materials: Geophysics, **61**, No. 4, 1247–1257.

Ortiz-Osornio, M., and Schmitt, D. R., 2010, Physical Modeling of the Reflectivity and Transmissivity Dependence on Tilt and Azimuth of a Material with Orthorhombic Symmetry: SEG Expanded Abstracts.

Parkes, G. E., Hatton, A., and Haugland, T., 1984, Marine source array directivity, a new wide airgun array system: First Break, **2**, No. 4, 4–15.

Parsons, R. W., 1996, Permeability of Idealized Fractured Rock: Society of Petroleum Engineers, 126–136.

Pšenčík, I., and Farra, V., 2005, First-order ray tracing for qp wave in inhomogeneous weakly anisotropic media: Geophysics, **70**, No. 6, D65–D75.

Resnik, J. R., 1993, Seismic data processing for AVO and AVA analysis: Investigation In Geophysics Series, , No. 8, 175–189.

Rudzki, M. P., 1911, Parametrische darstellungd er elastischen welle in anisotropen medien: Anzeiger der Akademie der Wissenachaften Krakau, 503–536.

Rüger, A., 1997, P-wave reflection coefficients for transversely isotropic models with vertical and horizontal axis of symmetry: Geophysics, **62**, No. 3, 713–722.

Rüger, A., 2001, Reflection coefficients and azimuthal AVO analysis in anisotropic media: Goephysical Monograph Series.

Sayers, C. M., and Ebrom, D., 1997, Seismic traveltime analysis for azimuthally anisotropic media: Theory and experiment: Geophysics, **62**, No. 5, 1570–1582.

Schijns, H., Schmitt, D. R., Heikkinen, P. J., and Kukkonen3, I. T., 2012, Seismic anisotropy in the crystalline upper crust: observations and modelling from the outokumpu scientific borehole, finland: Geophysical Journal International, **189**, 541553.

Schmerr, L. W., 1998, Fundamentals of nondeconstructve evaluation - A modeling approach: Plenum Press.

Schoenberg, M., and Helbig, K., 1997, Orthorhombic media: Modeling elastic wave behavior in a vertically fractured earth: Geophysics, **62**, No. 6.

Sheriff, R. E., 1991, Encyclopedia dictionary of applied geophysics: Society of Exploration Geophysicists.

Shuey, R. T., 1985, A simplification of the Zoeppritz equations: Geophysics, **50**, No. 4, 609–614.

Smith, G., and Gidlow, P., 1987, Weighted stacking for rock property estimation and detection of gas: Geophysical Prospecting, 993–1014.

Song, L. P., and Every, A. G., 2000, Approximate formulae for acoustic wave group slownesses in weakly orthorhombic media: Journal of Physics D: Applied Physics, **33**, L81–L85.

Spratt, R. S., Goins, N. R., and Fitch, T. J., 1993, Pseudo-Shear - The Analysis of AVO: Investigation In Geophysics Series, **8**, 37–56.

Stearns, D. W., 1994, Fractured reservoirs school notes.

Tadepalli, S. V., 1995, 3-d avo analysis: Physical modeling study: University of Houston, PhD. Thesis.

Theophanis, S., and Zhu, X., 2003, Ultrasonic Numerical Modeling of Reflections from Simulated Fractured Reservoirs.

Thomsen, L., 1986, Weak elastic anisotropy: Geophysics, **51**, No. 10, 1954–1966.

Thomson, L., 1988, Reflection seismology over azimuthally anisotropic media: Geophysics, **53**, No. 5, 304–313.

Tsvankin, I., 1997, Anisotropic parameters and P-wave velocity for orthorhombic media: Geophysics, **62**, No. 4, 1292–1309.

Tsvankin, I., 2001, Seismic signatures and analysis of reflection coefficients in anisotropic media: Elsevier, Amsterdam.

Uren, N. F., Gardner, G. H. F., and McDonald, J. A., 1990, The migrator's equation for anisotropic media: Geophysics, **55**, No. 11, 1429–1434.

Ursenbach, C. P., Hass, A. B., and Downton, J. E., 2006, Improved modeling of spherical-wave AVO: CREWES Research Reports.

Ursin, B., 1990, Offset-dependent geometrical spreading in a layered medium: Geophysics, **55**, No. 4, 492–496.

Vavryčuk, V., and Pšenčik, I., 1998, P-wave reflection coefficients in weekly anisotropic elastic media: Geophysics, **63**, No. 6, 2129–2141.

Červený, V., and Ravindra, R., 1971, Theory of seismic head waves: University of Toronto Press, Toronto.

Vestrum, R. W., 1994, Group- and phase-velocity inversions for the general anisotropic stiffness tensor: University of Calgary, M.Sc. Thesis.

Vestrum, R. W., Lawton, D. C., and Schmitt, R., 1999, Imaging structures below dipping TI media: Geophysics, **64**, No. 4, 1239–1246.

Wang, S., and Li, X., 2003, Fracture detection using 3D seismic data: A physical modeling study: SEG Expanded Abstracts.

Wang, S., Li, X., Qian, Z., Di, B., and Wei, J., 2007, Physical modeling studies of 3D P-wave seismic for frcature detection: Geophysical Jounnal International, **168**, 745–756.

Winterstein, D. F., and Hanten, J. B., 1985, Suppercritical reflections observed in P- and S-wave data: Geophysics, **50**, No. 2, 185–195.

Wong, J., Hall, K. W., Gallant, E. V., Maier, R., Bertram, M., and Lawton, D. C., 2009, Seismic physical modeling at University of Calgary: Canadian Society of Exploration Geophysicists Recorder.

Zheng, Y., 2006, Seismic Azimuthal Anisotropy and Fracture Analysis from PP Reflection Data: University of Calgary, PhD. Thesis.

Zheng, Y., and Wang, S., 2005, Fracture analysis on prestack migrated gathers: A physical modeling study: CSEG Expanded Abstracts.